PERFORMANCE EVALUATION AND DYNAMICS OF ROVERS FOR PLANETARY EXPLORATION

Bahareh Ghotbi

Department of Mechanical Engineering McGill University, Montréal

December 2015

A Thesis submitted to the Faculty of Graduate Studies and Research in partial fulfilment of the requirements for the degree of Doctor of Philosophy

© Bahareh Ghotbi, 2015

Abstract

Planetary exploration and off-road applications require rovers to operate in unstructured environments, involving interaction with soft soil, non-homogeneous terrain and sloped and rocky surfaces. In this context, simulation and analysis tools can be very helpful to characterize the mobility of rovers under various terrain conditions.

Modelling of rovers with the objective of predicting their behaviour requires adequate knowledge of the parameters of the system and its environment. Due to the existence of uncertainties in estimation of terrain properties, accurate prediction of wheel-soil interaction poses the main challenge in the simulation of rover manoeuvres. However, accurate prediction of a rover behaviour may not be necessary for evaluation and improvement of its design and operational strategies. To this end, an alternative approach is introduced which relies on what is termed *observative* models, as opposed to the predictive ones. The objective of using observative models is to develop an understanding of the way the system performance would be affected by the change of its design and operation parameters. Observative models of rovers are able to capture the trends that are generally observed and it is shown that variations in terrain parameters do not affect the validity of the results obtained with these models.

A detailed study of the wheel-soil interaction phenomena is carried out which shows that the ability of rovers in developing drawbar pull is greatly influenced by the distribution of the normal load among their wheels. The *normal force dispersion* is

ABSTRACT

used as a performance indicator to compare the mobility of different rover configurations. Based on the type of soil and other factors such as the multipass effect, a series of design and operation guidelines are proposed in order to improve the ability of rovers to generate higher drawbar pull and climb steeper slopes and larger obstacles. These guidelines include the modification of the chassis internal force distribution via redundant actuation. The effectiveness of the proposed approaches is investigated via simulation studies and extensive sets of experiments with two rovers, the Juno and the Rover Chassis Prototype (RCP). Redundant actuation is realized by introducing some design modifications to the RCP which enables online modification of normal force dispersion.

The simulation studies are carried out using a generic multibody dynamics library which is developed as a part of this research. This library can serve as a generic and rover-specific analysis tool and addresses some of the shortcomings in the available simulation packages.

Résumé

Les missions d'exploration planétaire comme les applications tout-terrain imposent aux véhicules d'évoluer dans des environnements nonstructurés, dans lesquels ils sont confrontés à des sols meubles, hétérogènes, irreguliers, voire rocheux. Dans un tel contexte, les simulations et les outils d'analyse se révèlent d'une aide précieuse pour caractériser la mobilité de ces véhicules sur différents types de terrains.

La modélisation des robots mobiles en vue de prédire leur comportement nécessite une bonne connaissance des paramètres du système et de son environnement. Du fait des incertitudes dans l'estimation des propriétés du terrain, la restitution fidèle des interactions roues-sol constitue le défi principal de la simulation des véhicules tout-terrain. Cependant, une prédiction précise du comportement du robot n'est pas toujours nécessaire à l'évaluation et à l'amélioration de sa conception et de ses stratégies d'évolution. Aussi, une approche alternative est proposée ici, en s'appuyant sur les modèles dits observatif, par opposition aux modèles prédictifs. L'utilisation desdits modéles doit permettre de comprendre la manière dont la conception et les paramètres de fonctionnement influent sur les performances du système. Les observatif sont capables de saisir les tendances que pren globalement le robot et il a été montré que la modification des paramètres du terrain n'affectent pas la validité des résultats obtenus par de tels modèles.

RÉSUMÉ

Une étude détaillée des phénomènes d'interaction roue-sol est réalisée. Celle-ci montre que la traction développable par un véhicule est hautement influencée par la distribution des réactions normales sur les roues. La dispersion de ces derniéres est donc utilisée comme indicateur de performance pour comparer la mobilité de différentes configurations de robots. À partir du type de sol et d'autres facteurs comme le roulement dans les traces des roues frontales, un ensemble de directrices pour la conception et le déploiement est proposé afin de donner aux robots mobiles à roues la capacité de générer davantage de traction, gravir des pentes plus prononcée et franchir des obstacles plus importants. Ces directrices incluent la modification de la distribution des forces internes au moyen d'un actionnement redondant. L'efficacité des approches proposées est testée à l'aide de simulations et d'une gamme étendue d'essais basé sur deux exemples de robots roulants, le Juno et le Rover Chassis Prototype (RCP). La redondance d'actionnement est élaborée en introduisant quelques changements dans la conception du RCP afin de permettre la modification en ligne de la dispersion des forces normales.

Les études en simulation sont réalisées en utilisant une bibliothèques dynamique générique développée dans le cadre de cette recherche. Cette bibliothèques fournit une série d'outils d'analyse aussi bien génériques que spécifiques aux systèmes roulant et permet de pallier les lacunes des logiciels de simulation existants.

Claims of originality

- (i) The concept of observative models is presented with the objective of predicting the way in which changes in the design, actuation, or configuration of the rover will affect its ability to operate. The mobility of a four-wheeled rover is analyzed using observative models which allows for developing performance indicators as functions of rover parameters and state. This modelling approach provides guidelines for the design and operation of complex systems without resorting to detailed modelling and requiring precise values of the system and environment parameters.
- (ii) A methodology to improve the mobility of mobile robots on soft terrain is proposed which relies on maintaining the optimum normal force distribution throughout the rover operation. The set of system and terrain properties that accentuate the effect of normal force distribution on the rover mobility is identified. An extensive set of experiments is carried out with a six-wheeled rover which confirms the effectiveness of this method and validates the simulation results.

CLAIMS OF ORIGINALITY

- (iii) Redundant actuation is used for online modification of the internal force distribution in order to achieve the desired normal force distribution during the rover operation. This method is shown effective in improving the rover mobility on soft terrain and its obstacle-climbing performance.
- (iv) Terramechanics relations are implemented for spatial simulation of rovers in the generic multibody dynamics library. This implementation includes proper transformation of the generalized coordinates and velocities of the wheel to its plane of motion to compute slip and sinkage. Additionally, the built-in functions of the library represent the output of the terramechanics model, which is the set of terrain reaction forces, in the array of generalized forces of the system model. This process requires information about the generalized velocities of the wheels.

Acknowledgements

I would like to express the deepest appreciation to my supervisors Professor József Kövecses and Professor Jorge Angeles. Without their guidance and persistent help this thesis would not have been possible.

This project owes its inception and progression to the strong collaboration between McGill University and industry. The financial and technical support by MacDonald, Dettwiler and Associates is gratefully acknowledged.

I have been very fortunate to work with Dr. Francisco Gónzalez over the last few years. He is the co-author of the generic multibody dynamics library which is described in this thesis. Our numerous technical and non-technical discussions has made my Ph.D. journey a memorable experience.

I am grateful to Dr. Ali Azimi for sharing with me his knowledge on terramechanics. My colleagues Sadhbh MacMahon and Qingfeng Lou have been a constant source of encouragement and support especially during our experimental tests.

Finally, I would like to use this opportunity to express my sincere gratitude to my family, especially my parents for working their best to give me the education, the opportunities, and the courage to pursue my dreams.

| Abstrac | et |
|---------|---|
| Résumé | ś ii |
| Claims | of originality |
| Acknow | vledgements |
| LIST C | OF FIGURES xii |
| LIST C | OF TABLES |
| CHAP | ΓER 1. Introduction |
| 1.1. | Motivation |
| 1.2. | Scope and objectives of the thesis |
| 1.3. | Organization of the thesis |
| CHAPT | ΓER 2. Literature Review |
| 2.1. | Multibody dynamics simulation tools |
| 2.2. | Wheel-ground interaction in rover dynamics simulators |
| 2.3. | Wheel-soil interaction models |
| 2.4. | Performance analysis of mobile robots |
| 2.5. | Effect of load distribution on rover mobility |
| | |

| 2.6. Us | e of redundant actuation for mobility and stability improvement | 19 |
|-----------------|---|--------------|
| СНАРТЕР | R 3. Concept of Observative Models | 21 |
| 3.1. Int | croduction | 21 |
| 3.2. Dy | vnamics modelling | 25 |
| 3.2.1. | General formulation | 25 |
| 3.2.2. | Operation on hard terrain | 27 |
| 3.2.3. | Operation on soft terrain | 28 |
| 3.3. Ob | oservative models for analysis | 32 |
| 3.4. Illu | ustration with simulation | 37 |
| 3.4.1. | Predictive model | 38 |
| 3.4.2. | Observative model | 38 |
| 3.4.3. | Simulation results | 43 |
| 3.5. Ex | eperimental results | 48 |
| СНАРТЕР | R 4. Effect of Normal Force Distribution on Rover Performance | 53 |
| | croduction | 53 |
| | nalysis of a single wheel moving on soft soil | 55 |
| | plementation of terramechanics relations in dynamic simulation | 56 |
| 4.3.1. | · | 59 |
| | ormal force dispersion as mobility indicator | 61 |
| | oplication of the concept | 64 |
| | Effect of normal force distribution on wheel slip | 69 |
| 4.5.2. | Effect of normal force distribution on drawbar pull | |
| | escription of the experiments | 70 70 |
| | | 70 |
| 4.6.1. | Slip ratio measurement | 72 |
| 4.6.2. 4.6.3 | Modification of load distribution of the chassis | 74 76 |
| 403 | MODIFICATION OF IOAG CHSETDHLION OF THE CHASSIS | - <i>i</i> r |

| 4.6.4. Considerations for redundant actuation |
|--|
| 4.6.5. Selection and placement of pneumatic actuators 8 |
| 4.7. Modification of the normal force distribution |
| 4.8. Experimental results |
| 4.8.1. Effect of reconfiguration on normal forces |
| 4.8.2. Effect of reconfiguration on drawbar pull 9 |
| 4.9. Comparison of experimental and simulation results |
| 4.10. Effect of soil parameters on F_D -vsNFD relation 10 |
| 4.10.1. Effect of the pressure - sinkage parameter k_{ϕ} 10 |
| 4.10.2. Effect of larger normal loads |
| 4.11. Obstacle climbing |
| 4.12. Multipass effect |
| 4.12.1. Theory |
| 4.12.2. Effect of normal force distribution considering the multiple passages 12 |
| CHAPTER 5. Closing Remarks |
| 5.1. Conclusions |
| 5.2. Recommendations for future work |
| 5.2. Recommendations for future work |
| BIBLIOGRAPHY |
| APPENDIX A. Soil parameter estimation for the RCP experiments 14 |
| APPENDIX B. The Generic Multibody Dynamics Library |
| B.1. Introduction |
| B.2. Structure and organization of the library |
| B.3. General dynamic equations |
| B.3.1. Parametrization of the motion of a single body 15 |
| B.3.2. Dynamic equations of a single body |
| |

| B.3. | 3. | Dynamic equations of a set of unconstrained bodies | 58 |
|-------|------------------------------|--|------------|
| B.3. | 4. | Dynamic equations of a system of bodies constrained to each other 16 | 30 |
| B.4. | Libi | rary implementation | 31 |
| B.4. | 1. | Data structures: BODIES, CONSTS, FORCES 16 | 32 |
| B.4. | 2. | Predefined constraints | 3 4 |
| B.4. | 3. | Definition of forces | 35 |
| B.5. | For | mulation and algorithm options | 39 |
| B.6. | $\operatorname{Int}\epsilon$ | grator options | 75 |
| B.7. | Nur | nerical integration | 76 |
| B.8. | Pos | t processing | 7 9 |
| B.9. | Disj | play | 30 |
| B.10. | Ar | nalysis capabilities of the library | 30 |
| B.10 |).1. | Position, velocity, and acceleration problems | 31 |
| B.10 |).2. | Force and motion specification | 34 |
| B.10 |).3. | Velocity transformation | 35 |

xiii

| 3.1 | Free-body diagram of a rigid wheel in contact with soft soil, with driving torque t_a and normal load $w 	cdots 	cdots$ | 29 |
|-----|--|----|
| 3.2 | A five degree-of-freedom, 2-D model of a planetary rover on uneven terrain | 37 |
| 3.3 | Effect of the variation of the torque distribution parameter α on (a) the net tangential force obtained with the observative (dashed lines) and predictive models (solid lines) and (b) the slip at the wheel-terrain contact point obtained with the predictive model | 45 |
| 3.4 | Effect of the variation of the torque distribution parameter α on the net tangential force obtained with the predictive model for different soil parameters (solid lines) and the observative model (dashed lines) | 46 |
| 3.5 | Effect of the variation of wheel radius on the net tangential force obtained with the predictive model for different soil parameters (solid lines) and the observative model (dashed lines), for $\alpha=1,\ldots,$ | 47 |
| 3.6 | Juno Rover with additional mass elements in configurations A (left) and B (right) | 48 |

| 3.7 | Effect of the CoM position of the Juno rover on (a) the normal | |
|------|--|----|
| | force and (b) the net tangential force at the wheel-soil interface, as | |
| | predicted by simulation with Azimi et al. model [1] | 49 |
| 3.8 | Time history of the loads applied to the rover in experiments with | |
| | configurations A and B . The average values of the loads during the | |
| | representative period of the motion are superimposed on the figure | |
| | as straight lines | 51 |
| 4.1 | Input and output variables to terramechanics model | 57 |
| 4.2 | Transformation of coordinates and velocities from the global refer- | |
| | ence frame to the wheel local frame and transformation of the terrain | |
| | reactions from the wheel local frame to the global reference frame | 58 |
| 4.3 | F_D -vs F_n relation for a single wheel with different slip ratios on soil | |
| | "B" | 60 |
| 4.4 | F_D -vs F_n relation for a single wheel with different slip ratios on soil | |
| | "A" | 61 |
| 4.5 | Effect of non-uniform normal force distribution on the total available | |
| | drawbar pull | 62 |
| 4.6 | The RCP rover | 64 |
| 4.7 | The chassis elements and the wheel of the RCP | 65 |
| 4.8 | CAD model of the RCP was used to extract parts dimensions and | |
| | joints positions to build the multibody model of the rover | 66 |
| 4.9 | The RCP operation modes (courtesy of MDA) | 67 |
| 4.10 | Illustration of the multibody model of the RCP | 68 |
| 4.11 | Values of the slip-vsNFD index developed by the RCP while climb- | |
| | ing a 10° slope, with a 22.5 kg payload | 69 |

| 4.12 | Correlation between the maximum slope angle that the RCP can | |
|------|---|----|
| | climb (with a 90% slip) and the NFD | 71 |
| 4.13 | Drawbar pull test with the RCP | 72 |
| 4.14 | A winch was used to control the translational velocity of the rover . | 73 |
| 4.15 | Drawbar pull tests were carried out using a winch to obtain a more | |
| | uniform rover motion compared to the setting illustrated in Fig. 4.13 | 73 |
| 4.16 | On-board force sensor readings in the normal direction at the front, | |
| | middle, and rear starboard wheels | 75 |
| 4.17 | Snapshot of the recording of the GoPro camera which shows the | |
| | screen of the force scale | 75 |
| 4.18 | Force applied to the rover by the human operator | 76 |
| 4.19 | Force applied to the rover by the winch | 77 |
| 4.20 | Effect of CoM repositioning and redundant actuation on normal | |
| | force distribution | 78 |
| 4.21 | Design modification of the RCP to add redundant actuation option . | 84 |
| 4.22 | Kinematic simulation of the actuator and bogie sub-mechanism to | |
| | study mechanism singularity | 86 |
| 4.23 | Snapshots from the simulation of the climbing manoeuver of the | |
| | RCP on a 0.3-m-high step in the presence of the actuators | 87 |
| 4.24 | Length of the actuator during climbing a 0.3-m-high step | 88 |
| 4.25 | Switch Ready Aluminum Air Cylinder selected from McMaster-CARR | |
| | catalogue | 89 |
| 4.26 | Time history of the torque applied by the pneumatic actuators on | |
| | the bogies during the climbing manoeuvre of 0.3-m-high step. The | |
| | actuator force was kept constant at 400 N | 90 |

| 4.27 | The RCP while climbing large obstacles with the aid of the actuators | 91 |
|------|--|-----|
| 4.28 | The NFD of the RCP during climbing of terrain 2 in Table 4.4. The | |
| | internal actuation torque T was increased in two successive steps, | |
| | from 0 Nm to 20 Nm and then to 50 Nm | 92 |
| 4.29 | Slip of the front, middle and rear wheels of the RCP during climbing | |
| | the terrain of case 2 in Table 4.4, for the manoeuvre in Fig. 4.28 $$ | 92 |
| 4.30 | Experimental results: Normal force on the starboard wheels of the | |
| | RCP with $\eta = 139$ N and $\eta = 113$ N | 95 |
| 4.31 | Experimental results: Normal force on the starboard wheels of the | |
| | RCP with $\eta = 97$ N and $\eta = 69$ N | 96 |
| 4.32 | Effect of redundant actuation on the NFD | 98 |
| 4.33 | Drawbar pull during experiments with 60% slip and several NFD | |
| | values | 99 |
| 4.34 | Experimental (a) and simulation (b) results from the drawbar pull | |
| | experiments | 102 |
| 4.35 | Slip-vsNFD plots for different slopes described in Table 4.8, with | |
| | a 22.5 kg payload on the RCP | 104 |
| 4.36 | Slip-vsNFD plots for different payloads for the RCP climbing a 7.5° | |
| | slope on soil "B" from Table 4.1 | 105 |
| 4.37 | Multibody model of the RCP climbing a step obstacle of height | |
| | h = 0.1 m with no actuators | 105 |
| 4.38 | Multibody model of the RCP climbing a step obstacle of height | |
| | h = 0.3 m with actuators | 106 |
| 4.39 | Modelling the no-slip revolution of the wheel about the corner of the | |
| | step obstacle by placing a virtual pin joint at the contact point | 107 |

| 4.40 | Torque applied to the front wheels of the RCP during the climbing | |
|------|--|-----|
| | a 0.1-m-high step for different values of the redundant actuation | |
| | torque (T_g) | 108 |
| 4.41 | Torque applied to the middle wheels of the RCP during the climbing | |
| | a 0.1-m-high step for different values of the redundant actuation | |
| | torque (T_g) | 109 |
| 4.42 | Torque applied to the front wheels of the RCP during the climbing | |
| | a 0.3-m-high step for different values of the redundant actuation | |
| | torque (T_g) | 110 |
| 4.43 | Torque applied to the front wheels of the RCP during the climbing | |
| | a 0.3-m-high step for different values of the redundant actuation | |
| | torque (T_g) | 110 |
| 4.44 | Schematic of repetitive loading characteristics of soil, obtained from | |
| | reported bevameter tests $[2]$ | 112 |
| 4.45 | Relationship between the soil stiffness and initial unloading sinkage . | 113 |
| 4.46 | Schematic of wheel passage on a compacted soil and wheel's local | |
| | and absolute sinkage measurements | 114 |
| 4.47 | Multipass effect predicted by [3] and with the generic multibody | |
| | dynamics library | 118 |
| 4.48 | F_D -vs F_n relation for different number of wheel passages with 50% | |
| | slip on soil "B" | 121 |
| 4.49 | Drawbar pull variation for a range of NFD values considering mul- | |
| | tipass effect | 126 |
| A.1 | The drawbar pull-slip curve obtained from experiments and simula- | |
| | tions with soil parameters listed in Table A.1 | 149 |
| | | |

| B.1 | Examples of multibody systems modelled in the library: (a) double | |
|-----|---|-----|
| | pendulum, (b) Bricard mechanism, (c) the Rover Chassis Prototype | |
| | (RCP), (d) Juno rover, (e) MER, (f) ExoMars | 166 |
| B.2 | Flowchart of the algorithm with the trapezoidal rule and the aug- | |
| | mented Lagrangian formulation with projections | 177 |
| B.3 | Calculating the constraint forces associated with constraint of index | |
| | idxCt on the body of index idxB1 | 180 |

LIST OF TABLES

| 3.1 | Soil parameters used for the predictive model | 3 |
|------|--|---|
| 4.1 | Set of soil parameters used for study of F_D -vs F_n curves 60 | 0 |
| 4.2 | Placement parameters of the pneumatic linear actuators on the chassis 83 | |
| 4.3 | Specifications of the selected actuator from McMaster Carr catalogue 88 | 3 |
| 4.4 | Properties of different slopes used in the simulations | 1 |
| 4.5 | Effect of internal actuation on the slope climbing ability of the RCP | |
| | for the cases described in Table 4.4 | 3 |
| 4.6 | Experimental results of drawbar pull for different values of the NFD | |
| | (averaged for each test) | O |
| 4.7 | Operation conditions of the tests | 1 |
| 4.8 | Slope characteristics for the simulation of the climbing manoeuvre | |
| | of the RCP | 3 |
| 4.9 | Parameters defined in [3] for the multipass model | 7 |
| 4.10 | Parameters introduced in [3] for terramechanics model 11 | 7 |
| 4.11 | Soil parameters used for terramechanics and multipass models in the | |
| | RCP simulation | 9 |

LIST OF TABLES

| 4.12 | Solution of the maximization problem for the RCP operation on soil |
|------|--|
| | "B" with 50% slip |
| 4.13 | Solution of the maximization problem for the RCP operation on soil |
| | "A" with 60% slip |
| A.1 | Set of soil parameters estimated via experimental results of the RCP |
| | operation in Mars Dome |

CHAPTER 1

Introduction

1.1 Motivation

Mobile robots are among the best candidates for planetary surface exploration due to their good performance in unstructured environments. Increasing mobility is generally a primary objective for the design and operation of wheeled robots. Reduced mobility can limit the ability of the robot to achieve the mission goals and can even render it immobile in extreme cases. This goal becomes especially challenging when these vehicles operate on soft terrain and in unstructured environments. In this case, the analysis, design, and operation planning of such robots are often based on predictive dynamic simulations, where the multibody model of the vehicle is combined with terramechanics relations for the representation of the wheel-ground interaction. However, the analysis of the complex wheel-ground interaction phenomenon poses serious difficulties and the terramechanics models are only helpful in capturing the behaviour of the vehicle under some restrictive assumptions. An alternative approach, which can be beneficial for design and operation decision making, is defining relevant performance indicators. For many analysis purposes, estimating the overall impact of system parameters variations on a performance indicator is the

primary objective; the precise value of the performance indicator being secondary. On the other hand, detailed analysis of the system dynamics and its interaction with the environment can assist in providing useful design and operation planning guidelines. These guidelines would be even more useful if they remain valid in presence of uncertainties of the system and environment parameters.

1.2 Scope and objectives of the thesis

The objective of this thesis is to develop analysis tools and algorithms to assist the design and operation of mobile robots. Planetary exploration rovers operating on unstructured environments are the main focus of the work. Common dynamics simulation packages generally perform only the forward-dynamics simulation. Furthermore, they do not necessarily make the models explicitly available to the user which makes it difficult to gain in-depth insight into the effect of design and operation parameters on the performance of the system. To overcome these limitations, a generic multibody dynamics library is developed as part of this research which is capable of simulating mechanical systems via motion or force specification. This means that it is possible to specify forces acting on, or the motion of systems, or a combination of both as input to the simulation. Several models to represent the wheel-soil interaction have been included in this implementation. The library is open-architecture which allows users to access the time history of all the variables and dynamics terms in the model of the system. Open architecture is especially advantageous in the analysis of complex systems, where access to the dynamics terms and evaluation of user-defined indicators enhance the understanding of the system behaviour and performance.

Given the complexity of the wheel-soil interaction phenomenon and lack of knowledge of the terrain properties, especially in planetary applications, the available models can fail to provide a high fidelity estimation of the forces involved in the interaction. An alternative approach, which we refer to as observative models, is introduced in the thesis. This approach can allow for the definition of performance indicators to characterize the behaviour of the system without resorting to the complex and computationally expensive wheel-terrain interaction models. Observative models may capture certain aspects of the behaviour of the physical system; the aspects that are important for performance evaluation of the system and can provide useful information for design, control, and decision making. They can be used to predict the way in which system parameters of rovers will affect their operation.

The definition of relevant performance indicators and identification of influential parameters on the system performance generally require in-depth knowledge of the nature of the system. A detailed study of the wheel-soil interaction and dynamics of the robot has led to the definition of a performance indicator which can be used for rover design and reconfiguration planning. In this work, the effect of internal force distribution of the rover chassis on its mobility is analyzed. The validity of this index is assessed using both simulation and experimental results obtained for a six-wheeled rover prototype. Modifying the system configuration and employing active suspension to alter the chassis internal force distribution are studied for their effect on the available traction force at the wheel-terrain interfaces, and consequently, the rover mobility.

1.3 Organization of the thesis

This thesis includes five chapters and two appendices:

- Chapter 1 briefly introduces the research topic and highlights the motivation, objective, and the organization of the thesis.
- Chapter 2 provides an overview on the rover simulation packages, wheelsoil interaction models, and available rover analysis tools and performance indicators in the literature.

CHAPTER 1. INTRODUCTION

- Chapter 3 introduces the concept of observative models and their role in evaluation and comparison of performance of rovers. The validity of the results achieved from observative models is assessed by those obtained from terramechanics relations as well as experimental tests.
- Chapter 4 discusses the effect of load distribution on the mobility of wheeled robots and provides guidelines to improve the rover performance in slope and step climbing manoeuvres. Redundant actuation of the chassis is recommended in order to gain control on the internal force distribution of the chassis. An extensive set of experiments which supports the simulation results are described in this chapter.
- Chapter 5 summarizes the material presented in this thesis, and highlights the contributions and the areas for future research work.
- Appendix A includes a description on the procedure for estimating the parameters of the terrain used in the experiments with the RCP rover.
- Appendix B describes the structure of the generic multibody dynamics library and series of tools which can be used for analysis of mechanical systems.

CHAPTER 2

Literature Review

The successful mission of the US rover Sojourner on Mars in 1997 [4] motivated the use of wheeled mobile robots for planetary exploration applications in the next missions. The twin rovers Spirit and Opportunity landed on Mars in 2003 and managed to send back valuable information during their operation which lasted much longer than initially planned [5, 6]. Since then, much research work has been invested in analyzing the past and planning the future missions on Mars [7, 8] and the Moon [9]. The latest successful landing on Mars took place in 2012 by Curiosity [10]. The future planned missions include the ExoMars rover under development by the European Space Agency in collaboration with the Russian Federal Space Agency [11] and the Mars 2020 rover mission under planning by NASA [12]. The common challenge in all these missions is related to the operation condition of the rovers which requires them to navigate through unstructured and soft terrain with little known properties. Reproducing such environments under the earth conditions is not simple and can be impossible in some cases. Therefore, modelling and simulation tools can play an important role during design and operation planning of rovers.

2.1 Multibody dynamics simulation tools

Rovers are a class of mobile robots which are mainly designed to operate in unstructured environments. From the mechanics point of view, they consist of a main body, a set of wheels and a mechanism connecting the body to the wheels. Rigid or flexible multibody models can be used to represent rovers in dynamics simulations. These models can be in a symbolic or a general numerical form. The former is useful in parametric studies of a system while the generation of the latter can be automated by computer programs which is useful for large multibody systems. MapleSoft MapleSim [13] is a commercial product that provides the capability of symbolic modelling. Is some cases, in order to obtain the symbolic form of a system model certain simplifications are required. Examples of such simplifications are reduction of the model to two dimension or modelling the ground reaction forces by a simple spring and damper system. The Performance Optimization Tool (POT) presented in [14] is a two-dimensional simulator which is developed to evaluate and compare different rover chassis designs. POT performs quasi-static analysis on rover models to find the input actuation which can optimize the rovers locomotion performance metrics such as friction coefficient.

However, most commercial software tools such as SIMPACK [15], SAMCEF Mecano [16], RecurDyn [17], and MSC ADAMS [18] generate numerical models of mechanical systems. The computational cost of simulation of a system depends on the level of detail involved in the model which can vary based on the application type. For example, in software packages which provide real-time simulation there is a trade-off between computational cost and accuracy of the results. In this regard, CM Labs Vortex [19], which is a simulation tool developed for training purposes, has been very successful in finding a right balance. However, the level of accuracy provided by Vortex may not be sufficient for performance analyses intended for design or

operation improvements. In addition to commercial software tools, several simulation tools have been developed by research groups around the world, such as Gazebo [20] and MBDyn [21]. MBDyn is an open-source software developed at Dipartimento di Scienze e Tecnologie Aerospaziali of the Polytechnic Institute of Milan, Italy. According to the website of this software, it has been used in the aerospace, wind energy, automotive, and mechatronic fields such as robotics applications. The special feature of the MBDyn is its ability to couple with external solvers which enables co-simulation of multiphysics systems. For example, in order to simulate aircraft MBDyn couples with Computational Fluid Dynamics (CFD) tools to capture the behaviour of the system.

Due to the increasing demand on understanding the dynamics of mechanical systems in various applications, multibody dynamics simulation capability has been added to existing packages which did not initially include this feature. As an example, the SimMechanics library of MATLAB [22] provides a 3D multibody simulation environment as an extension to the MATLAB Simulink software. One advantage of this tool is the ease of modelling. Also, it is possible to integrate mechanical systems to the existing Simulink blocks which include control algorithms and models of electrical and pneumatic subsystems. However, features such as collision detection are not included in the library and thus, have to be programmed by the user. Another example is SolidWorks, which is produced by Dassault Systems. SolidWorks has been used primarily as a CAD and CAE tool. The motion analysis feature [23] was later added to predict the physical movements of an assembly under defined loads using the dynamics of the system. The collision detection among the bodies is realized with the aid of the CAD models and the relative motion of the bodies is derived from the assembly mates.

In the past few decades, several simulation tools have been developed to particularly serve mobile robotics applications such as planetary explorations. The Jet Propulsion Laboratory (JPL) has developed Dynamics Algorithms for Real-Time Simulation (DARTS) [24] which is a flexible multibody dynamics simulator for designing and testing spacecraft. The Rover Analysis, Modelling, and Simulation toolbox (ROAMS) [25, 26] was then developed as an extension to DARTS as a real-time simulator supporting planetary rover exploration missions. ROAMS includes a library of kinematics and dynamics models of mobile robots and manipulator arms. Model of onboard sensors and batteries as well as navigation and locomotion modules are also available which can be used to define custom simulation scenarios. Another example is Gazebo which is a simulator for robotics systems initially developed at University of Southern California. Gazebo operates based on a physics engine for modelling of various types of robots in interaction with outdoor and indoor environments. This open-source package provides both programming and visual interfaces as well as high-quality graphics.

For the purpose of the research which was carried out in this thesis a multibody simulation tool was necessary. One part of the requirements for this simulator was modelling and analysis of rover manoeuvres using various parameterizations of the multibody model of the rover and different relations to represent its interaction with the environment. Furthermore, having full access to all the dynamic terms and variables during the simulation was necessary to gain a deep understanding on the behaviour of the system. These motivated the development of a generic multibody dynamic library as part of this research which is described in Appendix B.

2.2 Wheel-ground interaction in rover dynamics simulators

Modelling of the wheel-terrain interaction has received special attention in rover simulators due to their considerable role in the behaviour of the system. Simulations use various methods to represent the wheel-ground interaction phenomena. These methods include: classical terramechanics models, general contact models, and simple spring-damper models. The fidelity of simple models in calculating the terrain reaction forces may not be high enough.

The Adams-based Rover Terramechanics and Mobility Interaction Simulator (ARTEMIS) [27] includes a tire module and contact force models to predict the terrain reaction forces. These modules were added to Adams which as mentioned earlier is one of the commonly used multibody packages. ARTEMIS consists of a library of terramechanics models and high-resolution height maps of the Mars surface which can be helpful in providing accurate prediction of rover mobility in exploration missions. As an example, it was used by Lindemann et al. [28] to assist in the design of the Mars Exploration Rovers (MER), Spirit and Opportunity.

Lamon and Siegwart [29] simulated a six-wheeled rover with passive suspension mechanism in Open Dynamics Engine (ODE) using Coulomb friction model as the wheel-ground contact model. The Open Dynamics Engine (ODE) is an open-source library for simulating dynamics of rigid body systems in three dimensional space. A traction control strategy was proposed which finds the optimal wheel torque to minimize the slip.

The ROAMS system uses SimScape environment [30, 31] which is a general-purpose terrain modelling toolkit to simulate key applications such as planetary landing and surface operations. SimScape features include multiple representations of the terrain geometry, transformation between different terrain model representations, import and export of terrain data from and to various forms of terrain databases, and combining models responsible for various properties of the terrain such as composition, texture, and reflectivity.

Another example of terrain libraries is a commercially available software package called AESCO Soft Soil Tire Model (AS²TM) [32]. This library is available as a Simulink S-Function and is mainly developed based on the research results from the

former Institute for Automotive Engineering (IKK) at the University of the Federal Armed Forces Hamburg [33]. The library includes models for rigid wheel and elastic tire and can evaluate the terrain reaction forces such as tractive and lateral forces and rolling resistance. It can capture the slip-sinkage effect, influence of tire tread, and multipass effect.

In [34], Bauer et al. presented a Rover Chassis, Analysis, and Simulation Tool (RCAST) which couples the rigid multibody dynamics engine of SimMechanics toolbox with AS²TM. The objective of development of RCAST was to evaluate the locomotion performance of rovers to support the European Space Agency (ESA) ExoMars mission.

Classical terramechanics models which are mainly based on the work by Bekker [35] and Wong [36] are widely used in simulation environments to evaluate rover design and performance. Parallel to the development of RCAST, a set of tools called RCET was developed by ESA which also aimed at supporting the design and performance optimization of the ExoMars rover [37]. The tractive prediction module (TPM) available in RCET uses classical terramechanics models.

Apostolopoulos [38] studied the effect of configuration parameters on rover performance using a computational framework named Locomotion Synthesis (LocSyn). The classical terramechanics relations were used in LocSyn to model the wheel-ground interaction. The optimal configuration parameters were obtained based on the three performance indicators which were defined to quantify rover mobility: trafficability, manoeuvrability and terrainability.

Another example of the software which uses classical terramechanics models is the Rover Performance Evaluation Tool (RPET) developed by the Surrey Space Centre and German Aerospace Centre (DLR) [39]. RPET can be used as a rover chassis evaluation tool. It consists of two main modules: Rover Mobility Performance Evaluation Tool (RMPET) and Mobility Synthesis (MobSyn). RMPET determines the mobility performance based on indicators such as drawbar pull, slippage, and sinkage for different types of mobility systems. The performance of wheeled, tracked, and legged mobility systems can be evaluated on a wide range of terrain types such as Martian, Lunar, and other user defined models. MobSyn, on the other hand, is similar to LocSyn in the way that it also outputs the optimum configuration parameters for the given desired performance on a specific type of terrain.

2.3 Wheel-soil interaction models

A summary of available modelling techniques to address the complex phenomena of wheel-soil interaction is presented here. Study of soil behaviour using models based on continuum mechanics has received increasing attention in the past few decades [40, 41]. With the recent advancements in the development of faster computers this approach shows higher potential to be used in different applications. The particular benefit of this approach is its ability to capture complex scenarios such as interaction with a terrain consisting of different materials as well as complex geometric surfaces. The work by Perumpral et al. [42] is one of the earliest examples of such modelling method to simulate the wheel-terrain interaction. The stress distribution and terrain deformation was captured by Finite Element Modelling (FEM). One clear advantage of this method is that the deformation of both the wheel and the terrain are the result of interaction forces and no assumption on the shape of the contact contour is required. This feature was successfully captured in [43, 44] where the tire and soil were separately modelled and interacted during the simulation.

Liu and Wong [45] studied the deformation patterns and stress distributions in the soil using FEM and compared the result with the available experimental data. In order to improve the accuracy of the numerical analysis Shikanai et al. [46] carried out a set of experiments on a single wheel testbed to measure soil particle movement and the developed drawbar pull (DBP). However, FEM is not suitable for situations where large terrain deformation or high slippage is expected beneath the wheel. In these situations Discrete Element Modelling (DEM) is preferred.

The results from several papers [47–49] show the applicability of DEM in predicting the interaction forces but they also indicate that for more accurate results the number of particles must be expanded which comes at the price of increase in the computational cost. Although these methods can provide higher accuracy in the prediction of terrain reaction forces the number of terrain parameters that should be provided based on the terrain characteristics is higher compared to terramechanics models. This makes the terrain parameter identification process even more complicated.

Azimi et al. [50] proposed a novel approach for calculating the stress and strain fields in the vicinity of the wheel-soil contact area based on elasto-plasticity theory. In this approach, some assumptions on the velocity field of the soil particles is made. With those assumption, in order to find the terrain reactions finite element analysis is not required.

Semi-empirical methods are widely used to develop wheel-terrain interaction models based on experimental observations and theoretical studies. This branch of models is originated from the work of Bekker [35, 51, 52] who significantly contributed to the development of classical terramechanics relations. These models are developed with the objective of calculating the vehicle drawbar pull as a function of its slip ratio. The drawbar pull is obtained by summation of the net tangential force, the tractive minus the resistive forces, of all the wheels of the vehicle. The resistive and tractive forces acting on each wheel depend on the normal and shear stresses at the wheel-terrain contact.

Bekker [35] assumed that the normal stress at a point on the contact area between the wheel and soil can be obtained from the average pressure under a flat plate at the same sinkage. The *bevameter* test, which involves a plate pushed into the soil, is a well-known technique for obtaining the pressure-sinkage parameters of the soil [35]. The compression resistance of the soil is measured by monitoring the load applied to plates of different sizes and their sinkage value. Additionally, the shear strength of the soil can be measured by pressing and turning a circular plate with radial grousers [36]. The relationship between the shear stress and shear displacement is obtained by measuring the torque applied on the plate as a function of angular displacement of the plate and its normal load. The determination of the shear strength of the soil is necessary in order to predict the behaviour of powered wheels. The terrain reaction forces are evaluated by integrating the normal and shear stresses at the points along the wheel-terrain contact area. This model and the modifications introduced by Wong and Reece [53], which are referred to as classical terramechanics relations, are commonly used in many simulators to evaluate the terrain reaction forces. Several research centres around the world have developed terrestrial test facilities to study the soil behaviour under the wheel, mainly constructing single wheel or full rover testbeds [38, 54–59].

The classical terramechanics relations are primarily developed to capture the palanar steady-state motion of a wheel on soft soil. However, during the past few decades some modifications to the original terramechanics relations have been introduces to expand their range of application.

Simulation of a wheel-soil interaction using the original form of the classical terramechanics relations results in an artificial oscillatory response in the vertical direction during transient motion of the wheel. The reason is that based on these relations the normal reaction force from the terrain does not depend on the sinkage rate of the wheel in the soil. Azimi et al. [1] added a nonlinear damping term in the vertical direction to obtain realistic response with zero or negligible oscillation in multibody dynamics simulation environments.

CHAPTER 2. LITERATURE REVIEW

Ishigami et al. [60] extended the terramechanics relations to include the lateral forces which are generated during steering manoeuvres. The flat-terrain assumption was adopted in the multibody simulation of a four-wheeled rover on soft soil. This study was later extended to uneven surfaces by Ding et al. [61] and the terramechanics relations were simplified to increase the simulation speed. In addition to driven wheel, Wong and Reece [62] also studied the governing terramechanics relations for towed wheel. The behaviour of towed and free-rolling wheels were also addressed by Gee-Clough [63]. Shmulevich et al. studied the effect of velocity on wheel performance and presented a modified normal stress model [64]. This model included velocity dependent terms to explain the effect of wheel velocity on the stress distribution under the wheel. The wheel sinkage and wheel performance indicators such as maximum net tractive force ratio and maximum tractive efficiency were shown to increase at higher wheel speed.

The presence of wheel grousers can have significant effect on the terrain reaction forces. A simple technique to include the effect of grousers in the model is to add the height of the grousers to the radius of the wheel and use the original terramechanics relations to obtain the reaction forces with these larger effective diameters [65]. Trease et al. modelled the effect of individual wheel grouser on developing traction and provided estimation of the resultant resisting torque due to the additional traction force [27]. Chan and Sandu developed a 3D quasi-static tire model for dynamics simulation of on-road and off-road vehicles [66, 67].

Due to the sensitivity of the terramechanics model parameters to soil conditions [68] the issue of online identification of soil parameters has been the subject of research. The online soil parameter estimation using rover sub-systems was addressed in several studies. Moore et al. estimated some characteristics of different types of terrains by an instrumented arm of the Viking Lander [69]. The sampler arm was used to scrap the soil crust and dig trenches. The shape and size of the trenches as

well as the force required to create them were combined to estimate certain properties of the terrain. The driving torque of the wheels has been used as an indicator of the terrain strength and deformation in the missions of the Mars Pathfinder Sojourner micro rover [70, 71] and the twin rovers, Spirit and Opportunity [72]. Along the same lines, the soil identification for tracked vehicles was addressed by Seneviratne et al. [73] and for small mobile robots by Ojeda et al. [74].

In the process of soil parameter identification the forces and moments acting on a wheel are used to estimate the following parameters: the cohesion and internal friction angle of the soil, the cohesive sinkage modulus, frictional sinkage modulus, and sinkage exponent. However, due to the complex form of terramechanics relations the online parameter identification algorithms can only work on a simplified form of these relations. Iagnemma et al. [75] have proposed an algorithm to estimate the soil parameters using on-board sensors. In order to use a linear-least squares method to estimate terrain parameters based on the sensor readings, the classical terramechanics equations were simplified. In a similar work by Ding et al. [76] the normal and shear stresses were linearized to obtain a set of symbolic expressions which were then used to identify the planetary soil parameters.

2.4 Performance analysis of mobile robots

Autonomous operations of planetary exploration rovers require an advanced level of decision making ability based on the input data from the environment. Therefore, analysis tools can be very helpful in providing useful information for decision making processes. These tools must consider the physics of the system and its interaction with the environment in order to identify the best ways to improve the performance of the robot throughout the operation.

Lamon et al. [77] proposed an analysis approach based on the rover quasi-static model. This method can find the optimum torque of the wheels to limit the slip

CHAPTER 2. LITERATURE REVIEW

and increase the drawbar pull. Performance evaluation of mobile robots for rough terrain applications was investigated by Thueer et al. [78] via introducing a selection of metrics. These metrics target different aspects of mobility improvement such as increasing the traction development, reduction in torque requirement for motors of the wheels, and decreasing the accumulated slip over the course of the manoeuvre. Also, a new metric called velocity constraint violation (VCV) was defined to quantify the deviation of each wheel velocity from the ideal velocity achieved under the rolling condition.

Zhang et al. [79] used the classical terramechanics models to study the effect of configuration parameters of the rover on its mobility. The mobility of two lunar locomotion systems LER-1 and ALR were compared via certain mobility indicators. Examples of the indicators used in that study are free drawbar pull coefficient, defined as the ratio of wheel drawbar pull to its load, and motion resistance coefficient, which is the ratio the resistance force to the normal load on the wheel.

Iagnemma and Dubowsky [80] presented a rough-terrain control (RTC) methodology and defined their optimization criteria as maximum ground traction and minimum power consumption by the motors. These two performance indicators together with the quasi-static force balance equations and the physical constraints of the system formed an optimization problem. The priority of each performance index during the operation was prescribed by a weighting factor. The selected physical constraints of the system were: the saturation limit of the actuators, non-zero wheel-ground normal reaction force for all the wheels, and maximum available ground tractive force for a given normal load. In order to solve the above optimization problem on uneven terrain the wheel-ground contact angles had to be known. A technique based on kinematic relations of the rover, introduced by the same authors [81], was adopted to estimate the contact angle for each wheel.

Yoshida et al. [82] analyzed the behaviour of a planetary rover with the aid of dynamic simulation of the rover and terramechanics relations to model the wheel-terrain interaction. Specifically for applications on rough terrain, this study led to development of an effective control law which was shown to improve traversability while limiting the slip ratio [83].

Ishigami et al. [84] studied the performance of a planetary exploration rover prototype in slope climbing and traversing using terramechanics relations. Slope traversability was evaluated using two new-defined criteria: mobility limit and trafficability limit. The study helped determining the appropriate motors for slope negotiation and improving the control algorithm.

A methodology based on virtual friction angle is used by several authors [77, 78, 80, 85] to improve mobility, especially for applications on rigid ground. The objective of this methodology is to reduce the likelihood of developing wheel slip via minimization of the virtual friction coefficient $\mu^* = F_T/F_N$, where F_T is the traction and F_N the normal force at each contact point. Along the same lines, the concepts of traction margin and slip margin were defined by Thueer and Siegwart [78] and used in traction control of several rover concepts.

Many researchers have addressed the issue of rover stability and have proposed control algorithms which consider both stability and mobility to improve the rover performance. Papadopoulos defined a stability metric based on stability angles [86]. A stability angle is measured as the angle between the vertical line and a line which passes through the rover CoM and is normal to one of its tip-over axes. Zero stability angle indicates marginal stability. In several other papers, the same concept has been the basis of stability comparison among different rover configurations [87–89]. In another work presented by Schenker et al. [90] the minimum friction coefficient and stability angles were used to define the cost function for configuration optimization of rovers. The analysis was carried out in two stages: First, at the predictive

reconfiguration stage, the configuration of the chassis based on the surface shape of the terrain ahead was computed. Based on the computed joint angles and wheelterrain contact angles the minimum friction coefficient that satisfied the static force balance of the system was calculated. In the second stage, the reactive reconfiguration stage, a stability angles were used to find the closest stable configuration to the rover nominal configuration to maximize the ground clearance.

2.5 Effect of load distribution on rover mobility

The effect of the internal force distribution of the chassis and the resultant load distribution among the wheels has not been rigorously addressed in the literature. Based on results obtained from experiments with a four-wheeled rover, Ishigami stated that a variation in the normal force distribution does not change the drawbar pull developed by the vehicle [91]. However, it is acknowledged in the same work that a balanced load distribution helps reducing the resistant torque on some wheels and consequently improving the rover mobility. On the other hand, some researchers mention a uniform distribution of normal forces among the factors that enhance mobility. Grand et al. state that balancing the normal loads helps the vehicle to develop higher drawbar pull [92]. Along the same lines, Freitas et al. suggested that uniformly distributing the weight of the rover among the wheels is a valid strategy to achieve better mobility, when adequate information about contact forces is not available [93]. A similar conclusion was reported by Michaud et al. [37]: the load distribution among the wheels has to be even on flat ground to achieve the best performance. The positive effect of uniform load distribution on the improvement of climbing ability is also mentioned in [94]. As a consequence, special attention must be paid to good adaptation to the terrain and the position of the centre of mass when deciding on the structure of the rover as well as during its operation on uneven surfaces.

2.6 Use of redundant actuation for mobility and stability improvement

Several studies have addressed the underactuated nature of rover chassis to introduce modification to the chassis internal force distribution in favor of certain optimization criteria. Waldron and Abdallah [95] state that vehicles with active suspension can have enhanced performance in all terrain conditions with the aid of their active degrees of freedom. Vehicles with four or more wheels are kinematically redundant when placed on the ground. Therefore, while satisfying the force equilibrium, the distribution of normal load among the wheels can vary in order to improve mobility and performance of the system. In the same work several performance indicators were considered and some algorithms were described by the same authors for solving the force-equilibrium equations. In one of the proposed algorithms, minimizing the Euclidean norm of the contact forces was used to impose zero interaction force condition by which the ground contact forces did not work against each other. Another algorithm, called the optimal friction angle algorithm, allocated the contact forces in a way that the maximum friction angle among all the wheels is minimized [95]. The study was carried out assuming rigid wheel-ground contact and negligible dynamics effects.

In another work presented by Kuroda et al. [96] two rover designs were compared in terms of their mobility in step and slope climbing manoeuvres: (a) a conventional four-wheeled drive system and (b) a rover with a new chassis design which consisted of a conventional four-wheeled drive system and an extra wheel attached to the chassis via an active joint. The latter was designed with the objective of distributing the vertical load equally among all the wheels during step climbing. It was shown that the new design outperformed the conventional four-wheeled drive rover in both slope and step climbing.

CHAPTER 2. LITERATURE REVIEW

Kubota et al. [97] described a test scenario in which the traversability of a six-wheeled robot in two states of active and passive suspension were compared. In the rover design considered in their work, the active suspension was able to control the pitch and roll angles of the rover. Traversability was defined based on several factors: stability, obstacle climbing, ability to escape from an immobilized state, motor torque requirement for the wheels, and energy consumption. A new indicator named adhesive coefficient was also defined which quantified the deviation from even weight distribution among the rover wheels. This indicator is equivalent to what is introduced in this thesis as normal force dispersion. However, the conditions under which the study in [97] is carried out are very restrictive compared to the assumptions in this thesis. The most restrictive assumptions in [97] are no-rolling and no-slipping conditions, static model, and flat surface. Also, the method was not validated experimentally.

Finally, Sreenivasan and Wilcox [85] have also addressed the use of active suspension to influence the contact forces at the vehicle terrain contact points. The active suspension was presented as a means to achieve the set of contact forces which minimizes the maximum of friction angle among the wheels and keeps the rover stable. The proposed control strategy of the chassis was developed for a particular four-wheeled robot in the planar motion.

It must be noted that in all the above studies the effect of normal force distribution was studied under the assumption of rigid wheel-ground contact. In some papers [80, 93], it was shown experimentally that the results obtained under the assumption of rigid wheel-ground contact are also valid for operation of rovers on soft terrain. However, even in those cases no in-depth study of the relationship between the normal force on the wheel and the traction force it can develop on soft soil was carried out.

CHAPTER 3

Concept of Observative Models

3.1 Introduction

Predictive dynamic simulation of mobile robots aims to anticipate the time response of the system under internal and external forces as close to the real-life response and excitation as possible. Simulation includes the solution of an initial value problem of the governing dynamic equations. The mathematical models that form the basis of such simulation studies have to represent the system elements as realistically as possible. This is an extremely challenging task. In our context the most problematic element is usually the wheel-soil interaction. The detailed study of terramechanics plays a key role in the design, analysis, and simulation of wheeled mobile robots. Nonetheless, there are many open issues that can be mentioned. For example, robots are required to be robust to environmental effects when it comes to semi-autonomous missions. However, terramechanics models can be very sensitive to the inaccuracies in the soil parameters [68]; the identification of these parameters is a major challenge [75, 76, 98], as described in detail in Chapter 2. Also, the fidelity of the terramechanics models can be questioned. The detailed modelling of the vehicle-terrain interaction may not be able to provide high-fidelity estimation

of the forces involved in the interaction. The models are even less accurate when exact information on terrain properties is not available, which is particularly the case for planetary-exploration rovers. Conventional terramechanics models, e.g., those of Bekker and Wong [35, 36], have not really been developed for application in dynamic analysis and simulation. Furthermore, these models do not provide full insight on how the variations of the system parameters can influence the reaction forces and performance. This is the motivation for proposing a new concept to capture the representative aspects of the behaviour of the physical system, those that are important for performance evaluation and can result in parametric models for design analysis.

The experience of recent planetary exploration missions has brought to the limelight many challenges that must be faced in the autonomous operation of mobile robots in unstructured environments; these involve interaction with soft terrain and sloped and rocky surfaces. This brings the need for simulation and analysis tools that should provide a way of characterizing the mobility of the system under various terrain conditions. Recent efforts in this area have led to the development of several simulation toolboxes that include multibody dynamics models of mobile robots and wheel-soil interaction models [25, 27, 34, 37, 99]. The analysis results provided by these simulation toolboxes can be useful in evaluating different design ideas and control strategies [14, 77, 80, 85, 90, 95–97, 100, 101]. A review of these simulation packages and their analysis tools is available is Chapter 2.

Rover performance can be analyzed considering different aspects. One of them is mobility, which is specially important in applications on unknown and soft terrain. Due to the autonomous nature of planetary applications, it is critical to identify possible strategies to enhance the mobility of the rover and the modes of failure. Mobility is not rigorously defined in the literature for wheeled vehicles operating on soft soil. The concept is clearly defined for mechanism models where the connections between the links are given with holonomic or nonholonomic kinematic constraints, e.g., for

linkages or wheeled robots operating on hard surfaces [102]. However, for rovers operating on soft terrain, generally such kinematic constraints cannot be given a priori for the modelling of wheel-ground interaction. Also, for wheeled rovers mobility is often meant in a different sense: the ability to move from a certain configuration or to move with maximum speed. Apostolopoulos [38] categorized the mobility performance of wheeled robots under three terms: manoeuvrability, terrainability, and trafficability. Manoeuvrability refers to the steering capabilities of the robot and its ability to navigate through obstacles in cluttered environments. Based on this definition, locomotion parameters such as the robot length-to-width ratio can then be calculated as functions of traction forces and total motion resistance developed at the wheel-terrain contact. Terrainability is the ability to negotiate uneven terrain without losing stability, while providing enough traction for forward motion. A parametric relation between the maximum slope the robot can climb and stability requirements, traction-force limits, and power limitations of the robot is obtained. Trafficability is defined as the ability of the robot to generate traction and overcome resistance, which is the primary focus in the context of robot mobility. In [38], the dependency of sinkage, soil traction, and motion resistance forces on wheel parameters, diameter, and width, are represented by parametric expressions. All of the above expressions are obtained based on assumptions such as uniform normal stress distribution, which greatly simplifies the terramechanics relations. Some of the existing mobility indicators were studied along with novel concepts to quantify mobility, as proposed and applied to exploration rovers on hard ground [14, 27, 33, 77, 80, 97]. These indices include minimum friction requirement at wheel-ground contact for forward motion, maximum actuation torque requirement, total slip distance over the course of a run, and average violation of pure rolling constraint among all wheels of the vehicle. In fact, slip plays a key role in the determination of the mobility of a wheeled rover on soft soil, as pure rolling cannot always be guaranteed during

motion. Moreover, Iagnemma et al. [103] showed using simulation results that, due to the slip-sinkage effect, increased slippage causes additional sinkage of the wheel, which will result in increased motion resistance. The concept of maximum mobility for wheeled robots on soft soil is thus related to minimizing the slip of the wheels.

In order to improve the behaviour of a rover it is necessary to identify the influential parameters at the design and operation levels. In different designs of planetary rovers the parameters that can be tuned during the operation vary. In some designs it is possible to control the distribution of input power among the wheels. In several studies [77, 85, 89, 104] improvement of the wheel traction through proper selection of input torques to the wheels is discussed. Lamon et al. [77] considered quasi-static modelling, as the dynamic effects are assumed to be negligible within the range of robot speed, while the calculation of the friction requirement was based on the Coulomb friction model. However, in practice, the value of the friction coefficient is not known. According to the foregoing approach it is first assumed that the wheel does not slip and the ratio of traction to normal force falls below the actual friction coefficient. With this assumption it is possible to calculate normal and traction forces as functions of torque applied to the wheel. Next, in an optimization process an input torque that minimizes the ratio of traction to normal force is calculated. By doing this, the chance that this ratio can be smaller than the friction coefficient increases.

The concept of observative models was introduced by Ghotbi et al. in [105] and is described in this chapter. Such models are not intended to replace their terramechanics counterparts. However, they can provide information about the way in which a change in the design, actuation, or configuration of the rover can affect its ability to operate. At the design and control stages it is very important to foresee all the challenging situations in which the rover would face mobility problems, to provide tools and algorithms to avoid those situations or to overcome them. In

reconfigurable robots it is possible, for instance, to change the position of the centre of mass (CoM) and other effective inertial properties, which can provide an important means to improve the mobility of the system and its stability [106]. The effect of changes in other parameters such as distribution of input torque and wheel radius is also discussed in this chapter.

3.2 Dynamics modelling

3.2.1 General formulation. A key element in wheeled mobile robots is the characterization of their interaction with the ground via the wheels. The wheel-ground contact usually involves a complex geometry and a finite contact area. However, the forces and moments exchanged between the wheel and the ground can generally be represented with a resultant force and a resultant moment about a reference point on the perimeter of the wheel. Based on this we will assume that the contact forces and moments will be represented this way with a reference contact point.

If the rover is freed from the contact with the ground, then its configuration can be represented with a minimum set of n generalized coordinates arrayed in vector \mathbf{q} . Using this set of coordinates for the parametrization of the dynamics, the model of the rover can be expressed as

$$\mathbf{M\ddot{q}} + \mathbf{c} = \mathbf{f} \tag{3.1}$$

where **M** is the $n \times n$ mass matrix of the system, **c** the n-dimensional array of Coriolis and centrifugal terms, and **f** the n-dimensional array of generalized forces. The generalized forces include three main parts: $\mathbf{f} = \mathbf{f}_w + \mathbf{f}_d + \mathbf{f}_o$, where \mathbf{f}_w represents

¹We note that the selection of this set of coordinates is not unique; the choice of coordinates depends on the analyst, the system, and the need at hand.

CHAPTER 3. CONCEPT OF OBSERVATIVE MODELS

the wheel-ground interactions, \mathbf{f}_d is the driving force, and \mathbf{f}_o represents the other loads acting on the system, e.g., gravity.

In the ideal case, the kinematic relations that describe the motion of the wheels in contact with the ground are non-holonomic. These are written, at the velocity level,

$$A\dot{q} - s = 0 \tag{3.2}$$

where **A** is the $s \times n$ matrix mapping the pertinent generalized velocities into the velocities of the wheel-contact points and frames, and **s** the s-dimensional array of the velocities of the wheel contact points and frames; this term includes, for example, wheel slip and also the possible motion of the wheel in a direction normal to the ground. This velocity-level relationship are expressed at the acceleration level as

$$A\ddot{\mathbf{q}} + \dot{\mathbf{A}}\dot{\mathbf{q}} - \dot{\mathbf{s}} = \mathbf{0} \tag{3.3}$$

The required motion of the rover can be represented by a set of b kinematic relations. For instance, it is possible to specify the desired forward acceleration or velocity of the rover for a given manoeuvre. If these relations are holonomic, they can be expressed at the configuration level as $\Phi_d(\mathbf{q},t) = \mathbf{0}$. Their corresponding velocity-level expression is in the form

$$B\dot{\mathbf{q}} - \mathbf{b} = \mathbf{0} \tag{3.4}$$

where **B** is the $b \times n$ matrix that represents the required rover motion in terms of the generalized velocities, and $\mathbf{b} = \mathbf{b}(t)$ is the b-dimensional array of required rover velocities. At the acceleration level these relations are written as

$$\mathbf{B}\ddot{\mathbf{q}} + \dot{\mathbf{B}}\dot{\mathbf{q}} - \dot{\mathbf{b}} = \mathbf{0} \tag{3.5}$$

It must be noted that despite Eq. (3.4), the kinematic relations shown in Eq. (3.2) are not constraint equations in their general form. This will be discussed in Section 3.2.2.

Based on the kinematic relations given by Eqs. (3.2) and (3.4) the decomposition of the generalized forces in Eq. (3.1) can be represented in more detail as

$$\mathbf{f} = \underbrace{\mathbf{A}^{\mathrm{T}} \boldsymbol{\lambda}_{w}}_{\mathbf{f}_{w}} + \underbrace{\mathbf{B}^{\mathrm{T}} \boldsymbol{\lambda}_{d}}_{\mathbf{f}_{d}} + \mathbf{f}_{o}$$
(3.6)

where λ_w is the s-dimensional array of ground reactions transmitted to the wheels from the ground, and λ_d is the b-dimensional array that represents the generalized forces associated with the b required rover motion specifications. Henceforth, we will assume that either the required rover motion is specified via **b** and Eqs. (3.4) and (3.5), or the forces and moments λ_d associated with desired motion are given directly.

In the case of rovers operating on unstructured terrain, the nature of the wheel-ground interaction presents a significant, additional difficulty. The task of the analyst is to choose the most suitable interaction model to describe the phenomenon under modelling. This can generally be done in two different ways, either by specifying the forces and moments λ_w developed at the wheel-ground contacts via constitutive relations, or by imposing representative kinematic specifications on the wheel-ground interface motions denoted by \mathbf{s} in the model above. We will consider two representative cases here.

3.2.2 Operation on hard terrain. This is the most commonly considered case for wheeled robots in the literature. For these operations it can generally be a reasonable approach to assuming that the wheel-ground interaction can be well-represented by *kinematic specifications*, namely, the conditions of no slip and no penetration. In the formulation presented above this is represented by imposing

the kinematic constraints $\mathbf{s} = \mathbf{0}$. With this the ground reactions λ_w will become generalized constraint forces, i.e. part of the variables that are determined by the system dynamics.

For this situation the kinematic specifi-3.2.3 Operation on soft terrain. cations of no slip and no penetration are generally not applicable; a better characterization of the wheel-ground interaction can be achieved by means of constitutive relations. These can be based on the terramechanics relations proposed by Bekker [35], later modified by Wong and Reece [36], which are the most widely used relations for wheel-terrain interaction on soft soil. Terramechanics relations are a type of constitutive relations based on semi-empirical models of wheel and soil interaction. They offer a relatively good approximation for the case of steady-state motion. However, there can be many problems with the application of these formulas, particularly due to the highly uncertain parameters that need to be identified with extensive experimental work; furthermore, the results of the identification task can be highly sensitive to changes of soil or environmental conditions. Also, these formulas may fail to provide proper representations for dynamic operating conditions. Several new terramechanics models have also been developed based on the concepts put forth by Bekker [35] and Wong [36]. These also suffer from several of the above-mentioned shortcomings, yet this classical terramechanics approach still provides the simplest state-of-the-art representation to develop constitutive relations of the wheel-ground interaction on soft soil.

In the Bekker and Wong models [35, 36] the terrain reaction forces are obtained by integrating the normal stress σ and the shear stress τ over the wheel contact area. This gives the elements of λ_w for each individual wheel. Figure 3.1 shows the interpretation of these force and moment components as well as the representative wheel parameters and variables. According to this figure, in the x-direction, parallel

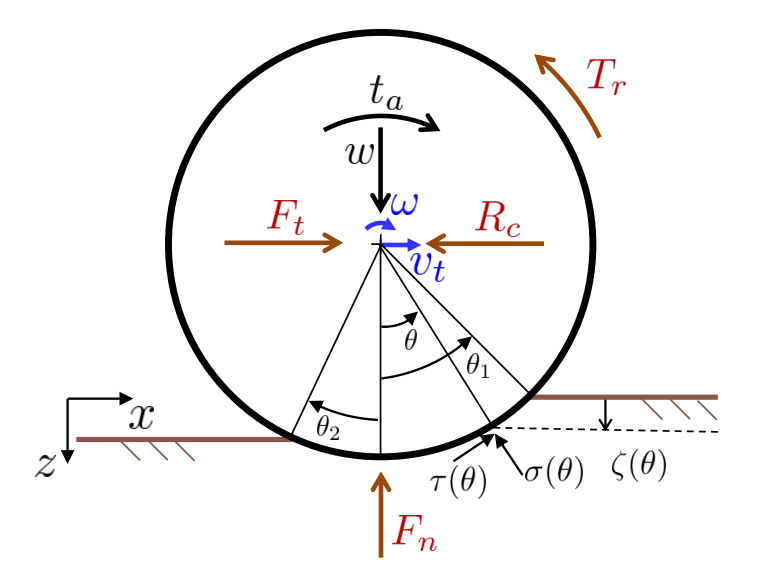


FIGURE 3.1. Free-body diagram of a rigid wheel in contact with soft soil, with driving torque t_a and normal load w

to the soil surface, rolling resistance R_c opposes the motion, while F_t is the tangential, traction force component. For the normal direction, F_n represents the normal reaction and T_r the resisting torque about the axis of the wheel. Based on Bekker's and Wong's work, [35] and [36], and also considering the modifications proposed by Azimi et al. [1] the expressions for these components can be derived as

$$R_c = rb \int_{\theta_2}^{\theta_1} \sigma(\theta) \sin \theta d\theta, \tag{3.7}$$

$$F_t = rb \int_{\theta_2}^{\theta_1} \tau(\theta) \cos \theta d\theta, \tag{3.8}$$

$$F_n = rb \int_{\theta_2}^{\theta_1} [\tau(\theta)\sin\theta + \sigma(\theta)\cos\theta] d\theta - c_z \dot{z}, \qquad (3.9)$$

$$T_r = r^2 b \int_{\theta_2}^{\theta_1} \tau(\theta) d\theta \tag{3.10}$$

In the above relations, r and b are the wheel radius and width, respectively, and θ_1 and θ_2 indicate the angles associated with the beginning and end points of contact

CHAPTER 3. CONCEPT OF OBSERVATIVE MODELS

on the wheel perimeter. In the Bekker model, θ_2 is zero. The term $c_z\dot{z}$ in Eq. (3.9) introduces a velocity-dependent damping [1], with \dot{z} denoting the velocity of the wheel centre in the normal direction.

In Eqs. (3.7) - (3.10), the normal stress at the wheel-terrain interface is given by:

$$\sigma(\theta) = \left(\frac{k_c}{b} + k_\phi\right) \zeta(\theta)^n \tag{3.11}$$

where n is the sinkage exponent, ζ is the vertical sinkage at any point on the contact surface, and k_c and k_{ϕ} denote the pressure-sinkage moduli associated with the soil cohesive and frictional components, respectively. The wheel slip is calculated as a function of the horizontal component of the velocity of the wheel centre v_t and its angular velocity ω in planar motion:

$$i_s = (r\omega - v_t)/r\omega \tag{3.12}$$

The shear stress can be determined as

$$\tau(\theta) = \left[c + \sigma(\theta)\tan\phi\right] \left[1 - e^{\frac{-r}{K}}[\theta_1 - \theta - (1 - i_s)(\sin\theta_1 - \sin\theta)]\right]$$
(3.13)

where c is the terrain cohesion, ϕ is the internal friction angle, and K is the shear deformation modulus [36]. In Eqs. (3.11) and (3.13), n, k_c , k_{ϕ} , c, ϕ , and K are terrain parameters that need to be determined experimentally.

The forces and moments in Eqs. (3.7)–(3.10) represent the soil reactions developed in the plane defined by the wheel and resolved about the wheel centre point. This is the form typically used in terramechanics. To obtain the resultant components that form the elements of λ_w this system of forces needs to be interpreted in terms of the representative contact point of the wheel. At the contact point, the net tangential force is $F_t - R_c$, the net normal force is F_n , and the net torque about the axis of the wheel is $T_r - r(F_t - R_c)$. Additionally, soil reactions perpendicular to the

plane of the wheel, such as lateral bulldozing forces [60], can also contribute to the elements of λ_w .

The modifications introduced by Azimi et al. [1] were particularly concerned with the motion in the normal direction. The use of the original terramechanics formulas for dynamic operating conditions would result in unrealistic, undamped oscillations in the normal direction. The reason is that the normal pressure-vs.-sinkage curve determined via the bevameter tests [35, 36] may be seen as the constitutive relation of a nonlinear spring, which would certainly not be representative of dynamic wheel-ground interactions when the soil behaves as an elasto-plastic medium. Azimi et al's modification involves a dissipative term for motion in the normal direction to better reflect what can be observed in reality. This term has no effect under steady-state conditions, which imply zero rate of sinkage, for which the classical terramechanics formulas provide reasonable representations. However, this additional term extends the usability and applicability of the formulas for dynamic operating conditions. These have been illustrated with simulation and experiments [107]. Alternative wheel-terrain interaction models have been recently introduced in the literature, e.g., [50], which intend to provide a more accurate representation of the phenomenon at the contact interface. These include damping in a more natural way, in the constitutive model of the wheel-soil interaction.

As mentioned above, the terramechanics representations are highly sensitive to the soil parameters. The sensitivity of the dynamic response of a single wheel to small changes in some soil parameters, such as the friction angle and the apparent cohesion coefficient was studied in [68]. It was shown that the dynamic response is usually extremely sensitive to even small changes in soil parameters, as completely different results can be obtained with small perturbations in the parameters. This also points to the need of exploring alternative possibilities for the analysis of rovers operating on soft soil.

3.3 Observative models for analysis

In the two cases discussed above, the intention generally is to approximate the key phenomena of wheel-ground interaction as closely as possible with the selection of the appropriate model and point of view. For hard terrain this can be achieved by representing the interaction using kinematic specifications in the first place; for soft terrain, the representation of the interaction forces via constitutive relations usually seems the appropriate choice. However, the development of the appropriate constitutive relations for the wheel-soil interaction is an extremely challenging task; no model is available currently that would be able to address a broad range of operating conditions with high-enough fidelity.

On the other hand, the dynamics formulation described in Section 3.2.1 allows for the development of an alternative point of view in the analysis of rovers on soft soil. This relates to the definition of conditions that can contribute to the increase in rover mobility; the reformulation of the dynamics model with the appropriate selection of base variables reflects how parametric changes in the system affect the desired optimum conditions. We term such models observative, as the general intention and point of view are different compared to the traditional developments of predictive simulation where high fidelity soil modelling is an essential aspect. In the observative point of view we rather try to eliminate the detailed constitutive modelling of the soil via a formulation of the appropriate conditions for mobility improvement and performance indicators based on those. Predictive simulation may also be used to study the effect of system parameters on its performance. However, available constitutive models are very sensitive to soil parameters [68]. Therefore, the fact that analysis results using observative models are more general and are not affected by the selection of the soil parameters is an advantage of these models.

We conjecture that maximum mobility for a rover moving straight is achieved when the wheel slip is zero.² We define a zero wheel-slip when the instant centre of velocity of the wheel relative to the inertial ground passes through the contact point, defined earlier, that is, on the characteristic perimeter of the wheel.³ In such a case the velocity of the centre of the wheel and its angular velocity are connected via velocity-level kinematic relation, which are the same type as the ones appearing for hard terrain contact representation. Some elements of the s and s arrays in Eqs. (3.2) and (3.3) are specified as zero. This concept can be generalized for slip values different from zero also. In the case of zero slip the main body of the rover can achieve maximum speed. The question is how this maximum mobility can be accomplished, and how the system parameters affect that.

Most investigations based on dynamic simulation focus on what is known as the drawbar pull as a measure to characterize system mobility. The drawbar pull is related to the traction forces developed by the wheels and the ability of the rover to pull a load. The maximum drawbar pull is observed at nonzero slip ratios, depending on the soil and wheel properties [36].

However, it is noteworthy that the drawbar pull alone cannot fully characterize the mobility of the system. For example, a wheel with a slip ratio of close to one may develop higher drawbar pull compared to a non-slipping wheel [36], but the former cannot be considered to have better mobility. We also conjecture that the motion with maximum mobility is a natural motion of the system, i.e. it moves as such unless the conditions and connections to its environment cannot make that possible. When the rover is moving, actuation is applied on certain wheels, and the contact

²If a rover is turning, then mobility also depends on the type of steering concept used.

³At every instant the wheel geometry naturally defines a plane, normal to the wheel axis; the wheel motion can be decomposed into motion parallel to this plane and motion perpendicular to that. The general definition of the instant centre relates to the part of the wheel motion that is parallel to the reference plane.

between the wheel and the ground is necessary to propel the vehicle. On the other hand, this contact is passive and the reaction force between the wheel and the ground is developed, not applied, which is a very important point. Only as much reaction force is developed as needed to achieve the maximum mobility. In other words, the wheels only slip if the required traction forces cannot be achieved without slipping. For example, it can be observed with off-road vehicles and rovers that considerable slip is not necessarily developed when the terrain is able to provide enough traction. In this case, the vehicle achieves maximum mobility. The level of reaction force needed to maintain the maximum mobility condition depends on the rover design and loading. The transition from maximum mobility to lower mobility occurs when the wheel-ground interface cannot develop the necessary reaction force anymore. In such a case the wheel starts to slip in order to accommodate the increased load, which decreases mobility, i.e. the instant centre of velocity of the wheel with respect to the unperturbed, fixed ground tends to move closer to the wheel centre. As explained earlier, the instant centre of velocity is defined for the wheel motion in the plane normal to its axis. The same reasoning can apply to wheel motions normal to the ground: the wheel sinks until the terrain develops the necessary reaction forces.

From the point of view of energy considerations, the desired situation, in which wheel slip and sinkage are zero, is also the most efficient mode of operation. In that case, all the power applied to the wheel is spent on accelerating the system, i.e., in increasing its kinetic energy. If slip and sinkage are present, a fraction of the input power is lost by dissipation.

Considering the dynamics formulation of Section 3.2.1, we can consider two situations. In the first, the constraint forces and moments λ_d , associated with the required rover motion, are explicitly given, and Eqs. (3.4) and (3.5) do not apply. Then, based on the rest of Eqs. (3.1) – (3.6) the wheel-ground interaction forces and

moments can be expressed as

$$\boldsymbol{\lambda}_w = (\mathbf{A}\mathbf{M}^{-1}\mathbf{A}^{\mathrm{T}})^{-1} \left[\mathbf{A}\mathbf{M}^{-1} \left(\mathbf{c} - \mathbf{B}^{\mathrm{T}} \boldsymbol{\lambda}_d - \mathbf{f}_o \right) - \dot{\mathbf{A}} \dot{\mathbf{q}} + \dot{\mathbf{s}} \right]$$
(3.14)

In the second case, the kinematic specifications associated with the required rover motion are given as per Eqs. (3.4) and (3.5). In this case, the problem can be cast in a more compact form if the definitions below are introduced:

$$\mathbf{D} = \begin{bmatrix} \mathbf{A} \\ \mathbf{B} \end{bmatrix} \qquad \mathbf{d} = \begin{bmatrix} \mathbf{s} \\ \mathbf{b} \end{bmatrix} \qquad \boldsymbol{\lambda} = \begin{bmatrix} \boldsymbol{\lambda}_w \\ \boldsymbol{\lambda}_d \end{bmatrix}$$
(3.15)

where **D** is a $(s + b) \times n$ matrix, while **d** and λ are (s + b)-dimensional arrays. With these definitions the dynamics and kinematics equations of (3.1) - (3.6) can be rewritten as

$$\mathbf{M}\ddot{\mathbf{q}} + \mathbf{c} = \mathbf{D}^{\mathrm{T}} \boldsymbol{\lambda} + \mathbf{f}_{o} \tag{3.16}$$

$$\mathbf{D}\ddot{\mathbf{q}} + \dot{\mathbf{D}}\dot{\mathbf{q}} - \dot{\mathbf{d}} = \mathbf{0} \tag{3.17}$$

$$\mathbf{D\dot{q}} - \mathbf{d} = \mathbf{0} \tag{3.18}$$

In this case, λ turns out to be

$$\lambda = (\mathbf{D}\mathbf{M}^{-1}\mathbf{D}^{\mathrm{T}})^{-1} \left[\mathbf{D}\mathbf{M}^{-1} \left(\mathbf{c} - \mathbf{f}_{o} \right) - \dot{\mathbf{D}}\dot{\mathbf{q}} + \dot{\mathbf{d}} \right]$$
(3.19)

Hence, the wheel-ground interaction reaction representations can be obtained as the first s entries of λ

$$\lambda_w = \lambda_{(1:s)} \tag{3.20}$$

These expressions open up a broad range of possibilities for parametric analyses⁴. We can see that Eqs. (3.14) and (3.20) give the expression of the wheel-ground reactions

⁴We note that for the above formulas it is assumed that both **A** and **D** have full rank; in other words all kinematic relations are independent of each other. For systems where this assumption is not valid, the methods reported by González and Kövecses [108] can be used to determine λ .

as a function of the rover system parameters, the desired operation of the rover, and the kinematics and the wheel-ground interfaces, e.g., slip and sinkage. In the observative model concept, these force representations can play the role of primary variables to characterize the vehicle-terrain interaction behaviour with respect to changes in the parameters and the state of the rover.

If we employ conditions for maximum mobility or requirements for sinkage, then some or all of the entries of \mathbf{s} are given. The above formulas give the required terrain reactions to maintain the specified operating conditions. For example, the transition from maximum mobility to lower mobility occurs when the wheel-ground interface cannot develop the necessary reaction force anymore without slipping. In such a case the wheel starts to slip to accommodate the increased load and the mobility decreases, i.e. the instant velocity centre of the wheel tends to move closer to its axis. The form of Eqs. (3.14) and (3.20) allows one to conduct a parametric study that can provide useful information on where the transition from higher mobility to lower mobility takes place and which rover parameters affect that. This representation allows the analyst to study how the rover design and control parameters can influence this transition. The analysis of how changes in rover parameters can reduce the necessary level of reaction force to maintain the required conditions can help achieve better performance. Regardless of the soil characteristics, if lower tangential reaction forces are required for a manoeuvre, then that would give the vehicle a higher chance of maintaining the no-slip condition. The tangential reaction force components in λ_w , associated with the slip specifications, can be considered as one set of the performance indicators used to characterize the effect of changes in rover parameters on the contact interface behaviour and mobility.

On the other hand, the distribution of the normal reaction force components, also present in λ_w , may also have an immediate influence on the mobility and performance of a rover. These normal reactions can directly influence the maximum tangential

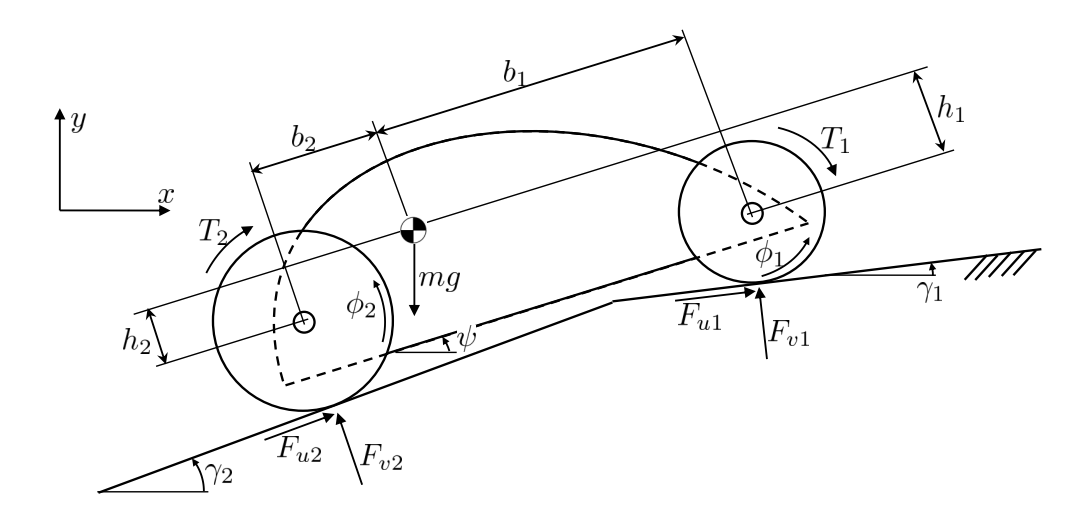


FIGURE 3.2. A five degree-of-freedom, 2-D model of a planetary rover on uneven terrain.

reaction forces that can be developed at the wheel-ground interfaces. This is also supported by general terramechanics observations [36], which can bring about the possibility to develop a performance indicator based on the distribution of the normal reaction forces. These forces can also be important for stability analysis [85]. The ratio of tangential to normal force as a function of rover parameters can be used in optimization procedures to reduce the chance of slip and achieve desired values [77].

3.4 Illustration with simulation

A two-dimensional, five degree-of-freedom multibody model of a rover, illustrated in Fig. 3.2, is used in this section. In the dynamics model of the vehicle the generalized coordinates are the Cartesian coordinates of the CoM of the vehicle, x_G and y_G , the rotation ψ of the body with respect to the x axis, and the rotation of the front and rear wheels with respect to the vehicle main frame, ϕ_1 and ϕ_2 . Parameters b_i and b_i represent the distance of the CoM to the centre of the i^{th} wheel, for i = 1, 2.

The mass of the vehicle body is m_b and its moment of inertia about the axis normal to the plane is I_b . The mass and radius of wheel i are m_i and r_i , respectively. The moment of inertia of wheel i about the axis passing through the wheel CoM, is given by I_i .

The input torques applied to the wheels are T_1 and T_2 ; they are related to each other with a proportionality ratio α as $T_2 = \alpha T_1^{-5}$. The wheel-terrain interaction forces in the tangential and normal directions of the contact for wheel i are F_{ui} and F_{vi} respectively. The contact between ground and wheels can be considered in two alternative ways, as described below.

3.4.1 Predictive model. A predictive model of the rover can be developed using the terramechanics relations in Eqs. (3.7)–(3.10). These relations are based on Bekker's [35] and Wong's work [36] and the modifications proposed by Azimi et al. [1]. The wheel-terrain interaction forces \mathbf{f}_w required by Eq. (3.1) are determined using this predictive model.

The tangential and normal components of interaction are

$$F_{ui} = F_{ti} - R_{ci} \tag{3.21}$$

$$F_{vi} = F_{ni} \tag{3.22}$$

As no constraints are imposed on the system, its degree of freedom is kept as five. This model aims to provide realistic interaction forces; it can only be used in a forward-dynamics setting because Eqs. (3.7)–(3.10) evaluate these forces as functions of the configuration and velocity of the system.

3.4.2 Observative model. An alternative approach lies in specifying the relative motion of the wheels with respect to the ground using the mapping of Eq. (3.2). In this case, array s contains the tangential and normal components

⁵This relation was adopted from the operation conditions of the Juno rover.

of the velocity of the application point of each contact force, and array λ_w contains the wheel-terrain reactions λ_{ui} and λ_{vi} required to maintain the kinematic specifications. The generalized forces representing the wheel-terrain interaction are obtained as $\mathbf{f}_w = \mathbf{A}^T \lambda_w$. This mapping can be used to impose no-slip and no-penetration specifications by setting $\mathbf{s} = \mathbf{0}$. This is equivalent to requiring that the velocity of the points of the wheels in contact with the terrain be zero, thus resulting in the introduction of two kinematic constraints per wheel. Consequently, the degree of freedom of the system is reduced to unity. The model thus obtained can be categorized as an observative model, as introduced in Section 3.3.

For the case of flat terrain ($\gamma_1 = 0$, $\gamma_2 = 0$), the constraint reaction forces can be expressed as functions of the specified forward acceleration of the rover (\ddot{x}_G) and the design and operation parameters, namely,

$$\lambda_{u1} = \frac{1}{\alpha + 1} \left[m_b + 2m_w - \frac{\alpha I_w}{r^2} + \frac{I_w}{r^2} \right] \ddot{x}_G \tag{3.23}$$

$$\lambda_{u2} = \frac{1}{\alpha + 1} \left[\alpha \left(m_b + 2m_w \right) + \frac{\alpha I_w}{r^2} - \frac{I_w}{r^2} \right] \ddot{x}_G \tag{3.24}$$

$$\lambda_{v1} = \frac{1}{b_1 + b_2} \left[-\left(m_b h + 2m_w r + m_b r \right) \ddot{x}_G - m_w g \left(b_1 + b_2 \right) - m_b g b_2 - 2 \frac{I_w}{r} \ddot{x}_G \right]$$
(3.25)

$$\lambda_{v2} = \frac{1}{b_1 + b_2} \left[\left(m_b h + 2m_w r + m_b r \right) \ddot{x}_G - m_w g \left(b_1 + b_2 \right) - m_b g b_1 + 2 \frac{I_w}{r} \ddot{x}_G \right] \quad (3.26)$$

The reaction forces λ_{u1} , λ_{u2} , λ_{v1} , and λ_{v2} correspond to the components of λ_w in Eq. (3.19).

Equations (3.23)–(3.26) provide the expressions of the constraint reaction forces associated with the kinematic constraints imposed on the observative model as functions of the desired acceleration \ddot{x}_G of the vehicle, when it moves on flat terrain. The details of their derivation are provided below.

CHAPTER 3. CONCEPT OF OBSERVATIVE MODELS

The dynamic equations of the five-dof model of the rover are given in Eq. (3.1), with $\mathbf{q} = [x_G, y_G, \psi, \phi_1, \phi_2]^{\mathrm{T}}$. The term of generalized forces can be further expanded into its three components, the dynamic equations thus reading

$$\mathbf{M\ddot{q}} + \mathbf{c} = \mathbf{f}_w + \mathbf{f}_d + \mathbf{f}_o \tag{3.27}$$

The mass matrix of the system is

$$\mathbf{M} = \begin{bmatrix} M_{11} & 0 & M_{13} & 0 & 0 \\ 0 & M_{22} & M_{23} & 0 & 0 \\ M_{31} & M_{32} & M_{33} & M_{34} & M_{35} \\ 0 & 0 & M_{43} & M_{44} & 0 \\ 0 & 0 & M_{53} & 0 & M_{55} \end{bmatrix}$$
(3.28)

with

$$M_{11} = M_{22} = m_b + 2m_w, \quad M_{13} = M_{31} = m_w \left((b_2 - b_1) \sin \theta + 2h \cos \theta \right)$$

$$M_{23} = M_{32} = m_w \left((b_1 - b_2) \cos \theta + 2h \sin \theta \right), \quad M_{33} = m_w \left(b_1^2 + b_2^2 + 2h^2 \right) + I_b + 2I_w$$

$$M_{34} = M_{43} = I_w, \quad M_{35} = M_{53} = I_w, \quad M_{44} = M_{55} = I_w$$

$$(3.29)$$

while the vector of Coriolis and centrifugal terms is

$$\mathbf{c} = \left[\dot{\theta}^{2} m_{w} \left((b_{2} - b_{1}) \cos \theta - 2h \sin \theta \right), \dot{\theta}^{2} m_{w} \left((b_{2} - b_{1}) \sin \theta + 2h \cos \theta \right), 0, 0, 0 \right]^{\mathrm{T}}$$
(3.30)

where the masses of the wheels have been assigned as $m_1 = m_2 = m_w$, their moments of inertia as $I_1 = I_2 = I_w$, and $h_1 = h_2 = h$.

The last two components of the generalized forces are given below:

$$\mathbf{f}_d = [0, 0, 0, T_1, \alpha T_1]^{\mathrm{T}} \tag{3.31}$$

$$\mathbf{f}_{o} = [0, m_{b}g + 2m_{w}g, m_{w}g (b_{1}\cos\theta - b_{2}\cos\theta + 2h\sin\theta), 0, 0]^{\mathrm{T}}$$
(3.32)

The kinematic relations imposing no-slip and no-penetration used in the definition of the observative model are given below. The no-slip condition on flat terrain is

$$\dot{\phi}_1 = \dot{x}_G/r_1
\dot{\phi}_2 = \dot{x}_G/r_2$$

$$\Rightarrow \qquad \ddot{\phi}_1 = \ddot{x}_G/r_1
\ddot{\phi}_2 = \ddot{x}_G/r_2$$
(3.33)

Similarly, for the no-penetration condition we have

$$\dot{y}_G = 0
\dot{\psi} = 0 \qquad \Rightarrow \qquad \ddot{y}_G = 0
\ddot{\psi} = 0 \qquad (3.34)$$

The imposition of these four kinematic constraints reduces the degree of freedom of the system to unity. In this case, the motion of the system can be fully determined upon specifying the acceleration \ddot{x}_G of the rover. The reaction forces for the no-slip and no-penetration constraints are the tangential (λ_{ui}) and normal (λ_{vi}) reactions on each wheel-ground contact point. These unknown reaction forces and the required applied torque are now grouped in an array $\lambda = [\lambda_{u1}, \lambda_{u2}, \lambda_{v1}, \lambda_{v2}, T_1]^T$. Reordering Eq. (3.27) as

$$\mathbf{f}_w + \mathbf{f}_d = \mathbf{M}\ddot{\mathbf{q}} + \mathbf{c} - \mathbf{f}_o \tag{3.35}$$

leaves all the unknown terms on the left hand side, while the right hand side is fully known. In order to find λ , a transformation from array $\mathbf{a} = \mathbf{f}_w + \mathbf{f}_d$ to λ can be used.

The virtual work of the unknown forces is

$$\delta W = \lambda_{u1} \left(\delta x - \delta \psi \left(b_1 \sin \psi - h \cos \psi \right) + \left(\delta \psi + \delta \phi_1 \right) r_1 \right)$$

$$+ \lambda_{u2} \left(\delta x - \delta \psi \left(-b_2 \sin \psi - h \cos \psi \right) + \left(\delta \psi + \delta \phi_2 \right) r_2 \right)$$

$$+ \lambda_{v1} \left(\delta y + \delta \psi \left(b_1 \cos \psi + h \sin \psi \right) \right) + \lambda_{v2} \left(\delta y + \delta \psi \left(-b_2 \cos \psi + h \sin \psi \right) \right)$$

$$+ T_1 \delta \phi_1 + \alpha T_1 \delta \phi_2$$
(3.36)

while the corresponding term in the dynamic equations is

$$\mathbf{a} = \mathbf{f}_w + \mathbf{f}_d = \frac{\partial \delta W}{\partial \delta \mathbf{q}} = \begin{bmatrix} a_1 & a_2 & a_3 & a_4 & a_5 \end{bmatrix}^{\mathrm{T}}$$
(3.37)

with

$$a_{1} = \lambda_{u1} + \lambda_{u2} \quad a_{2} = \lambda_{v1} + \lambda_{v2}$$

$$a_{3} = \lambda_{u1} \left(h \cos \psi - b_{1} \sin \psi + r_{1} \right) + \lambda_{v1} \left(b_{1} \cos \psi + h \sin \psi \right)$$

$$+ \lambda_{u2} \left(b_{2} \sin \psi + h \cos \psi + r_{2} \right) + \lambda_{v2} \left(h \sin \psi - b_{2} \cos \psi \right)$$

$$a_{4} = \lambda_{u1} r_{1} + T_{1} \quad a_{5} = \lambda_{u2} r_{2} + \alpha T_{1}$$
(3.38)

It is possible to relate \mathbf{a} and $\boldsymbol{\lambda}$ through a transformation $\mathbf{v} = \mathbf{J}\dot{\mathbf{q}}$, where \mathbf{v} contains the velocities of the application points of forces $\boldsymbol{\lambda}$. Matrix \mathbf{J} is

$$\mathbf{J} = \begin{bmatrix} 1 & 0 & h\cos\psi - b_1\sin\psi + r_1 & r_1 & 0\\ 1 & 0 & b_2\sin\psi + h\cos\psi + r_2 & 0 & r_2\\ 0 & 1 & b_1\cos\psi + h\sin\psi & 0 & 0\\ 0 & 1 & -b_2\cos\psi + h\sin\psi & 0 & 0\\ 0 & 0 & 0 & 1 & \alpha \end{bmatrix}$$
(3.39)

In this case **J** is non-singular, the relation between the two sets of forces then being

$$\lambda = \mathbf{J}^{-\mathrm{T}}\mathbf{a} \tag{3.40}$$

and Eq. (3.40) can be substituted into Eq. (3.35), which yields the expression of the unknown forces:

$$\lambda = \mathbf{J}^{-\mathrm{T}} \left(\mathbf{M} \ddot{\mathbf{q}} + \mathbf{c} - \mathbf{f}_o \right) \tag{3.41}$$

Finally, imposing constraint equations (3.33) and (3.34) onto Eq. (3.41), and setting $\psi = 0$ and $r_1 = r_2 = r$ yield the parametric expression of the reaction forces shown in Eqs. (3.23)-(3.26) and the applied torque as:

$$T_1 = \frac{-r}{\alpha + 1} \left(m_b + 2m_w + \frac{2I_w}{r^2} \right) \ddot{x}_G \tag{3.42}$$

3.4.3 Simulation results. The two models described above are compared by means of simulation. The purpose of the observative model is to capture the way in which reaction forces vary when the system parameters are modified. The trends obtained are compared to the results from the predictive model of Section 3.4.1. It will be shown that there is a direct relation between the actual level of slip that occurs during operation and the magnitude of the tangential reaction force the terrain must be able to develop to avoid slip. The tangential reaction force can be considered as an indicator for rover mobility. Three design and control parameters of the rover have been studied. The first parameter under study is the ratio α that characterizes the distribution of the resultant applied torque among the wheels. The wheel radius r and the displacement of the CoM of the rover with respect to the geometric centre of the vehicle along its longitudinal axis are the two other design parameters to be assessed.

The effects of the variation of these parameters on the tangential reaction forces were studied in the simulation when the rover moves on flat terrain. First, the wheel-terrain interaction forces F_{ui} and F_{vi} were determined using the predictive model with terramechanics relations (3.7)–(3.13) and the terrain parameters in Table 3.1.

Table 3.1. Soil parameters used for the predictive model

$$n$$
 c ϕ k_c k_ϕ K
 $(-)$ (N/m^2) (deg) (N/m^{n+1}) (kN/m^{n+2}) (m)
 1 800 37.2 1370 814 0.025

Forward dynamics simulation was conducted to compute acceleration and terrain reaction forces for given input torques applied to the wheels. The total applied torque T was distributed among the front and rear axles according to the expressions:

$$T_1 = \frac{1}{1+\alpha}T \qquad T_2 = \frac{\alpha}{1+\alpha}T \qquad (3.43)$$

Torque T followed a trapezoidal profile starting from zero at t=1 s, increased linearly with time to 11 Nm until t=2 s, remained constant during the next 10 s, and then ramped down to 0 Nm over 1 s. Simulation studies showed that the vehicle reaches a constant acceleration \ddot{x}_c between t=2.5 s and t=12 s. The tangent reaction forces during this period were evaluated using Eq. (3.21).

In order for the reaction forces obtained to be comparable, the predictive and observative models need to be considered for the same rover motion. Acceleration \ddot{x}_c obtained with the predictive model, is consequently set to specify the desired motion of the rover for the observative model. Then, the required constraint reaction forces are evaluated using Eq. (3.19). For this particular rover, the tangential reaction forces can also be determined using Eqs. (3.23) and (3.24) as functions of the system parameters and the desired acceleration \ddot{x}_c .

First, the effect of the torque distribution parameter α was studied. The simulation procedure described above was repeated for a range of values of α and the tangential and normal forces were determined using the two models. Also, for each value of α the magnitude of the slip was calculated based on the predictive model. It was confirmed that changes in α had no significant effect on the normal forces. This is derived from the condition that both models must satisfy the dynamic equilibrium of the rover in the vertical direction, which is independent of α . However, the applied torque directly affects the force equilibrium of each wheel and, consequently, the resultant tangential reaction force. The net tangential force F_{ui} obtained with the predictive model and the tangential constraint force λ_{ui} given by the observative one are compared for different values of α in Fig. 3.3. The figure on top shows

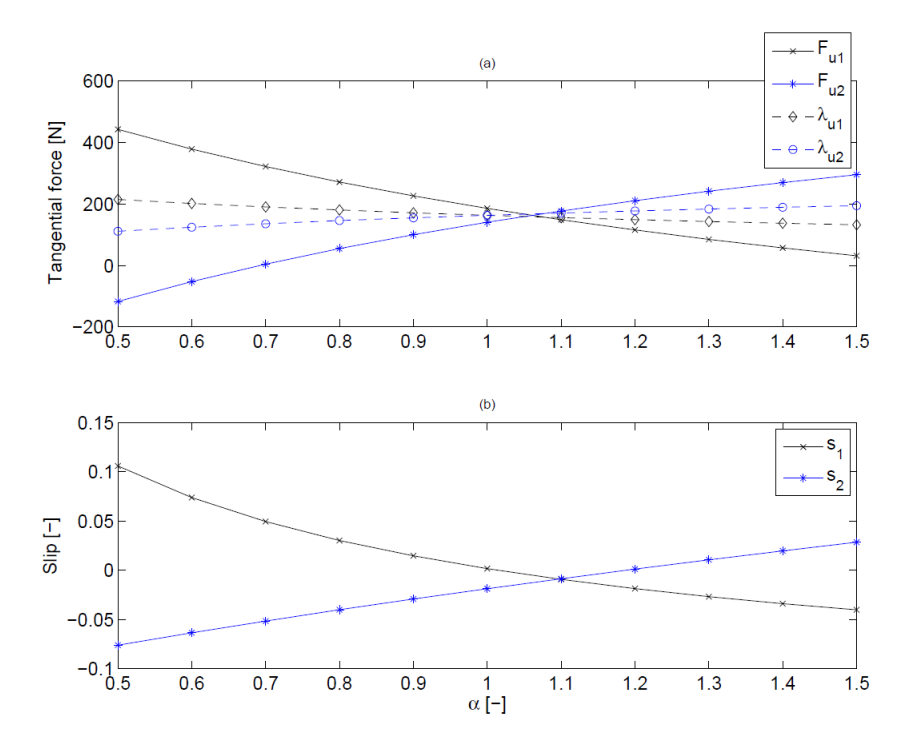


FIGURE 3.3. Effect of the variation of the torque distribution parameter α on (a) the net tangential force obtained with the observative (dashed lines) and predictive models (solid lines) and (b) the slip at the wheel-terrain contact point obtained with the predictive model

that the trends of change in the tangential forces obtained from the predictive and observative models due to the variation of α are similar. It has to be noted that the observative model is not used here to determine the value of α for which the net traction force at the front and rear wheels is the same. This model is neither used to determine the torque distribution that results in zero slip at the wheel-terrain interfaces. These values depend on the terrain characteristics and cannot be found with the observative model. However, the change in the wheel slip due to the variation of α (Fig. 3.3b) does follow the same trend as the tangential reaction force. These results tally with the expectation that if the tangential forces obtained from the observative model are high, the terrain is less likely to withstand this force and

CHAPTER 3. CONCEPT OF OBSERVATIVE MODELS

the system is more prone to developing slip. The larger the constraint forces λ_{ui} , the higher slip to be expected in reality.

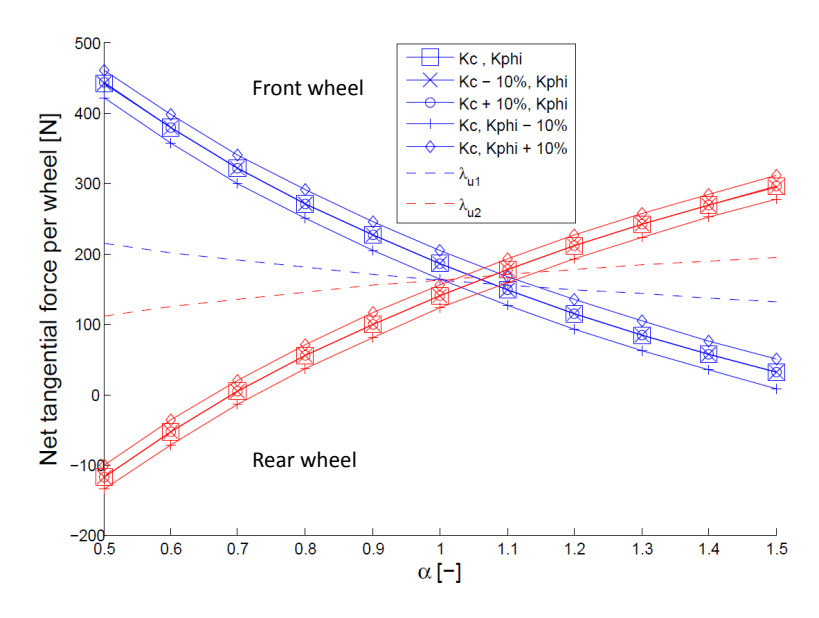


FIGURE 3.4. Effect of the variation of the torque distribution parameter α on the net tangential force obtained with the predictive model for different soil parameters (solid lines) and the observative model (dashed lines)

The observative model is able to indicate these effects of changes in rover parameters without the need to have a detailed representation of the soil properties. In order to investigate this in more detail, the simulation with the predictive model was repeated varying soil parameters k_c and k_{φ} from their original values given in Table 3.1. These parameters appear in the normal stress formula in Eq. (3.11). The variation of these parameters represents soils with different cohesive and frictional properties. As shown in Fig. 3.4, with different values of soil parameters, reaction forces obtained from terramechanics models follow the same trend as determined via the observative model.

Figure 3.5 shows the net tangential force developed at each wheel with the same value of the input torque, for different values of the wheel radius r. The slip developed

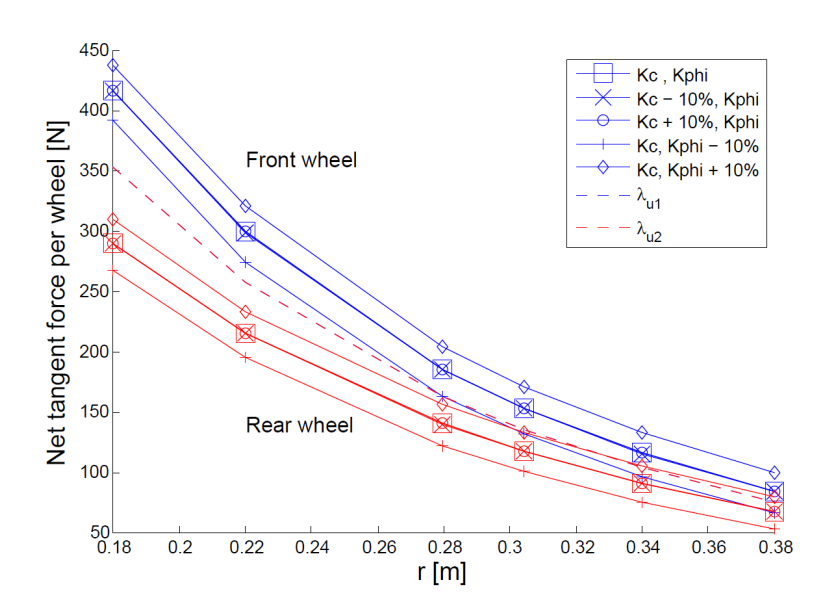


FIGURE 3.5. Effect of the variation of wheel radius on the net tangential force obtained with the predictive model for different soil parameters (solid lines) and the observative model (dashed lines), for $\alpha = 1$

at each wheel is important to understand this figure. It can be seen that, when using terramechanics models, larger wheels result in smaller values of the net tangential force and, consequently, in lower slip. This is to be expected, as the input torque is kept constant for different values of the wheel radius. The purpose of this study was not to find an optimum wheel radius from the point of view of rover performance, but rather to highlight that the observative model is able to capture the trends that are generally observed. Again, variations in the soil parameters do not affect the validity of the results obtained with the observative model.

The position of the centre of mass of the rover has to be considered as well in the study of mobility. Information about its effect on the performance of the system can be useful for design and operation. For the case of reconfigurable systems, for example, mass distribution can be changed while the robot is in operation in order to improve traction or stability. This reconfiguration requires knowledge of the way in which a change in configuration will influence the soil interaction.

In some cases, the study of how the CoM position affects mobility can be carried out using normal forces as performance indicators. It is obvious that the change of CoM position has an immediate effect on the normal force distribution among the wheels. In the case of non-redundant supporting in the normal direction, the normal forces obtained from both the predictive and observative models should be the same. Thus, without resorting to the complex and computationally expensive terramechanics relations, the mobility of a rover during operation can be studied with the aid of an observative model. The use of normal reaction forces as indicators is illustrated in Section 3.5 with an experimental example.

3.5 Experimental results

The experiments reported here were conducted on the Juno rover prototype, developed by Neptec [109], operating on soft soil, as shown in Fig. 3.6.





FIGURE 3.6. Juno Rover with additional mass elements in configurations A (left) and B (right)

The model of the rover can be developed in the form given previously in Section 3.4. The rover is instrumented with wheel encoders, inertial measurement units

(IMU), and a positioning system that provides the 3-D position of the rover in global coordinates. The two wheels on each side of the rover are coupled; hence, they are constrained to have the same angular velocity. Given that the distance between the two wheel centres is constant, on flat terrain they experience the same slip. Simulations with the terramechanics relations described in Section 3.2.3 showed that, in such a case, the highest resultant traction force will be developed if the normal load distribution on the wheels is uniform. This is illustrated in Fig. 3.7. The plots

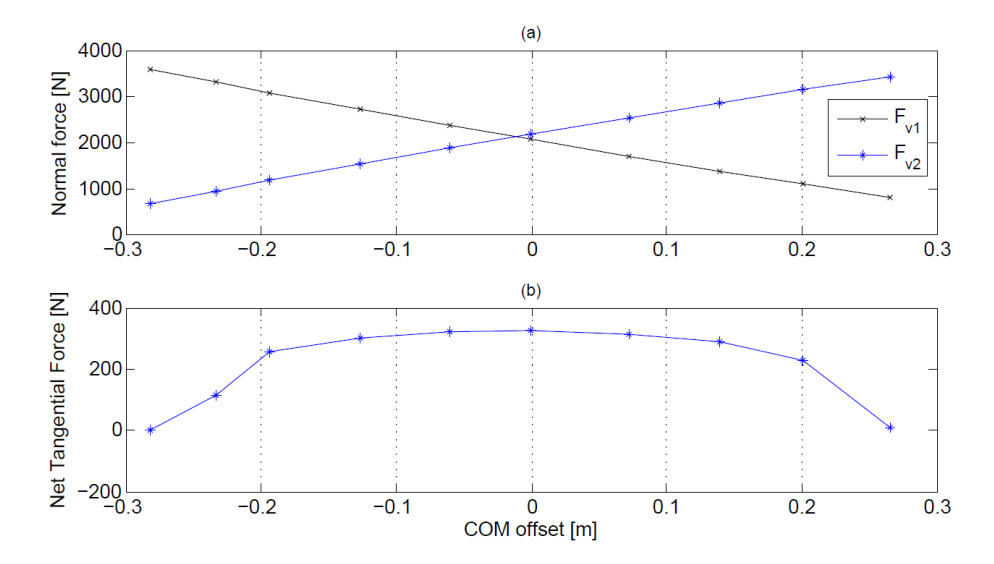


FIGURE 3.7. Effect of the CoM position of the Juno rover on (a) the normal force and (b) the net tangential force at the wheel-soil interface, as predicted by simulation with Azimi et al. model [1]

show that when travelling on flat terrain the net tangential force obtained using the terramechanics model reaches its maximum when the normal forces experienced by the wheels are identical. This allows the use of the normal force distribution as a relevant performance indicator in analyzing the mobility of this particular rover.

The load distribution can be influenced by changes in the configuration of the rover. The position of the CoM resulting in a uniform normal force distribution can be found employing the observative model described in Section 3.4.2. Based

on the equations describing the normal forces, Eqs. (3.25) and (3.26), the values of parameters b_1 and b_2 that provide a uniform force distribution can be found. Given two different mass distributions for the rover, it is possible to select the one that provides larger traction forces just by comparing the normal wheel-ground reactions evaluated with the simple observative model. To illustrate this, several different configurations of the Juno rover were compared in terms of the drawbar pull the vehicle was able to develop. The design of the platform of the Juno rover does not allow for direct geometric reconfiguration. However, as additional components, such as manipulator arms or payload, will be present in real-life missions, the configuration of these elements is bound to change the position of the CoM. Therefore, in order to obtain different configurations with the same rover chassis, an additional set of mass elements was placed on different points on the rover platform, as shown in Fig. 3.6, making sure that the total mass was the same in all experiments.

The mass of the rover was found to be 317.5 kg; additional mass elements, including attachments, weighed a total of 111.4 kg, resulting in a total mass of 428.9 kg. Therefore, changing the position of the mass elements on the rover platform had a significant effect on the horizontal position of the CoM of the overall rover system. Selected results for two positions of the additional mass are shown in Fig. 3.8 and analyzed next. The configuration in which the mass elements are located on the front tip of the longitudinal axis of the rover is labeled A (Fig. 3.6a). Configuration B refers to the arrangement where mass elements are placed at the back end of the interface plate (Fig. 3.6b). The distance between the two positions of the mass elements is 0.91 m.

During experiments, the rover was commanded to move forward with a constant speed on soft flat soil, i.e. constant wheel angular velocity of 0.5 rad/s. The wheel encoders confirmed that the wheels operated at the expected angular velocity. A

variable, controlled horizontal load was applied to the frame of the rover. The magnitude of this force was adjusted during operation to keep the velocity of the rover within the same range for all the experiments; the value of the force was recorded by a digital load cell. Experimental results were selected from runs where the motor currents were found to be the same for both configurations, so the input power of the system for the two trials can be considered constant between experiments. Under these conditions, the applied load represents the drawbar pull that the rover is able to carry for a given value of input power, for each configuration.

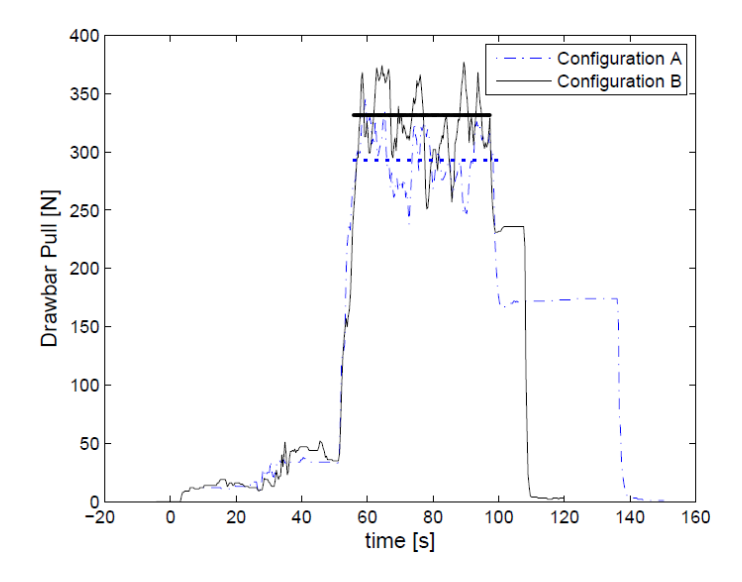


FIGURE 3.8. Time history of the loads applied to the rover in experiments with configurations A and B. The average values of the loads during the representative period of the motion are superimposed on the figure as straight lines

As an example, Fig. 3.8 shows the time history of the force measured by the load cell obtained during two experiments, with configurations A and B. The difference in normal forces between front and rear axes was determined using Eqs. (3.25) and (3.26) of the observative model and found to be 1571.6 N with configuration A. For configuration B the difference between normal force components was reduced to

812.3 N. The average value of the applied force was determined for each case based on the digital load cell measurement, as shown in Fig. 3.8 with horizontal straight lines. For configuration A, the rover was able to develop an average drawbar-pull force close to 290 N (represented in Fig. 3.8 with a dashed line); for configuration B that value increased to approximately 340 N (represented by a solid line in the figure). These values show that configuration B is more suitable for development of higher traction, or equivalently, for developing higher drawbar pull. The results from experiments with the Juno rover follow the trend predicted by the simulation results shown in Fig. 3.7.

The experimental results showed that an uneven distribution of normal forces results in different traction forces developed at each wheel. The kinematic relation between the angular velocities of the two wheels on each side of this rover enforces the same slip at each wheel-terrain contact. The traction force is a function of normal force and slip; for the same value of slip, a smaller normal force provides a lower traction force, although this relation is not linear. If it were, the tangential force in Fig. 3.7 would be constant, regardless of the normal force distribution. However, in this figure it can be appreciated that the summation of tangential forces in the system reaches its maximum when the two tangential force components are equal due to the balancing of the normal force distribution. The experimental results support this statement, which confirms that the distribution of normal forces can be used as a performance indicator for improving the vehicle mobility. This type of indicators helps us find the configuration which provides higher drawbar pull without the need to go through detailed computation of terrain reactions, even though they do not provide the exact value of that drawbar pull. This is a key idea behind the use of observative models.

CHAPTER 4

Effect of Normal Force Distribution on Rover Performance

4.1 Introduction

Optimizing vehicle mobility is an important goal in the design and operation of wheeled robots on soft soil. As discussed in Chapter 3 slip reduction has been proposed in several works as a means to achieve this objective [14, 77]. In these papers, the interaction of wheel with hard ground is modelled using the assumption of Coulomb friction while the ratio of tangential to normal forces at the wheel-ground contact is minimized with the goal of reducing the risk of developing slip. While not directly dealing with soft soil modelling, these papers highlight the need for keeping wheel slip under control in order to improve the vehicle behaviour..

When soft terrain enters the picture, the phenomena at the wheel-terrain interface become more complex and Coulomb friction models can no longer be used to describe them accurately. Then, two options are left to predict the effect of design and actuation parameters on robot mobility. The first one is turning to detailed models of the contact interface. These models are typically used in forward dynamics simulation settings and require an accurate knowledge of the set of parameters that characterize the terrain properties and which are not always accessible. The second option consists in finding design and operation guidelines of general validity. These can offer simple means to compare alternative designs and can be used to define objective functions for design, operation, and control.

The effect of the normal force distribution on mobility on soft soil has been mentioned in the literature [37, 78, 89, 92, 93]. The conclusion of theses studies is that on a homogeneous terrain, traction is maximized if the normal forces are the same for all the wheels. However, as discussed in Chapter 2 the focus of some of these studies is on the operation of mobile robots on rigid ground. The ones which consider operations on soft soil mainly use experimental data to support the above conclusion. In-depth analysis of the relation between the normal and tangential reaction force of soft terrains is not provided in the above references to support the effect of normal force distribution on rover mobility.

The level of slip must be considered together with the terrain reaction forces when studying mobility. Reaching higher slip values can be used as strategy to develop more traction, e.g., by applying a greater driving torque to the wheels. However, the total drawbar pull goes down when the slip ratio goes beyond a certain value [94]. In the tests reported [110], the engineering model of Spirit and Opportunity was placed on a variable terrain tilt platform to measure the climbing ability for different slip ratios. It was found that the drawbar pull-slip curve is nonlinear. It will be shown in Section 4.2 that the actual shape of this plot depends on the properties of the terrain and the condition of the wheel-terrain interaction.

Some strategies exist to determine the climbing ability of a rover via estimation of the soil parameters and the slip ratio of the wheels [111]. The effect of chassis and wheel design on climbing ability of rovers was investigated as well in several papers

[112], [113]. However, despite being mentioned several times in the literature as a factor to consider during mobility evaluation, normal force distribution has only been studied in a systematic way in few references, e.g., [114] with regard to its role in traction on soft soil. The purpose of the presented work in this chapter is to provide a detailed analysis of the relation between the internal force distribution in a robot chassis, more specifically the normal force distribution among the wheels, and the robots mobility. The relation between the normal force at a wheel and the drawbar pull that it can develop was used as a starting point for this study. Besides providing a justification for the effect of normal force distribution on mobility, the operation conditions under which this effect is most critical have been identified in this chapter. A general framework, not limited to the study of a specific vehicle design or type of terrain, was adopted to ensure the general validity of the results. This chapter is an extension of the work presented in [115] and describes the results in more details and explores the validity of the proposed approach in a broader scope.

4.2 Analysis of a single wheel moving on soft soil

In order to study the relation between tangential and normal forces developed at a wheel-terrain interaction the terramechanics model described in Section 3.2.3 is used. The drawbar pull (DBP) developed by the wheel is defined as:

$$F_D = F_t - R_c \tag{4.1}$$

Through terramechanics relations it is possible to establish how a change in the normal force F_n affects the ability to develop drawbar pull F_D and consequently affect the rover mobility. Equation (3.13), which relates normal and shear stresses under the wheel, is rewritten here for quick reference:

$$\sigma(\theta) = \left(\frac{k_c}{b} + k_\phi\right) \zeta(\theta)^n$$

This shows that the shear stress τ increases with the normal stress σ . The relation between the two is nonlinear, as it includes an exponential term that is, in turn, a function of the slip s. This implies that the relation between F_D and F_n is of nonlinear nature. Wheel slip and soil properties give parameters to define the exact shape of that curve.

4.3 Implementation of terramechanics relations in dynamic simulation

In order to determine the effect of slip and soil parameters on the relation between the tangential and normal forces, the multibody library described in Appendix B was used. In this section the necessary considerations for including terramechanics models in the simulation are described.

Terramechanics relations require the state of the system (generalized coordinate and velocity) as their input to evaluate the reaction forces with terrain. As shown in Fig. 4.1 generalized coordinates and velocities are sent at each time-step to the terramechanics model. Based on these inputs the wheel slip and sinkage are computed. The relation for wheel slip was given in Eq. (3.12) which is $s = (r\omega - v_t)/r\omega$. The values of v_t and ω need to be extracted from the velocity components of the wheel expressed in its local coordinate frame. However, in this library one has access to the generalized velocities of the bodies expressed in the global reference frame. To this end, the transformation matrix between the global reference frame and the local coordinate frame of the wheel needs to be known. This transformation matrix can be readily obtained since the rotation matrix of all the bodies is available in the BODIES data-structure. The wheel sinkage is determined as a function of the

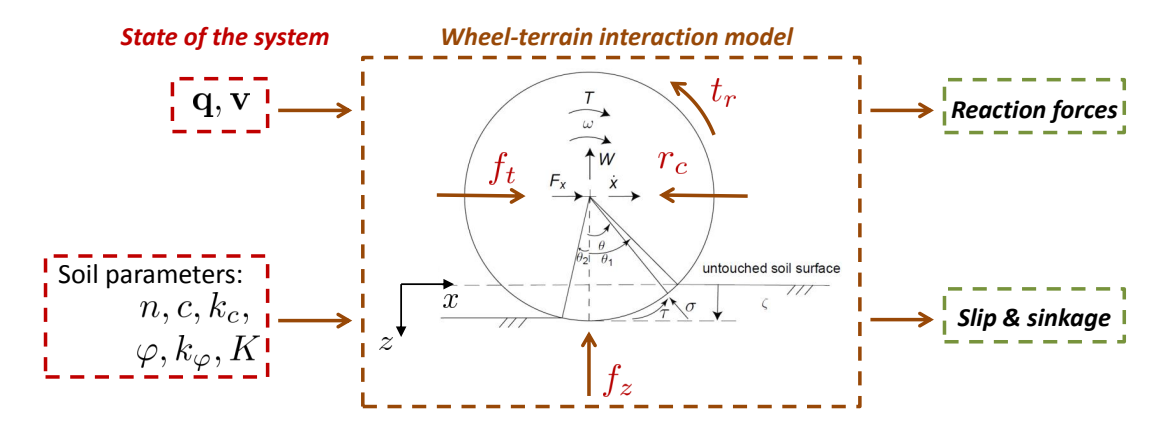


FIGURE 4.1. Input and output variables to terramechanics model

coordinates of the wheel centre and the ground in the direction normal to the plane of the wheel-ground contact. Additionally, the wheel and soil properties for each wheel-soil interaction must be available to evaluate the terrain reaction forces.

The output of the terramechanics model for each wheel includes the ground traction force F_t , resisting force R_c , normal force F_n , and resisting torque T_r . These represent scalar components that are interpreted in the local coordinate frame of the wheel, while the components in \mathbf{f}_a in Eq. (B.18) are generally interpreted in the global reference frame. Therefore, in order to include the terrain reaction forces in \mathbf{f}_a the transformation matrix from the local coordinate frame of the wheel to the global reference frame has to be used. Furthermore, the sign of the scalar values of the terrain reactions obtained from the terramechanics relations depends on the direction of motion of the wheel. This has to be considered in simulation. For example, resisting force and resisting torque must always oppose the direction of translational and angular velocity of the wheels, respectively. The above procedures are automatically considered in the developed library when calling terramechanics functions.

An additional consideration in the implementation of terramechanics models in the library was to deal with large discontinuities in these forces. The reaction forces

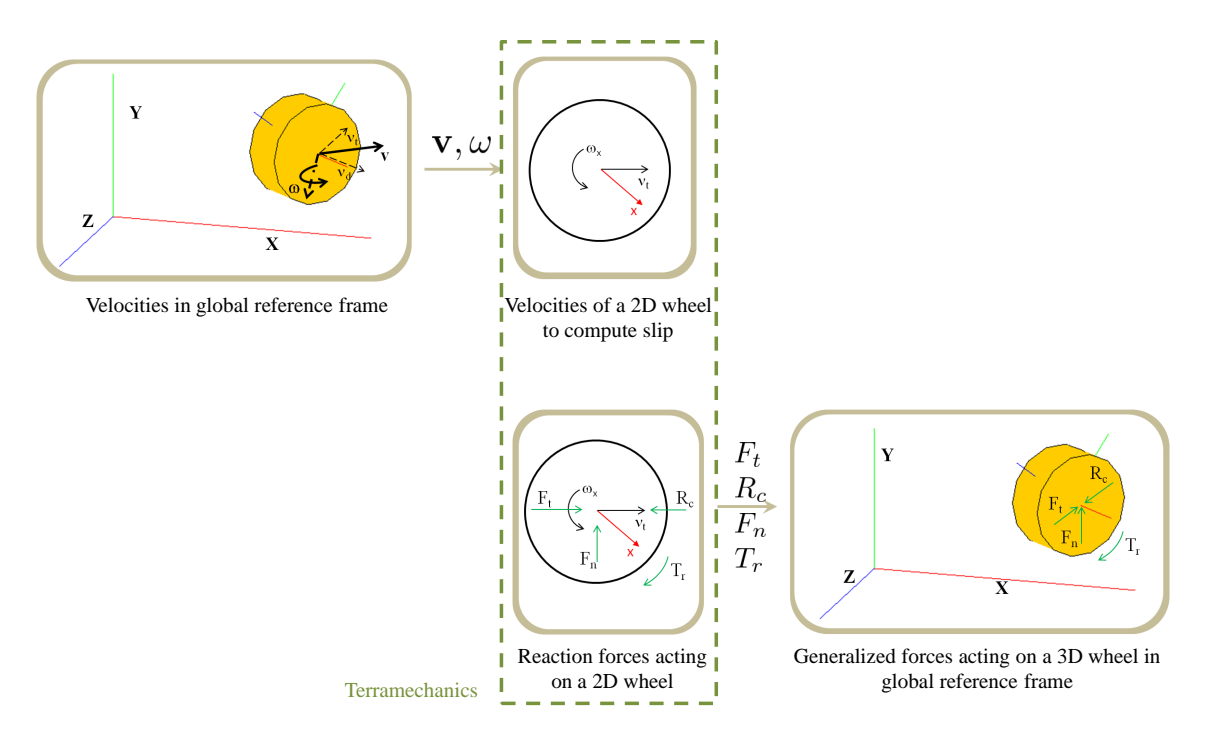


FIGURE 4.2. Transformation of coordinates and velocities from the global reference frame to the wheel local frame and transformation of the terrain reactions from the wheel local frame to the global reference frame

change sign depending on the direction of motion of the wheel, which introduces difficulties in simulation procedure, especially in wheel low-speed operation. Details of the assumptions and modifications to the original terramechanics model to address this issue are available [116]. With the aid of these modifications it is possible to simulate the motion of a wheel on soft soil for all of the following possible cases and during the transition between them:

- $v_t > 0, r\omega > 0$
 - $-r\omega > v_t$: Driving forward
 - $-v_t > r\omega$: Braking forward
- $v_t < 0, r\omega < 0$
 - $-|r\omega| > |v_t|$: Driving backward

- $-|v_t| > |r\omega|$: Braking backward
- $v_t > 0$, $r\omega < 0$: Skidding forward
- $v_t < 0, r\omega > 0$: Skidding backward

Braking forward and backward only differ in the direction of motion but are of the same nature. In the simulation of multi-axle vehicles on soft soil, multipass effect also needs to be considered. The multipass effect is implemented in the library in the form of an additional function which is called before the terramechanics function. This function evaluates the changes in the soil parameters as functions of multipass parameters of that specific soil, number of passes, and the slip ratio of the wheel in the previous pass. In this way the main terramechanics function remains unchanged. Details on the multipass model used in this library are given in Section 4.12.

As explained earlier, terramechanics relations require access to states of the bodies and their rotation matrices in order to compute the terrain reactions. This level of access is not allowed in many software packages, which explains part of the challenge in implementation of wheel-terrain interaction models in some available packages, as addressed in our library. Also, in this library it is possible to store all the internal variables related to the wheel-soil interaction for the entire simulation time. These variables, such as slip and sinkage, can be important for analysis purposes.

4.3.1 DBP and normal force relation. A set of simulations of the motion of a single wheel moving on soft terrain was carried out using terramechanics relations to model the wheel-terrain interaction. The wheel properties were chosen to match those of the RCP rover. The wheel properties, mass m = 2.55 kg, radius r = 0.175 m, and width b = 0.15 m, were chosen to match those of the rover prototype described in Section 4.5. The slip at the wheel-ground interface was specified through kinematically guiding the wheel by setting the velocity of the wheel centre v_t and its angular velocity ω in planar motion as depicted in Fig. 4.1. The constraint that

| Soil type | n | c | ϕ | k_c | k_{ϕ} | K |
|-----------|-----|-----------------|--------|---------------------------------|-------------------------|-------|
| | (-) | $({\rm N/m^2})$ | (deg) | $(\mathbf{N}/\mathbf{m}^{n+1})$ | $(\mathrm{kN/m}^{n+2})$ | (m) |
| A | 1 | 220 | 33.1 | 1400 | 2000 | 0.015 |
| В | 1 | 220 | 33.1 | 1400 | 820 | 0.015 |

Table 4.1. Set of soil parameters used for study of F_D -vs.- F_n curves

is used to specify the angular and translational velocities of a wheel is referred to "rigidly guided wheel" in the simulation tool and is introduced in Section B.4.2. This emulated the single-wheel testbed conditions. The total load F_n supported by the wheel was adjusted for each simulation, within a range of up to 600 N. The simulation output was the drawbar pull developed at each numerical test. Table 4.1 shows two sets of soil parameters used for the terramechanics relations in the simulations.

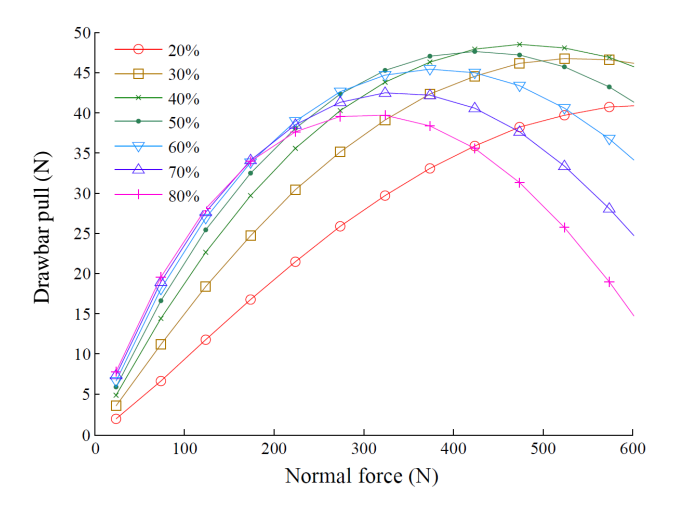


FIGURE 4.3. F_D -vs.- F_n relation for a single wheel with different slip ratios on soil "B"

Type "A" is an estimation of the soil properties used in the experiments with the RCP. These experiments are describes in detail in Section 4.6 and the estimation algorithm is explained in Appendix A. Type "B" is a theoretical variation of type

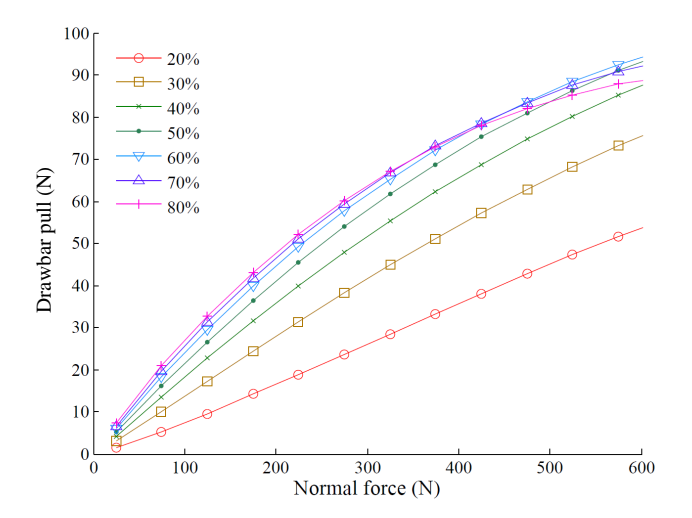


FIGURE 4.4. F_D -vs.- F_n relation for a single wheel with different slip ratios on soil "A"

"A" which only differs in the value of k_{ϕ} . Although such soil with the parameters listed under type "B" may not physically exist the objective of introducing type "B" was to study the effect of k_{ϕ} on system behaviour via simulation study. The F_{D} -vs.- F_{n} curves for the these types of soil are shown in Figs. 4.3 and 4.4. These plots show that for low values of F_{n} the relation between normal force and drawbar pull is practically linear for the entire range of slip ratios. On the other hand, higher normal loads on the wheel and higher slip, e.g., over 50%, bring along significant deviations from linearity. These are accentuated by low values of the k_{ϕ} modulus, which was found to be the most influential of all terrain parameters with regard to the curvature of the plotted lines.

4.4 Normal force dispersion as mobility indicator

The mobility of a wheeled robot depends on its ability to generate a required amount of drawbar pull while keeping the slip ratio low. The discussion in the previous section points out that the normal force at each wheel of a robot affects the developed tangential force and in turn, the total drawbar pull that the vehicle provides. The terrain normal reactions have to balance the inertial and applied forces on the rover. However, changing the normal load distribution among the wheels can result in different values of the total drawbar pull developed by the vehicle. The effect of normal force distribution can be studied using the F_D -vs.- F_n curve. An example for a planar three-axle system in 2-D motion is shown in Fig. 4.5, where the F_D -vs.- F_n curve has a generic nonlinear shape similar to those in Figs. 4.3 and 4.4.

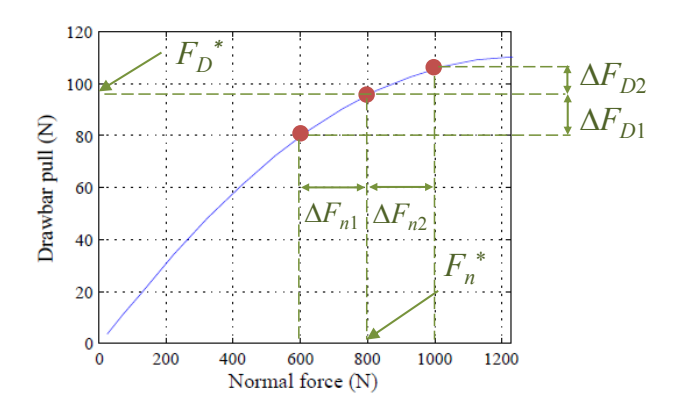


FIGURE 4.5. Effect of non-uniform normal force distribution on the total available drawbar pull

If the three axles are moving with the same angular speed, and the terrain under the vehicle is homogeneous, then the same curve can be used for all the wheels. In this case, an even normal load distribution would be the one in which $F_{n1} = F_{n2} =$ $F_{n3} = F_n^*$. A normal load transfer between the first and second axles of the robot $(\Delta F_{n1} = -\Delta F_{n2})$ will result in $\Delta F_{D1} < 0$ and $\Delta F_{D2} > 0$ in the drawbar pull at these wheels. If the slope of the F_D -vs.- F_n curve decreases consistently with F_n , i.e. the curve is sublinear, then $|\Delta F_{D2}| < |\Delta F_{D1}|$, which will yield a lower total available drawbar pull for the same slip values. In other words, in the uneven configuration the slip should become higher in order to achieve the same drawbar pull delivered by its balanced counterpart, where the normal forces are uniformly distributed among the wheels.

For the case of a wheeled robot operating on homogeneous terrain, the F_D -vs.- F_n relation will be the same for all the wheels if they are identical and have the same slip. These assumptions can be considered close enough to reality for a broad range of operating conditions.

We define here a performance indicator termed the Normal Force Dispersion (NFD), denoted by η , to measure and quantify the uniformity of the normal force distribution. This performance indicator is the standard deviation of the normal forces at the wheel-terrain contact interfaces, namely,

$$\eta(F_{n1}, \dots F_{np}) = \sqrt{\frac{1}{p} \sum_{i=1}^{p} (F_{ni} - \mu)^2}$$
(4.2)

where p is the number of wheels of the vehicle and μ is the average normal force:

$$\mu = \frac{1}{p} \sum_{i=1}^{p} F_{ni} \tag{4.3}$$

An even distribution of normal forces $(F_{n1} = F_{n2} = \dots = F_{np})$ would result in $\eta = 0$, which is the optimum configuration in terms of developed drawbar pull for operation on homogeneous terrain and assuming that all their wheels of the vehicle have the same slip ratio. Quantifying the unevenness of the load distribution via NFD facilitates the comparison of different rover configurations in terms of their mobility, while it may avoid the need for a detailed knowledge of the terrain properties. The exact value of the terrain reaction is not required since only information on the relative change in the performance of the rover is enough to make design and operation decisions. The index can be used to determine which configuration produces the most uniform load distribution among the wheels for a given manoeuvre or operation.

As a conclusion, it can be stated that making the normal force distribution more uniform will have a noticeable effect on the drawbar pull when the F_D -vs.- F_n curve shows an apparent sublinear relationship. This is the case of operation conditions where high slip values are expected to develop, such as slope climbing, or in the presence of loose terrain with low values of k_{ϕ} . In other situations, with an almost linear F_D -vs.- F_n plot, such as when moving on flat ground or climbing mild slopes on cohesive terrain, the uniformity of the normal load distribution will still have a positive effect on rover mobility, but this may not be very significant.

4.5 Application of the concept

The NFD was used to study the mobility of the Rover Chassis Prototype (RCP), a six-wheeled rover prototype developed by the Robotics and Automation unit of MDA (MacDonald, Dettwiler and Associates Ltd.) shown in Fig. 4.6. The rover was built as an engineering model for various experimental purposes.

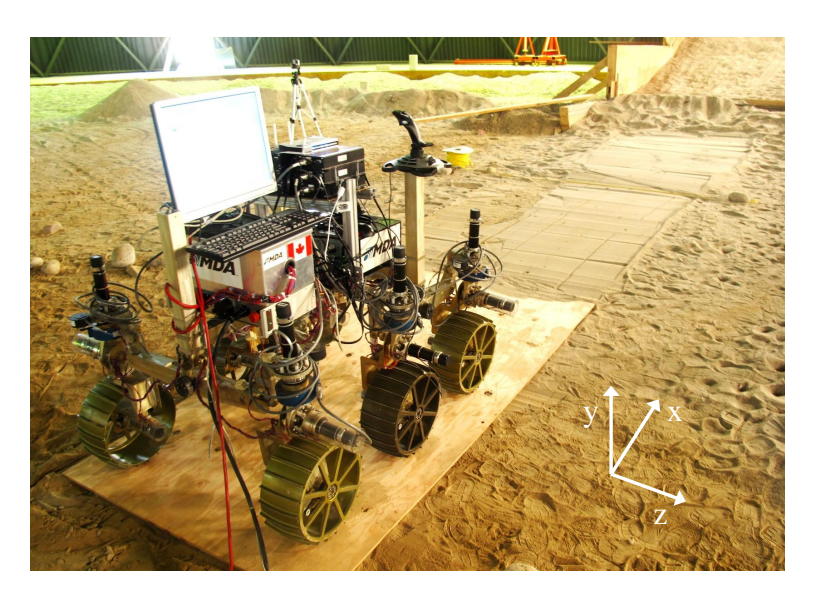


FIGURE 4.6. The RCP rover

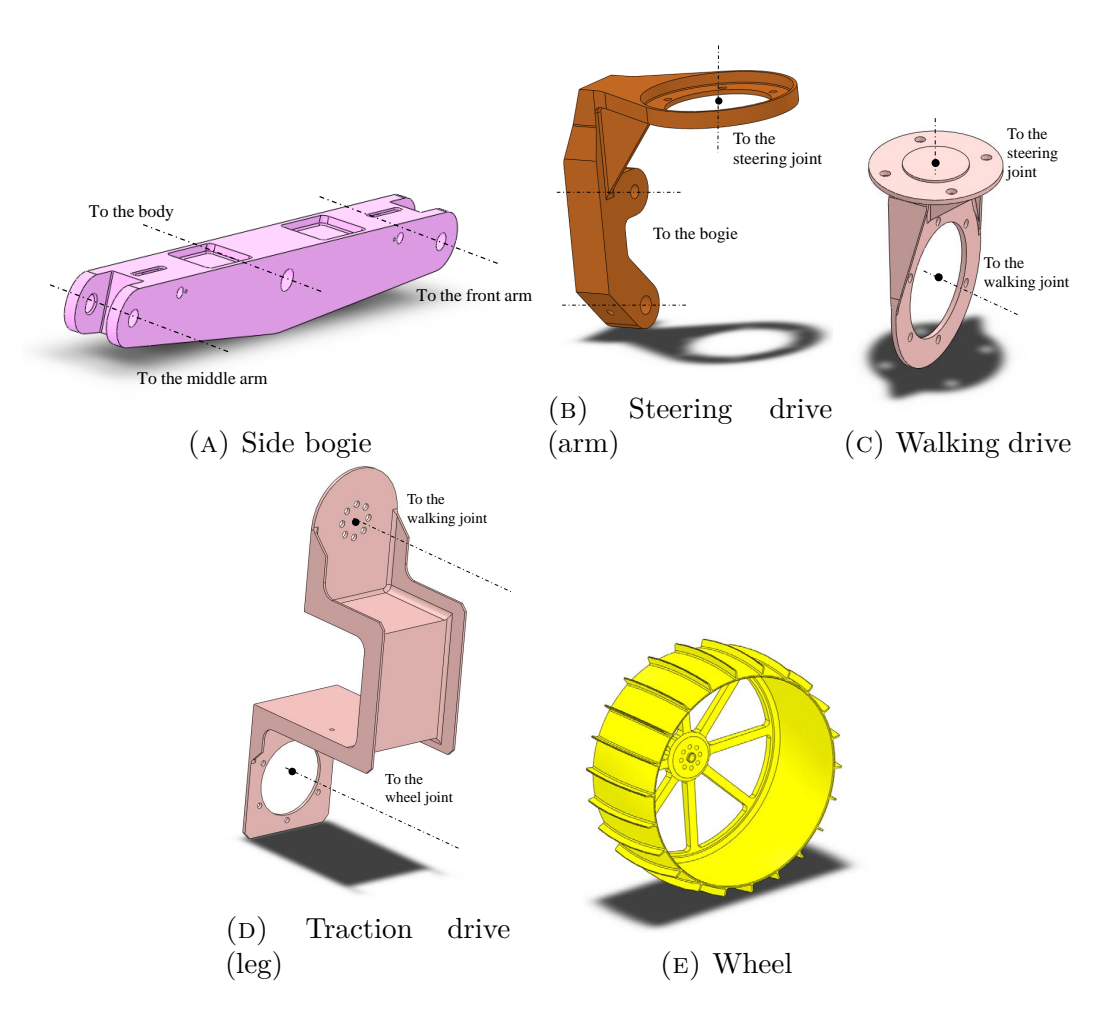


FIGURE 4.7. The chassis elements and the wheel of the RCP

The rover main body is attached to three bogies –starboard, port, and rear– via passive revolute joints, which enables free rotation of the bogies with respect to the body. The components of the RCP are shown in Figs. 4.7 and 4.8. The structure of the chassis is as follows: The rover main body is attached to three bogies (starboard, port, and rear) via unactuated revolute joints which enables free rotation of the bogies with respect to the body. Each bogie is connected rigidly to two steering drives (arms). The steering joint attaches each steering drive to a walking drive. The axis of the steering joint is along global y direction as shown in Fig. 4.6. Next,

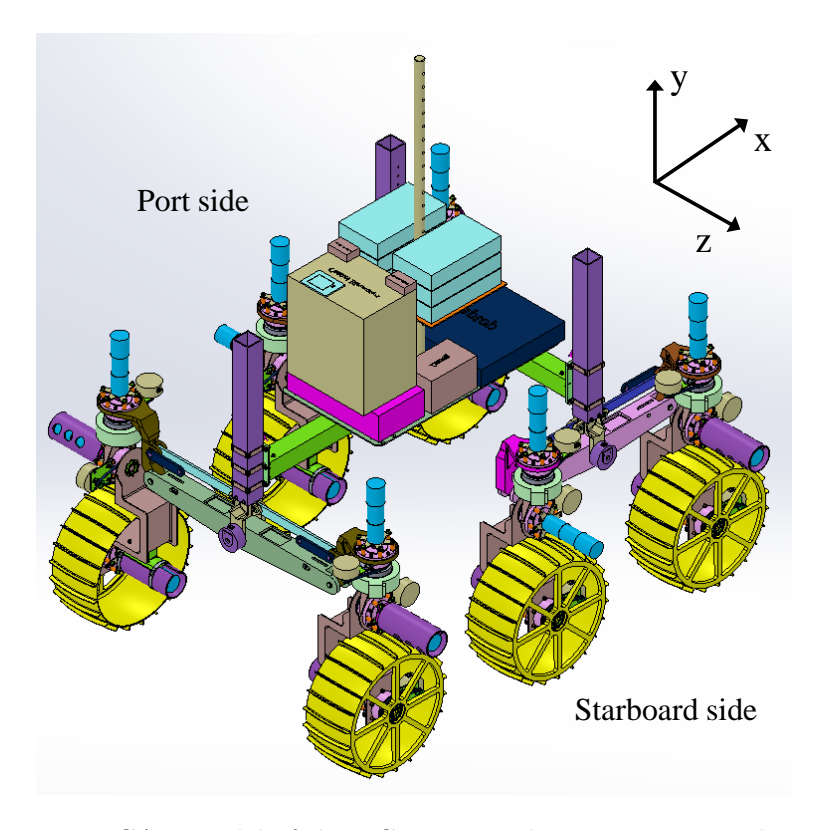


FIGURE 4.8. CAD model of the RCP was used to extract parts dimensions and joints positions to build the multibody model of the rover

each walking drive is connected to a traction drive (leg) via another revolute joint called the walking joint. This joint with its axis along global z enables the rover to operate under walking mode. In the current state of the rover the walking joints are locked and therefore, the walking mode is disabled. Finally, each leg is connected to a wheel via the wheel joint. Each wheel joint is actuated by a DC motor and the motors operate in velocity control mode.

During the operation the rover is controlled by a joystick. The direction and magnitude of the translational and angular velocities of the rover are specified by the operator via a joystick. An internal algorithm calculates the required wheel velocity and steering angle to meet the commanded motion. The RCP has several operation modes as shown in Fig. 4.9. The Ackerman steering mode was mainly used in the experiments.

The rover is approximately 1.4 m long and 1 m wide, with a total mass of nearly 125 kg. The wheels are metallic cylinders with grousers, of radius r = 0.175 m.

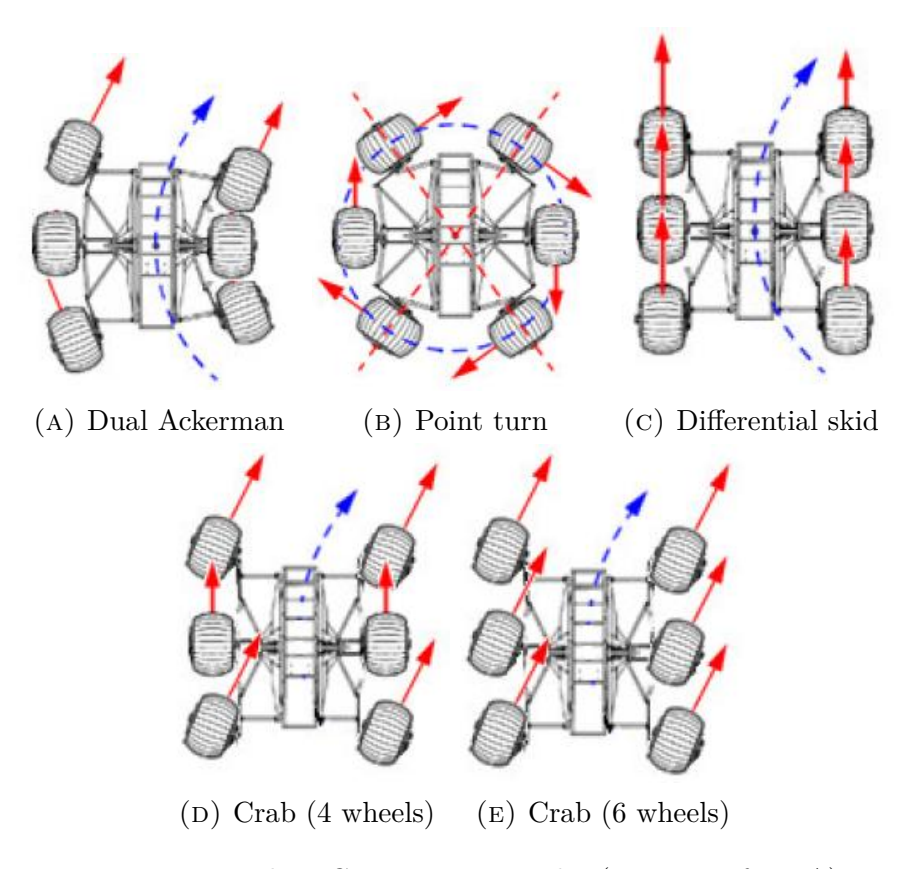


FIGURE 4.9. The RCP operation modes (courtesy of MDA)

A full-scale model of the rover (Fig. 4.10) was developed using the library introduced in Appendix B. The detailed information on the dimensions of each body and the location of joints was extracted from the CAD model of the rover provided by MDA (Fig. 4.8). The multibody model of the rover is composed of 28 rigid bodies connected by 27 revolute joints. The list of the bodies in the RCP model is the following: the main body, three bogies, six steering drives, six walking drives,

six traction drives, and six wheels. The motorized joints are modelled by adding the lock constraint over the revolute joints as described in Section B.4.2. The total number of the constraint equations including the lock constraint is 183. Although the name of the constraint can suggest that it does not allow the revolute joint to rotate, it actually does the opposite by imposing the input joint rate on the revolute joint. By adding the lock constraint the joint rate can be specified via a rheonomic kinematic constraint. Adding this constraint on the wheel joints and the steering joints makes them controllable at the velocity level. Therefore, it is possible to send angular velocity commands to the wheels to operate the rover and to steer the legs. The constraint forces and/or torques associated with the lock constraint represent the required action on the joint. Particularly, the constraint torques on the wheels of the rover give an estimation of the amount of torque required by the motors in the actual experiments.

The multibody library includes functions to evaluate the wheel-terrain interaction forces according to the terramechanics semi-empirical relations as described in Section 4.3. For the simulations performed in this study, an index-1 augmented Lagrangian formulation with projections of positions and velocities [117] was employed together with the Newmark integration formulas [118].

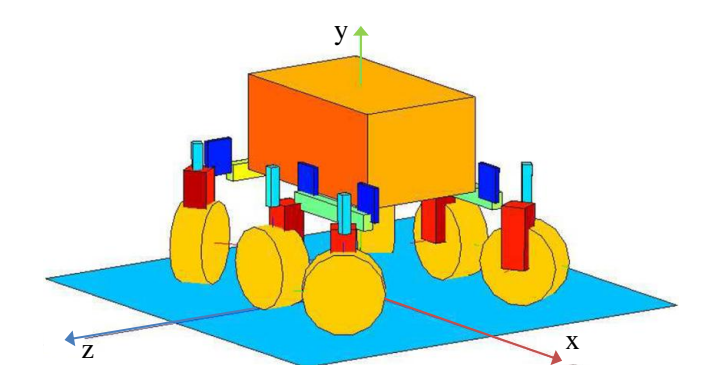


FIGURE 4.10. Illustration of the multibody model of the RCP

4.5.1 Effect of normal force distribution on wheel slip. The NFD introduced in Section 4.4 is intended to be used as a performance indicator of the mobility of a wheeled robot. According to the discussion in Section 4.4, of two different configurations of the same vehicle, the one with a more uniform normal load distribution will develop a lower slip to provide the same drawbar pull. The simulation results in this section support this statement.

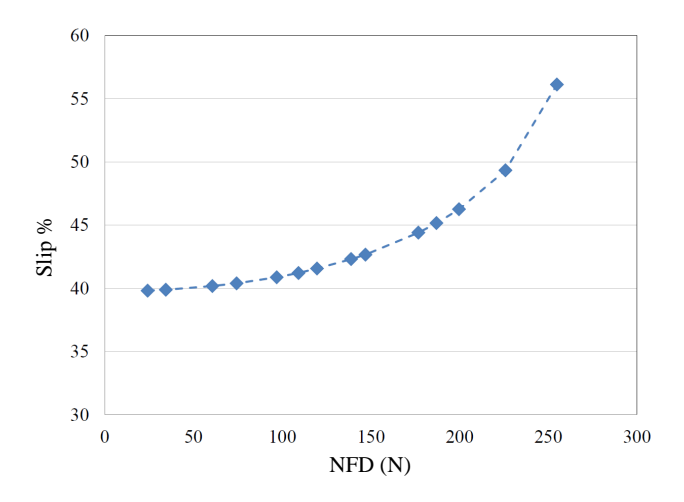


FIGURE 4.11. Values of the slip-vs.-NFD index developed by the RCP while climbing a 10° slope, with a 22.5 kg payload

First, the climbing manoeuvre of the RCP on a 10° slope with the properties of soil type "A" from Table 4.1 was simulated. The wheels of the rover were commanded to move with a constant angular speed $\omega = 0.4$ rad/s. In order to obtain different load distributions among the wheels of the RCP, a 22.5 kg (50 lb) payload was added as a movable mass element to the rover model. The simulation was repeated for different locations of the payload along the longitudinal axis of the vehicle. This resulted in variations of the position of the CoM of the rover, which in turn produced different values of NFD during the climbing manoeuvre.

In Fig. 4.11 the slip developed to climb a 10° slope while carrying a 22.5 kg payload is plotted for different values of NFD. The results confirms that lower values

of NFD resulted in less slip required to carry out the climbing, which is beneficial from the mobility and energy-consumption points of view. This study shows that it is possible to reduce the slip level by acting on the rover load distribution.

4.5.2 Effect of normal force distribution on drawbar pull. Alternatively, the improvement in mobility can be quantified by the value of the maximum slope that the vehicle can negotiate. The climbing manoeuvre was simulated for a variable slope with the properties of soil "A" from Table 4.1. The rover was considered unable to climb if the required slip ratio became higher than 90%. A similar slip threshold was used in slope climbing tests with the Dynamic Test Model of the Mars Exploration Rover [110]. The slope angle was increased until the rover was unable to complete the manoeuvre without exceeding the maximum admissible slip. Fig. 4.12 shows that a correlation exists between the value of NFD and the maximum slope the vehicle can successfully climb. Lower values of NFD improves the climbing ability of the rover.

Heavy normal loads and low values of the k_{ϕ} coefficient of the terrain were identified in Section 4.3.1 as the most influential factors on the F_D -vs.- F_n relation. Their effect on the slip developed by the RCP during a climbing manoeuvre is described in Section 4.10.

4.6 Description of the experiments

Results in section 4.5 showed the effect of repositioning the CoM on the normal force distribution, which in turn influences rover mobility. The rover ability to develop drawbar pull can be evaluated by slope climbing manoeuvres, as explained above. Drawbar pull tests can be considered analogous to slope negotiation tests since the application point of the applied force was chosen to be close to the rover

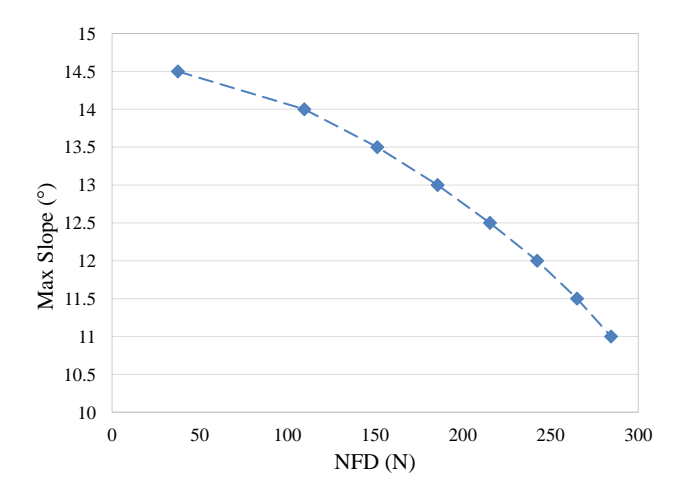


FIGURE 4.12. Correlation between the maximum slope angle that the RCP can climb (with a 90% slip) and the NFD

CoM, at least in the vertical direction. The action of gravity along the main longitudinal axis of the rover during slope climbing has similar effects to an external drawbar pull load applied on the chassis. That way, the ability of the rover to develop drawbar pull on flat terrain can be used as an indication of its ability to climb slopes. Drawbar pull experiments are also easier to carry out, as they require less resources than building a variable-angle, soft-soil slope.

A set of experiments, including drawbar-pull tests with variable NFD and wheel slip was carried out with the RCP on soft, sandy soil. The experiments were planned and conducted by several members of the Applied Dynamics Group of McGill University. The RCP was operated with the help from the personnel of the Robotics and Automation unit of MDA. The author of this thesis played a key, leading role in preparation, planning, and performing of the experiments. The test results reported in the following sections were obtained from three rounds of experiments, each lasting three days. These experiments took place in the Mars Dome which is a large, fully enclosed area, specially designed for mobile robots experimentations [119]. It is

located on the UTIAS (University of Toronto Institute for Aerospace studies) campus. The construction of the interior of the dome is aimed at producing unstructured environments. Large areas covered by sand made this facility suitable for testing the RCP mobility on soft soil. The objective of these experiments was to measure the drawbar pull developed by the rover for a certain wheel slip and load configuration. Initially, the tests were carried out in the setting shown in Fig. 4.13. The human operator would feed the rope to the figure 8 descender with a constant velocity to control the translational velocity of the rover. This configuration was later modified and a winch shown in Fig. 4.14, replaced the human operator, as schematically illustrated in Fig. 4.15. Details of the reasons for this modification are given in Section 4.6.2.

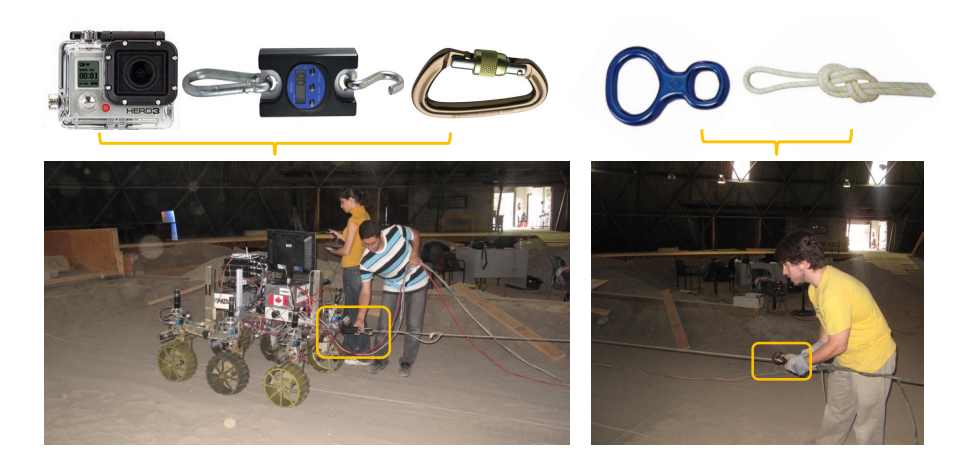


FIGURE 4.13. Drawbar pull test with the RCP

4.6.1 Slip ratio measurement. In experiments related to wheel-soil interaction the wheel slip plays an important role. The wheel slip is determined from angular velocity of the wheels and the rover translational velocity. The rover was operated under velocity control via commanding all the wheels to move with the maximum angular velocity of 0.4 rad/s. The RCP was equipped with wheel encoders



FIGURE 4.14. A winch was used to control the translational velocity of the rover

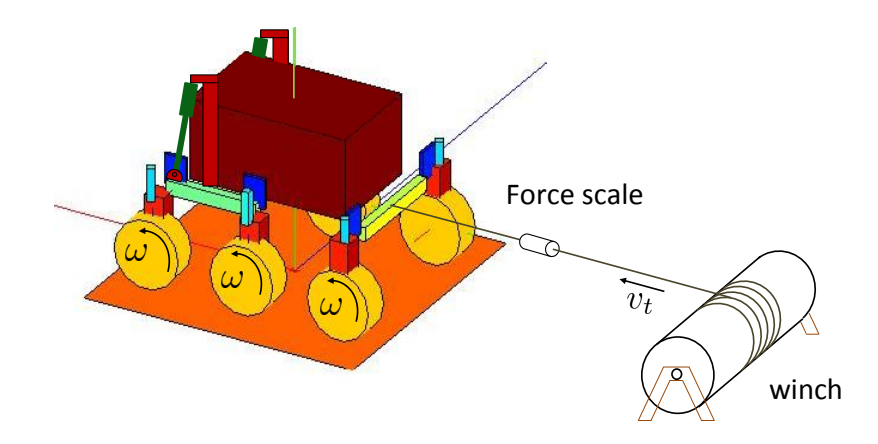


FIGURE 4.15. Drawbar pull tests were carried out using a winch to obtain a more uniform rover motion compared to the setting illustrated in Fig. 4.13

which measured the angular velocity of each wheel. Estimation of the translational velocity of the rover was more challenging. An Inertial Measuring Unit (IMU) was placed on the body of the RCP which measured the acceleration of the rover in three orthogonal directions. Generally, the acceleration readings from the IMU can be integrated over time to provide an estimation on the rover velocity. However, at low velocities the result from this method is highly affected by the drift in integration and does not provide the necessary precision. Therefore, to obtain the translational

velocity of the rover we resorted to visual references. For straight line motion this method can provide acceptable results with simple instrumentation. Instrumentation included a measuring tape, a GoPro camera and a pointer. The measuring tape was placed along the trajectory of the rover which was a straight line. The GoPro camera was chosen due to its easy mounting on different surfaces, stable video recordings, and its ability to record under harsh conditions. The camera was mounted under the RCP to face the measuring tape on the ground. The camera recorded the position of the rover for the duration of the experiment. The position of the rover at every 5 second was extracted to obtain its average translational velocity.

4.6.2 Force measurement. The terrain reactions, as well as forces applied to the body of the rover were measured for every experiment. The RCP is equipped with six force-torque sensors mounted on each of its legs. The normal, tangent, and lateral terrain reactions acting on each wheel were measured by these triaxial sensors during each experiment. However, generally for the purpose of online measurement of load distribution only normal force sensing is required. The difficulty in using these sensors was the need for their calibration before each test. The calibration of the readings in normal direction was carried out by means of placing digital scales under the wheels when the rover was stationary. Figure 4.16 shows a sample reading of the normal forces from the onboard sensors, after calibration.

In the longitudinal direction the forces were assumed to be zero when the rover is stationary. However, this assumption neglects the presence of prestress in the structure of the chassis. To reduce errors in estimation of the drawbar pull, additional sensor measurement in the longitudinal direction was required. To this end, a digital force scale was used to measure the force exerted by the winch on the rover. The time history of the force scale readings was recorded by a GoPro camera rigidly attached to it, as shown in Fig. 4.17.

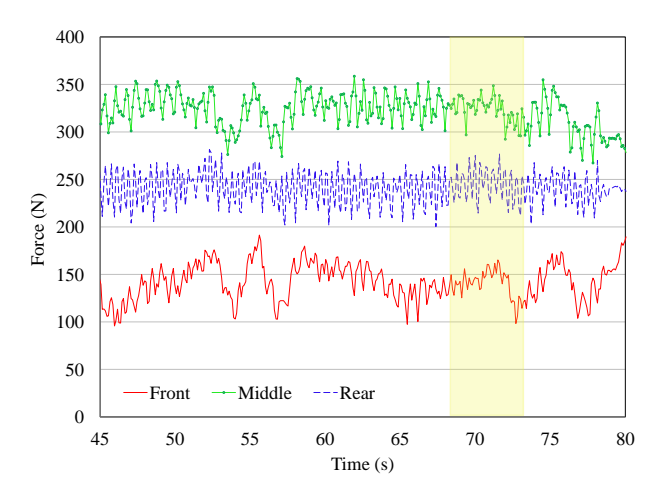


FIGURE 4.16. On-board force sensor readings in the normal direction at the front, middle, and rear starboard wheels



FIGURE 4.17. Snapshot of the recording of the GoPro camera which shows the screen of the force scale

As mentioned earlier first a human operator was used to apply force on the rover (Fig. 4.13). The results of that set of experiments showed large fluctuations in the force readings. Figure 4.18 shows one of the force plots from that set. Furthermore, the translational velocity of the rover was not constant under that setting which

resulted in variable slip during each test. This was the motivation for modification of the experimental setup. The RCP was connected to a winch to ensure that the rover translational velocity and consequently, wheel slip are constant during each test. In the latter setup, the translational velocity of the rover was controlled by specifying the winch rotary speed. Figure 4.19 illustrates the time history of the force applied to the rover by the winch, showing less fluctuation compared to Fig. 4.18. Given that the rover travels with negligible acceleration the force applied to the body must be balanced by the net tangential force developed at the wheels. The readings of the tangent terrain reactions from the six force-torque sensors were added up and compared to the readings of the digital scale, and showed a good agreement.

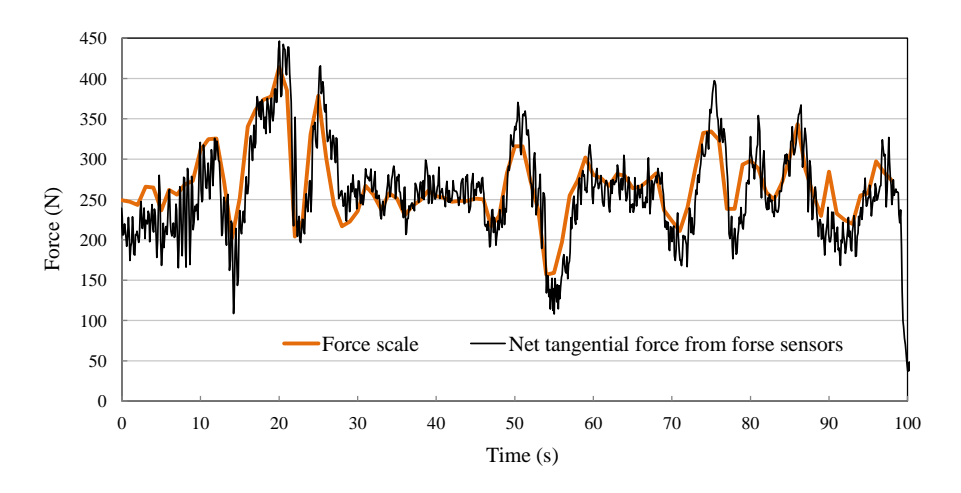


FIGURE 4.18. Force applied to the rover by the human operator

4.6.3 Modification of load distribution of the chassis. The NFD can be reduced significantly via design considerations, e.g., with a suitable distribution of the batteries and other heavy elements on the platform. Load distribution can also change during operation, e.g., by repositioning movable components of the rover such as manipulators.

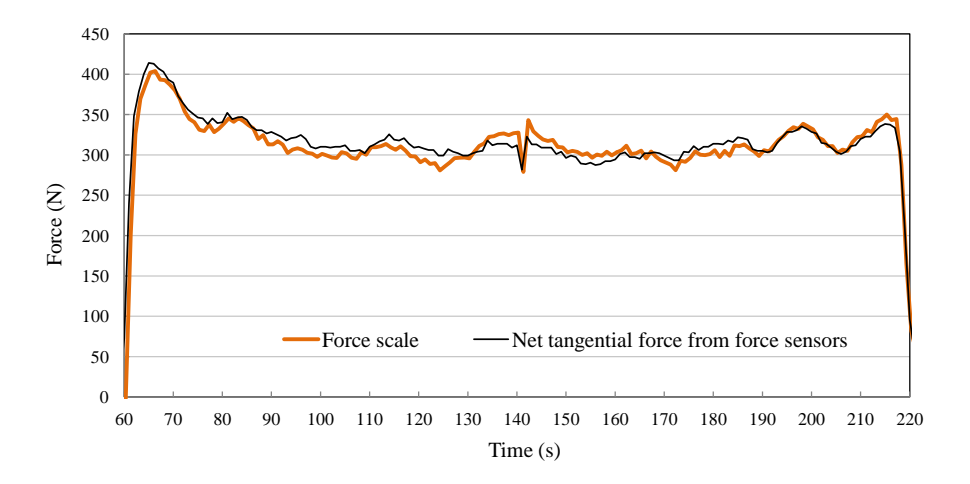


FIGURE 4.19. Force applied to the rover by the winch

To represent this with the RCP, and in order to obtain different sets of normal force distributions for each experiment, two movable 11.25 kg (25 lb) mass elements were mounted on the rover platform. Two attachment positions for the mass elements were designated on the rover body: the front attachment was the front tip of the main body and the rear attachment was the connection between the rear bogie and the main body. Three different configurations were achieved by distributing the mass elements between these two attachments. The mass-at-front configuration (Front_Config) corresponds to placing both mass elements at the front attachment. The mass-at-rear configuration (Rear_Config) refers to the one in which both mass elements were located at the rear attachment. The mass-in-the-middle configuration (Middle_Config) was obtained when one mass element was located at the front attachment and the other at the rear attachment.

In practice, with the RCP a uniform load distribution among the wheels cannot be achieved only via the relocation of the CoM due to limitations in the weight and the location of the extra mass elements. Furthermore, due to the presence of passive joints in the RCP suspension full control on the load distribution between the wheels is not possible. This is a feature commonly found in planetary exploration rovers. By repositioning the CoM of the rover only the load distribution between the rear wheels and the side bogies can be controlled. The load distribution between the front and middle wheels on the side bogies depends on the orientation of the bogie with respect to the rover body, which cannot be controlled because the body-bogie joint is passive. We will use the term redundant actuation to refer to the actuation introduced in these originally passive joints of the rover suspension. Besides modifying the normal force distribution among the vehicle wheels, redundant actuation can also be used to enhance certain manoeuvres like obstacle negotiation. Moreover, the actuation strategy can be modified during operation.

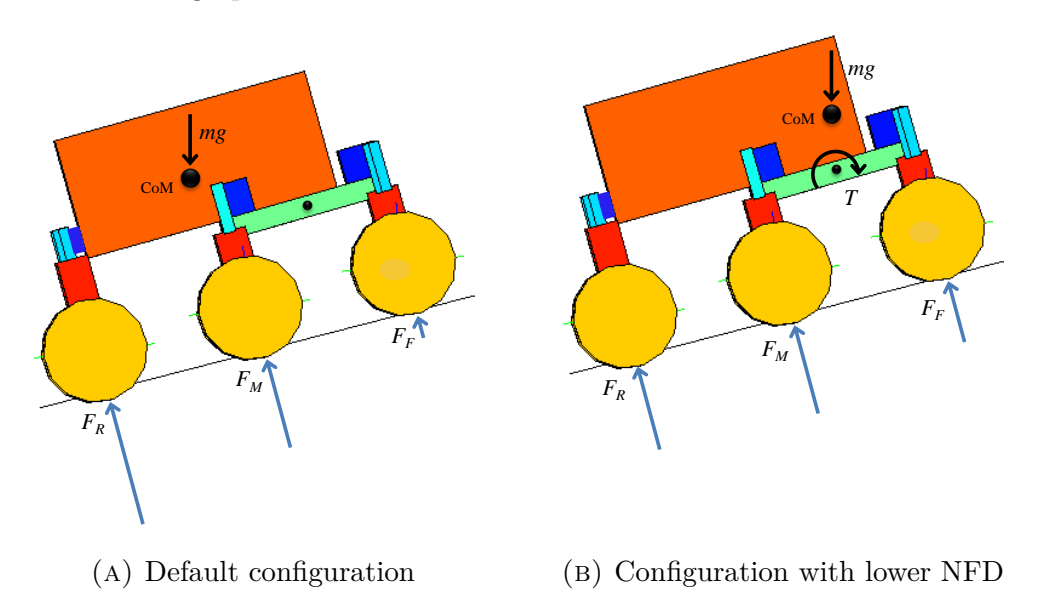


FIGURE 4.20. Effect of CoM repositioning and redundant actuation on normal force distribution

The effect of CoM repositioning and redundant actuation is illustrated with two configurations of the RCP in Fig. 4.20, where Fig. 4.20a represents the default configuration of the RCP. In Fig. 4.20b, the position of CoM is shifted towards the front of the rover and redundant actuation is introduced between each side bogie and the main body. In this example, a 60 Nm torque in the clock wise (cw) direction is applied at each bogie joint. In these figures the lengths of the arrows that represent the reactions at the wheel-terrain interface are proportional to the magnitudes of the normal forces obtained from simulation. In the default configuration in Fig. 4.20a, the resultant load distribution gives $\eta = 158.1$ N. The rover in this configuration is able to negotiate a maximum slope of 11°. As shown in Fig. 4.20b, a considerable reduction of NFD was achieved with the application of the described techniques. The NFD went down to $\eta = 24.2$ N and the rover was able to climb a 14.5° slope with the same slip as in the original configuration.

The simulation results reported in this section confirmed the effectiveness of the CoM repositioning and redundant actuation on the normal force distribution of the rover and its climbing ability. Next, the considerations for choosing and mounting an actuator to achieve redundant actuation for the RCP is discussed.

4.6.4 Considerations for redundant actuation. Redundant actuation in the case of the RCP controls the normal force distribution between the front and the middle wheels. This is achieved by mounting an actuator between the body and each bogie. In theory, either a rotary or a linear actuator can create the desired effect, i.e., generating a specified torque at the articulation between the body and the bogie. However, in choosing the actuator every precaution against limiting the motion of the rover has to be taken. When operating on irregular terrain, in order to maintain the contact between the ground and all the wheels the chassis has to be able to reconfigure. Presence of passive joints is necessary to make the reconfiguration possible. The joints between the bogies and the body are among the passive joints of the chassis. Actuating the bogie joints for the purpose of regulating the formal force

distribution must not interfere with other functionalities of the rover. To this end, the actuators must become passive when needed to allow the required reconfigurability.

In order to choose the type of the actuator the pros and cons of the rotary and the linear actuators were studied. The obvious choice for applying torque on the bogie was mounting a rotary motor on the revolute joint which connects the bogie to the body. The drawback of using a rotary motor was the considerable amount of works that would need to go towards disassembling the bogie from the body, mounting the motor, and assembling back the parts. The alternative option to generate the same effect was exerting force on the bogie at a distance from its articulation shared with the body. The force can be generated by a linear actuator which is connected between the body and the bogie. The linear actuator can be easily mounted on the rover without any alteration to the chassis components.

Due to the complications associated with mounting the rotary motors on the RCP the linear actuators were used to achieve redundant actuation. It must be noted that the choices made for instrumentation of the rover in this study are based on the design of the available rover prototype, i.e. the RCP. The implementation details to achieve redundant actuation would vary for different rover chassis designs.

Linear actuators come in different types such as: electric, pneumatic, and hydraulic. The hydraulic actuators are mainly suitable for heavy duty machinery where precision is not a priority. Also, these actuators have to be connected to a compressor during their operation. That introduces considerable complexity to the experimental setup which is not desirable.

Electrical actuators are common in robotic systems. However, these actuators mostly operate under position control and not force control. For the purpose of regulating the normal force distribution the force exerted by the actuator has to be controllable. Based on the experimental plan the actuator must be able to change the internal force distribution of the chassis without reconfiguring the mechanism.

Therefore, the actuator has to maintain certain amount of force for a period of time without introducing any displacement to the chassis components. For most electric actuators such operating condition results in current saturation as they are not designed for working under full mechanical load for a long period of time. Furthermore, most electrical motors are not back drivable. When the electric current to the actuator is cut they either become locked or show significant resistance in retraction. When operating on an irregular terrain, this makes it difficult for the rover to freely reconfigure and maintain all the wheels in contact with the ground. Therefore, the electrical actuators were not found suitable for the experimental setup used in this study.

Using pneumatic actuators, on the other hand, does not exhibit the issues related to the hydraulic and electrical actuators. The only drawback of using pneumatic linear actuators compared to their electric counterpart is the need for an external air source, i.e. air tank, while the electric actuators can use the rover electric power. However, components such as air tank, a regulator, and several valves can be easily added to the experimental setup without adding much complexity.

The most basic operation mode of pneumatic actuators is force control which is compatible with the requirements of the experiments in this study. The force can be controlled via a regulator by adjusting the pressure of the air that leaves the tank. These actuators can exert a constant force for a long period of time by maintaining the pressure level constant. The actuator force can be readily calculated by reading the pressure from the pressure gauge and finding the associated force from the calibration table. It is also possible to modify the actuator force in the course of each experiment to achieve variable NFD. Furthermore, pneumatic actuators can operate under atmospheric pressure by exhausting the residual air. In that case, they would act as a passive prismatic joint with negligible resistance which is desirable for chassis reconfiguration.

After evaluating the pros and cons of all different options, the pneumatic linear actuators were chosen to be mounted on the RCP. The disadvantage of linear actuators regardless of their type is that their stroke length can limit the rotation range of the bogie. Therefore, special attention must be paid to the size and attachment of the actuators to ensure that they are compatible with the entire motion range of the bogie, specially during obstacle climbing. The selection process and considerations for placement of the pneumatic actuators on the rover chassis is described next.

4.6.5 Selection and placement of pneumatic actuators. The required parameters for the selection of the pneumatic actuators are: (1) the actuator force and (2) the actuator size. In order to choose the actuator the force requirement has to be known. Actuators provide control on the normal force distribution among the wheels of the rover and assist in their obstacle climbing. The former has been discussed in detail in the previous sections. The latter is briefly studied here to find the maximum actuator force that is required to cover both applications. More details on the role of the actuators on obstacle climbing ability of the rover are given in Section 4.11.

Based on operation requirements set by the MDA design team, in planetary applications the rover has to be able to climb a 0.3-m-high step obstacle. This operation was simulated in the multibody dynamics library introduced in Appendix B. It will be shown in Section 4.11 that based on the simulation results the RCP would require smaller wheel actuation to overcome an obstacle with the aid of bogie actuation. Using the simulation tool the torque needed to enable the RCP to climb a 0.3-m-high step obstacle with wheels actuation of 24 Nm was computed. The results indicate that the required torque is about 30 Nm. In the simulation results presented in Section 4.6.3 the NFD in the RCP was reduced to 24.2 N with the aid of CoM repositioning and bogie actuation of 60 Nm. The above mentioned test

results provide an estimation of the torque requirement on the bogie joint for different operations of the RCP. Therefore, the actuator must be able to apply at least 60 Nm torque on the bogie. This value will be set as a design requirement for the selection of the actuator.

Next, the actuator force that can provide this required torque on the bogie has to be determined. In order to compute the force, the position of its point of application on the bogie must be known which depends on the placement of the actuator.

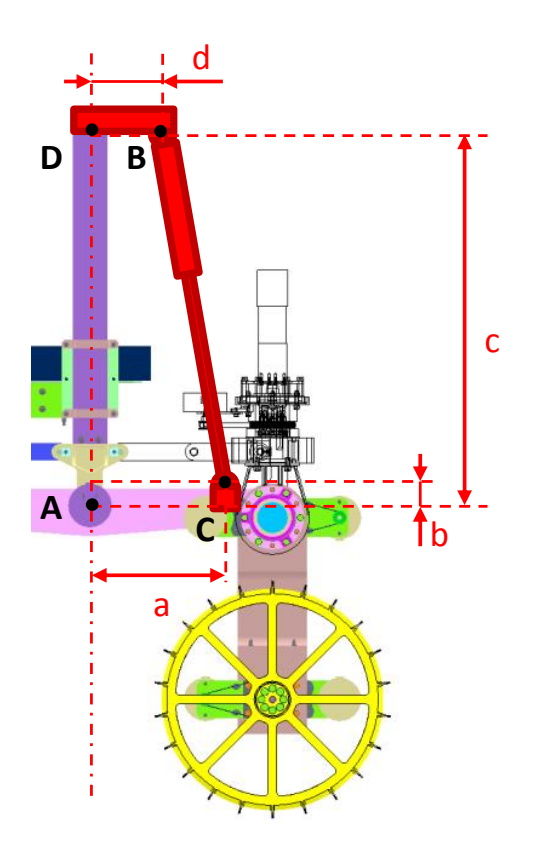
The second design parameter, the actuator size, also depends on the placement of the actuator on the rover. Therefore, first, the attachment position of the actuator on the rover body and bogic needs to be determined. The parameters associated with the actuator attachment position are a, b, c, and d as shown in Fig. 4.21a.

The attachment point C on the bogie must be at the furthest possible location from the bogie articulation point A, to maximize the resultant torque. Therefore, point C is chosen to be as close as possible to the joint between the bogie and the arm as shown in Fig. 4.21a. The horizontal and vertical distance of point C from A are parameterized by a and b, respectively, with their values listed in Table 4.2.

Table 4.2. Placement parameters of the pneumatic linear actuators on the chassis

| \overline{a} | b | c | \overline{d} |
|----------------|-------|-------|----------------|
| (m) | (m) | (m) | (m) |
| 0.189 | 0.070 | 0.450 | 0.106 |

The other factors which have to be considered in the selection of the actuator are its length and its stroke length. These greatly affect the rotation limit of the bogie with respect to the body.





- (A) Positioning parameters of the actuator on the chassis
- (B) RCP with the attached pneumatic actuator

FIGURE 4.21. Design modification of the RCP to add redundant actuation option

In order to fully define the attachment location of the actuator on the chassis, position of points B and D has be known. First, the feasible range for the horizontal distance between point B and D (parameter d) was studied. If point B is placed above point C (i.e. d=a), for small rotations of the bogie, the actuator would remain perpendicular to it and that would increase the resultant torque on the bogie. However, the same effect can be partially achieved by selecting a large value for parameter c (the vertical distance between point A and D). One drawback of selecting d=a is that the actuator would create a large moment about point D.

In that case, mechanical reinforcement of the horizontal bar between point B and D has to be considered. Furthermore, attaching the actuator with a large distance from point D increases the risk of reaching a singular configuration in large rotations of the bogie. Figure 4.22 shows the kinematic simulation of the bogie and actuator submechanism. When the bogie undergoes large rotations the sub-mechanism shown in Fig. 4.22a reaches a singular configuration. This problem is eliminated when d is much smaller than a as show in Fig. 4.22b. Therefore, in order to avoid the singularity problem and reducing the torque about point D variable d is set to 0.05 m, which is the minimum value considering the size of the actuator attachment. Also, the original columns on the rover chassis was replaced with a longer and stronger one made of Aluminium. This would allow for choosing a large value for parameter c, which is desirable as discussed above. The length of the column was chosen to be 0.45 m which was the maximum allowable value based the dimensions of the RCP chassis. The selected values for the attachment position parameters are listed in Table 4.2.

The step climbing manoeuvre was studied at this point to verify the suitability of the actuator attachment position. The simulation results of the climbing manoeuvre of the RCP over a 0.3-m-high step showed that with the selected parameters the climbing can be completed without encountering any singular configuration, as illustrated in Fig. 4.23. This shows that the attachment position of the actuators on the bogies and the body columns are acceptable. Based on that the required actuator size and stroke length were calculated. The simulation results show that when the rover climbs a 0.3-m obstacle the actuator length varies between 0.30 m to 0.39 m, as shown in Fig. 4.24. Therefore, the length of the actuator in its retracted configuration must not exceed 0.30 m and the stroke length must be at least 0.09 m.

A Switch Ready Aluminum Air Cylinder was chosen from McMaster-CARR catalogue (Fig. 4.25). This actuator was available in different bore sizes to provide a

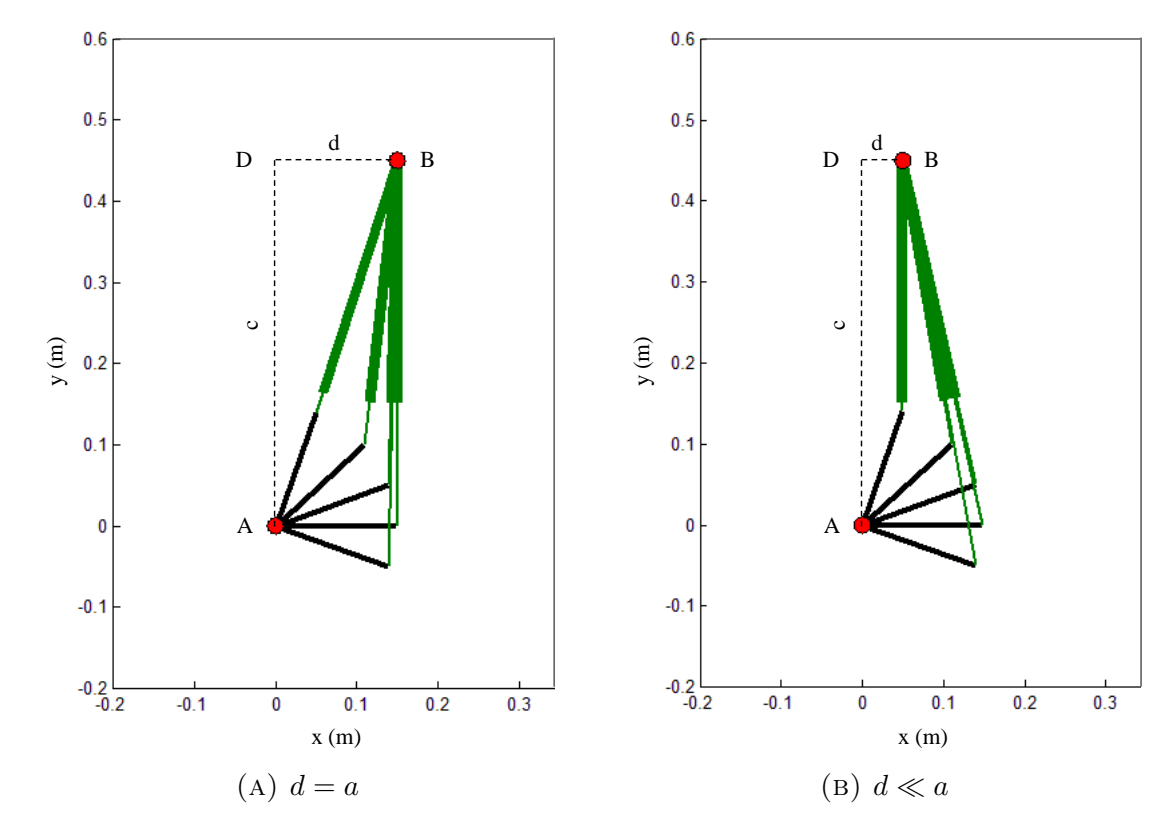


FIGURE 4.22. Kinematic simulation of the actuator and bogie submechanism to study mechanism singularity

wide range of force requirements. The actuator force in the data sheet was given for operation with 690 KPa (100 psi) pressure. The size and stroke length also varied with the bore size. Given the torque requirement and the attachment position of the actuator the required force was calculated to be 400 N. This guaranteed that at any point during different manoeuvres of the rover, including step climbing, the actuator is able to apply at least 60 Nm on the bogie. With this force level several actuator models satisfied the stroke length and actuator size requirements. Considering a reasonable safety factor the actuator with 38.1 mm $(1 \ 1/2")$ bore size was chosen. The specifications of this actuator is listed in Table 4.3. The stroke length was 0.152 m

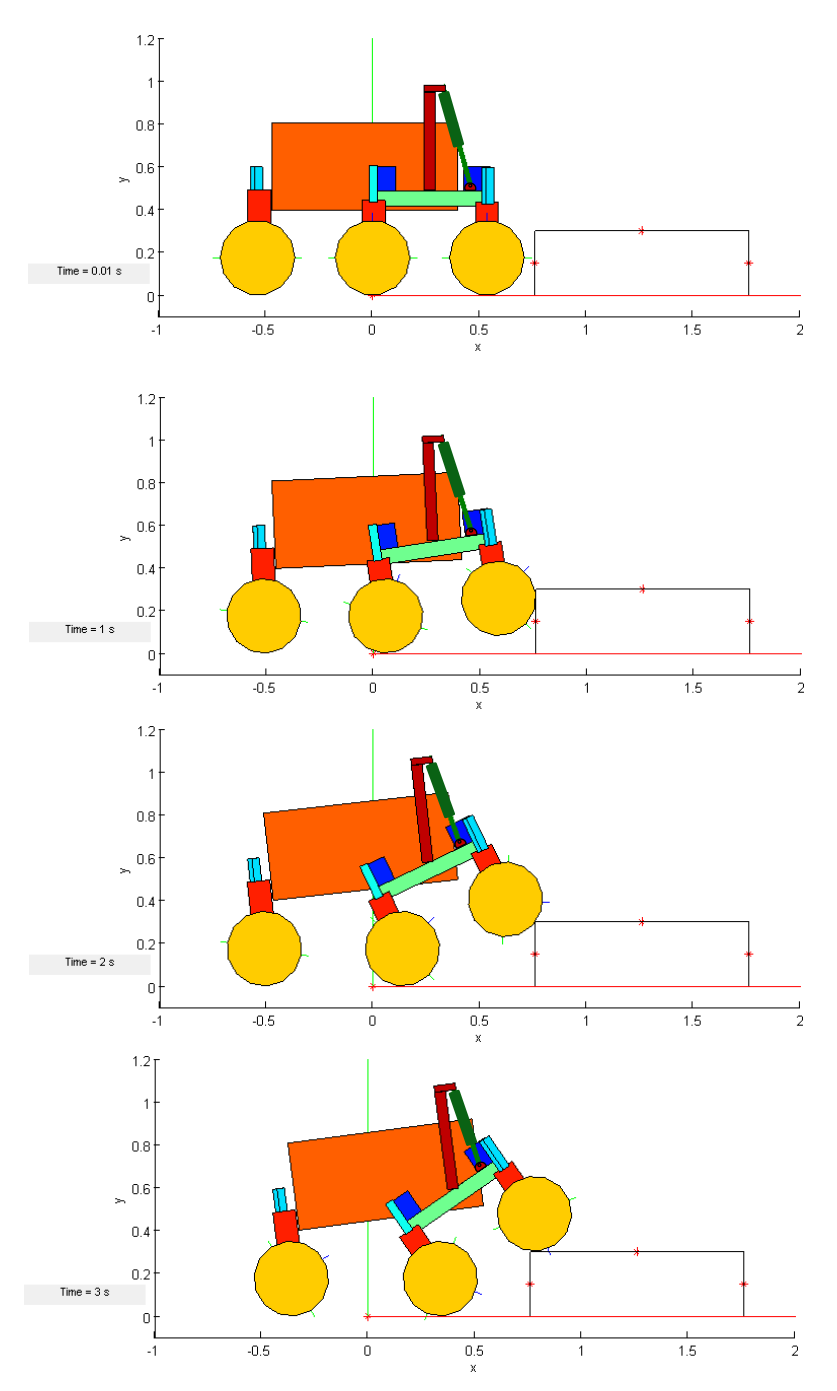


FIGURE 4.23. Snapshots from the simulation of the climbing manoeuver of the RCP on a 0.3-m-high step in the presence of the actuators

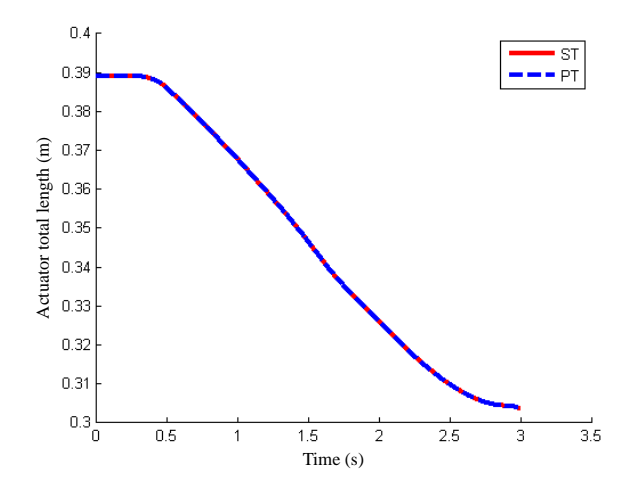


FIGURE 4.24. Length of the actuator during climbing a 0.3-m-high step

(6") which was compatible with the above design specifications. The climbing manoeuver of the RCP on the 0.3-m-high step was simulated with the selected actuator specifications and attachment position. The actuator force was set to 400 N for the entire motion. Simulation results shown in Fig. 4.26 confirmed that the minimum torque requirement of 60 Nm was maintained during the step climbing manoeuver.

Table 4.3. Specifications of the selected actuator from McMaster Carr catalogue

| Bore size (mm) | Force (N) | Min length (m) | Max length (m) |
|----------------|-----------|----------------|----------------|
| 38.1 | 729.5 | 0.274 | 0.425 |

The selected actuator was installed on the RCP with the attachment positions listed in Table 4.2. It will be experimentally shown in Section 4.8 that the actuator is able to provide the desired redundant actuation. Also, in experimental tests RCP was able to climb obstacles larger than 0.30 m and the presence of the actuators did not limit the motion range of the chassis components (Fig. 4.27).

4.7 Modification of the normal force distribution

In Sections 4.5.1 and 4.5.2 it was shown that the rover performance can be improved via modification of the normal force distribution. Design considerations would ensure an even normal force distribution for the default configuration of the rover on flat ground. However, manoeuvre of rovers on unstructured environments in presence of rough surfaces and obstacles results in the variation of normal force distribution during operation. Excessive sinkage and loss of mobility are some side effects of an uneven normal force distribution among the wheels. Therefore, to avoid such situations online modification of the normal force distribution is advantageous. Improvement of the mobility of the rover can be seen from two different points of view:

- Reduction of the slip ratio required to develop a certain drawbar pull. This applies to operations on flat ground, slopes with a constant angle, or when the rover carries a load.
- Improvement of the ability of the rover to develop higher drawbar pull for a certain slip ratio

The first scenario is more likely to happen as the slip is usually not specified, but rather developed; the slip increases until the wheel can provide the required drawbar pull for the required motion, although the DBP-slip relation is not linear and the drawbar pull can decrease beyond certain value of slip ratio. The first scenario is



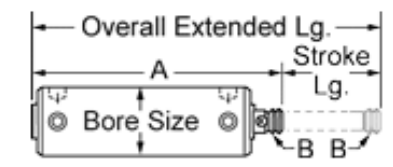




FIGURE 4.25. Switch Ready Aluminum Air Cylinder selected from McMaster-CARR catalogue

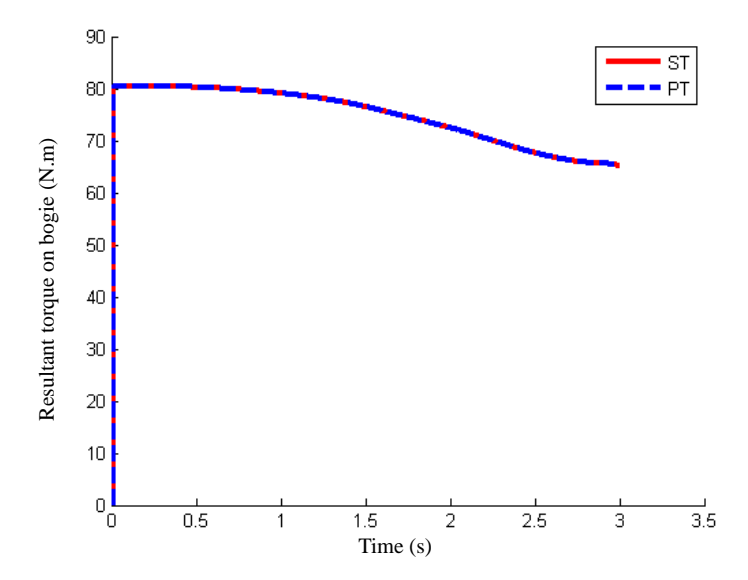


FIGURE 4.26. Time history of the torque applied by the pneumatic actuators on the bogies during the climbing manoeuvre of 0.3-m-high step. The actuator force was kept constant at $400~\mathrm{N}$

studied in this section using simulations. Experimental study of this type of operation requires very precise measurement of the rover velocity to monitor changes in the wheel slip. With the available resources obtaining reliable experimental results of this type was not possible. The second case is easier to realize experimentally and it allows one to carry out tests involving the continuous measurement of the drawbar pull. This was the approach adopted for the set of experimental tests which were performed with the RCP. The results of these experiments are reported in Section 4.8. Here the first case is studied in simulations with the model of the RCP and three slopes, listed in Table 4.4, which differ only in their frictional coefficients k_{ϕ} and ϕ , and their slope angles. When the rover climbs a slope with high frictional coefficients the slip developed to complete this manoeuvre is lower compared to the slip required to climb slopes with low frictional coefficients. It is desirable to assign a slope angle to each type of terrain so that the slip developed to climb that slope in absence of redundant actuation exceeds 80%. This can facilitate the comparison

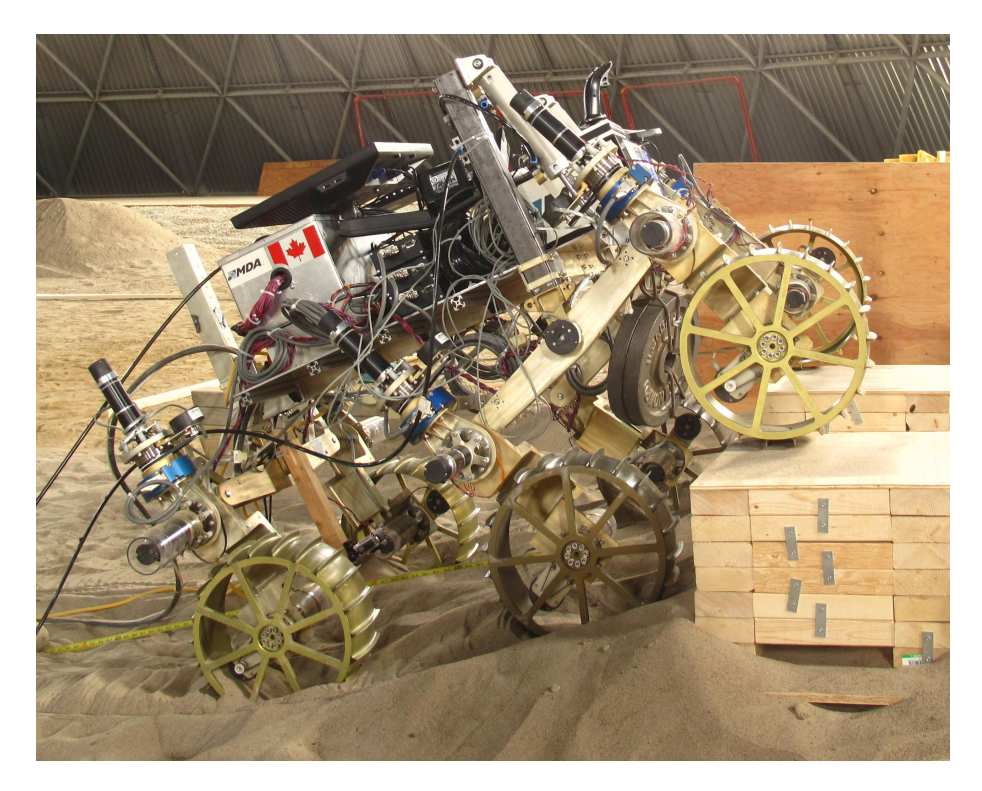


FIGURE 4.27. The RCP while climbing large obstacles with the aid of the actuators $\frac{1}{2}$

in the improvement of the rover performance between different cases. Therefore, the slope angle for the soils with higher frictional coefficient was set larger, as shown in Table 4.4.

Table 4.4. Properties of different slopes used in the simulations

| Case | Slope angle | k_{ϕ} | ϕ | n | c | k_c | K |
|------|-------------|----------------|--------|-----|-----------|---------------|-------|
| | (deg) | (kN/m^{n+2}) | (deg) | (-) | (N/m^2) | (N/m^{n+1}) | (m) |
| 1 | 9 | 820 | 33.1 | 1 | 220 | 1400 | 0.015 |
| 2 | 12 | 1410 | 34.1 | 1 | 220 | 1400 | 0.015 |
| 3 | 15 | 2000 | 36.1 | 1 | 220 | 1400 | 0.015 |

It was observed that during climbing, if no redundant actuation is applied, the middle wheels support most of the weight of the vehicle. The internal applied torque

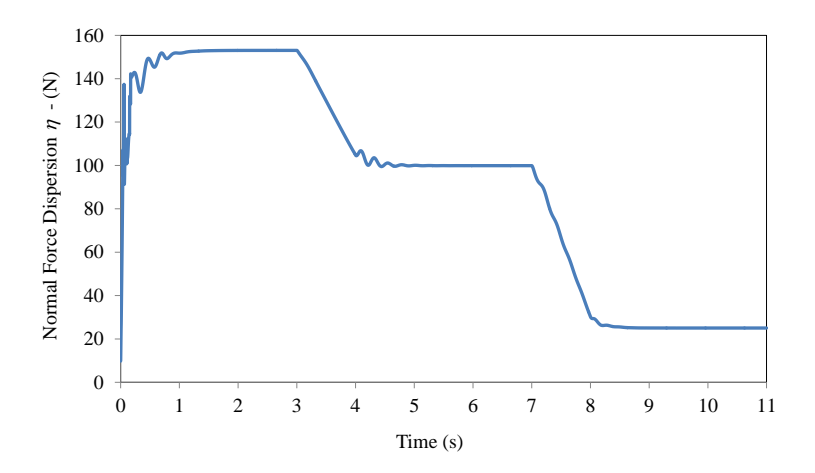


FIGURE 4.28. The NFD of the RCP during climbing of terrain 2 in Table 4.4. The internal actuation torque T was increased in two successive steps, from 0 Nm to 20 Nm and then to 50 Nm.

T on the bogies can then be used to generate a normal load transfer from the middle to the front wheels. The torque can be modified during the rover operation, based on the motion requirements. Details of the simulation of the RCP climbing slope 2 (Table 4.4) are presented next.

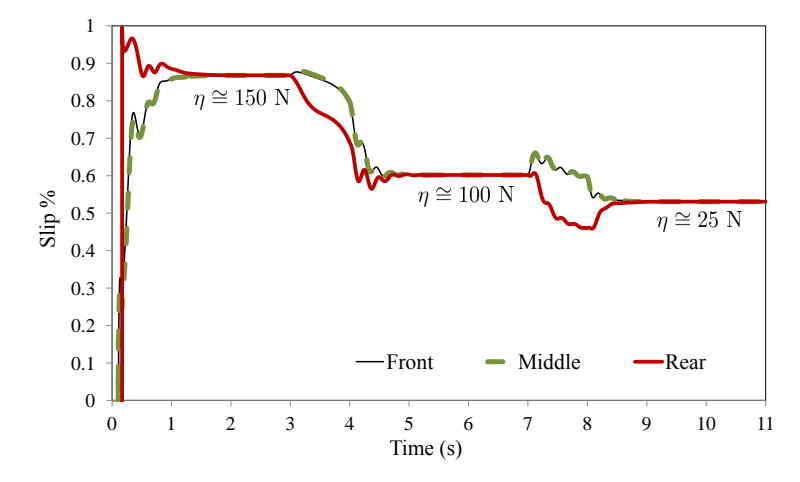


FIGURE 4.29. Slip of the front, middle and rear wheels of the RCP during climbing the terrain of case 2 in Table 4.4, for the manoeuvre in Fig. 4.28

At the beginning of the simulation the rover was placed on a 12° slope and the wheels where commanded to move with $\omega=0.4$ rad/s. Initially, in absence of redundant actuation, the NFD was $\eta=153$ N. The rover reached a steady-state motion after t=2 s, requiring 87% slip to move forward. At t=3 s, the torque on the bogic joint was increased gradually up to T=20 Nm. A new steady-state ensued after t=5 s. The new normal force distribution ($\eta=100$ N) brought the slip down to 60%. An additional increase in T to 50 Nm further improved the load distribution, enabling the rover to climb the same slope with 53% slip. These results are displayed in Figs. 4.28 and 4.29.

TABLE 4.5. Effect of internal actuation on the slope climbing ability of the RCP for the cases described in Table 4.4

| | Part 1 | | Part 2 | | | Part 3 | | | |
|------|--------|-----|--------|------|-----|--------|------|------|------|
| | T | NFD | slip | T | NFD | slip | T | NFD | slip |
| Case | (Nm) | (N) | % | (Nm) | (N) | % | (Nm) | (N) | % |
| 1 | 0 | 150 | 89 | 20 | 98 | 53 | 50 | 22.4 | 42 |
| 2 | 0 | 153 | 87 | 20 | 100 | 60 | 50 | 25.0 | 53 |
| 3 | 0 | 158 | 84 | 20 | 105 | 67 | 50 | 24.4 | 60 |

Similar tests were conducted for every case described in Table 4.4. The effect of two different values of T on the wheel slip and the NFD, is summarized in Table 4.5. The system behaviour followed the same pattern shown in Figs. 4.28 and 4.29.

4.8 Experimental results

The simulation results obtained in the previous section were confirmed with experiments. Improvement of the rover performance is studied here from the point of view of increasing the drawbar pull for a given slip ratio. First, the effect of the aforementioned factors on the normal force distribution of the RCP is reported. Next, the resultant performance improvement due to reduction in the NFD is presented.

4.8.1 Effect of reconfiguration on normal forces. In the simulation studies the performance of the rover was measured by its ability to climb slopes. Drawbar pull tests can be considered analogous to slope negotiation tests, since the external loads on the rover are of a similar nature. Drawbar pull experiments are also easier to carry out, because applying a variable external force to the rover requires less resources than building a large sand box with variable slope angle.

A set of experiments, including drawbar-pull tests with variable load distribution was carried out on the soft, sandy soil of the Mars Dome with the experimental setup described in Section 3.5 and a fixed slip ratio. The angular velocity of the wheels was set to $\omega = 0.4$ rad/s and its translational velocity was set to 0.027 m/s, which resulted in a wheel slip close to 60%. The load distribution was modified via CoM repositioning and redundant actuation of the rover chassis.

Figures 4.30 and 4.31 show the readings from the force sensors in four different tests. These readings are from the starboard side of the RCP during the motion of the rover on a straight line. Figure 4.30a corresponds to the RCP Rear_Config (defined in Section 4.6.3), in which the rear wheels support most of the load. The load distribution with this configuration is remarkably uneven with $\eta=139$ N. A second configuration, corresponding to Front_Config was obtained by shifting the mass elements towards the front. The normal forces obtained in this case which result in $\eta=113$ N are displayed in Fig. 4.30b. The comparison of Figs. 4.30a and 4.30b shows that CoM repositioning reduced the load on the rear wheels significantly, transferring it to the side bogies, where the middle wheels supported most of the load.

Next, a 9 Nm torque was applied between the main body and each side bogie. The resulting time history of the normal forces is shown in Fig. 4.31a which is associated with $\eta = 97$ N. The applied torque on the bogies was relatively small and did not transfer a significant load to the front wheels, but from the middle wheels to the rear wheels. Finally, the redundant internal actuation torque was increased

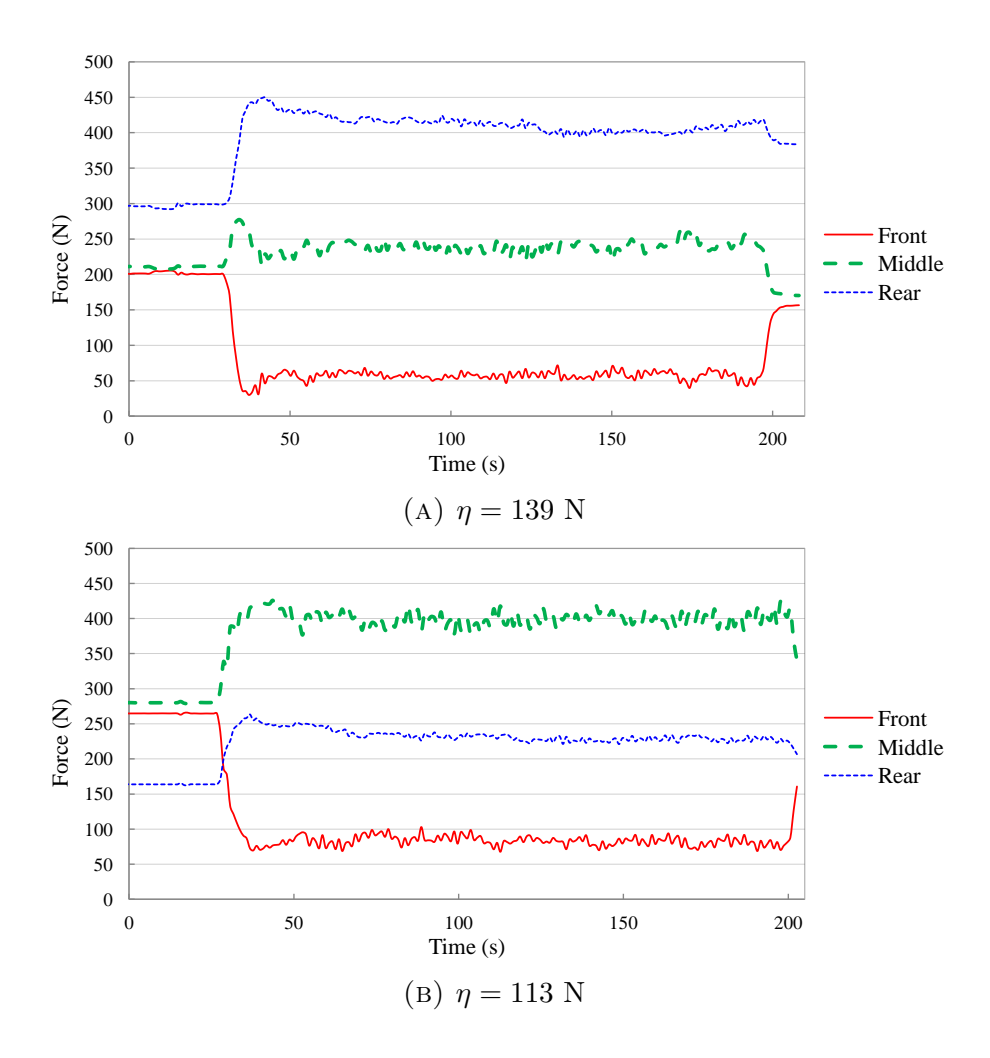


FIGURE 4.30. Experimental results: Normal force on the starboard wheels of the RCP with $\eta=139$ N and $\eta=113$ N

again up to 25 Nm and a higher load from the middle wheels was transferred to the front and the rear wheels, as shown in Fig. 4.31b. The NFD was reduced to $\eta = 69$ N. The comparison of these four experiments confirmed the effectiveness of CoM repositioning and redundant internal actuation in achieving the desired load distribution among the rover wheels.

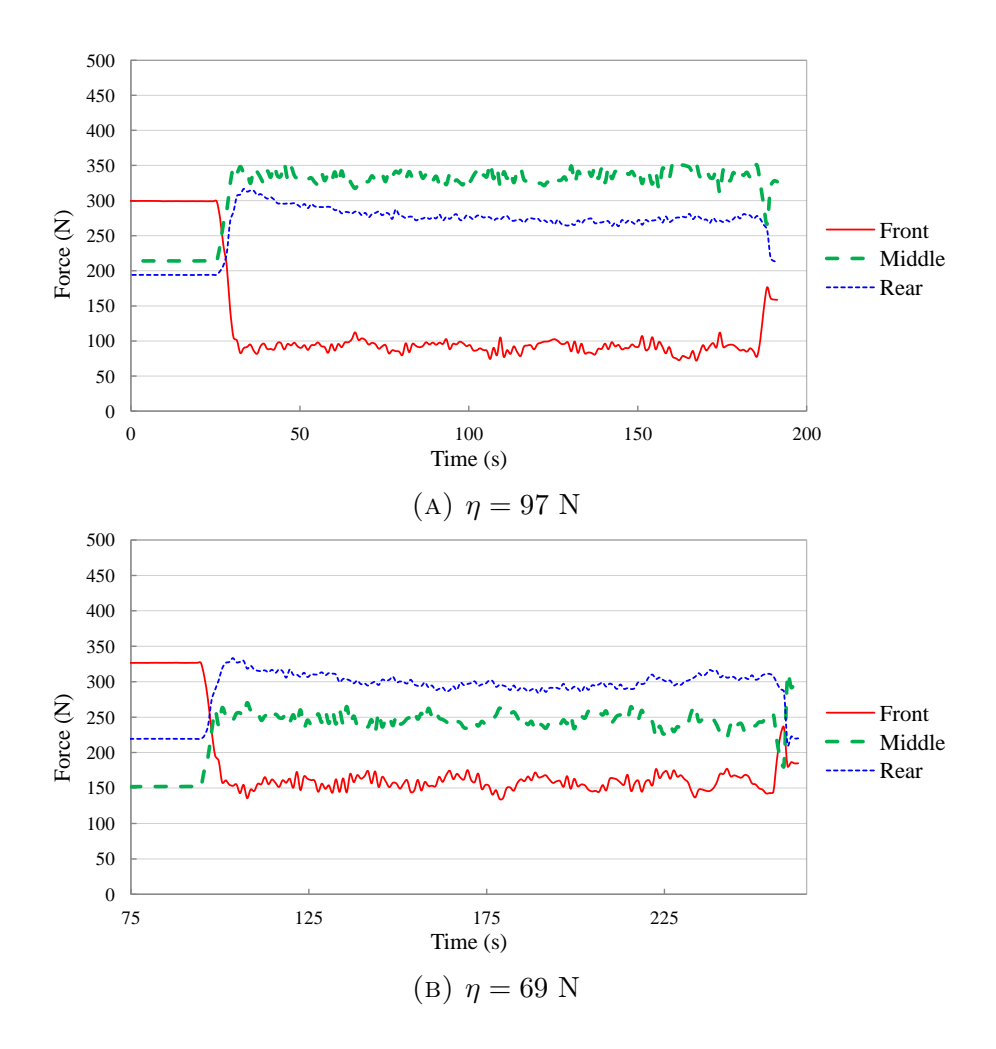
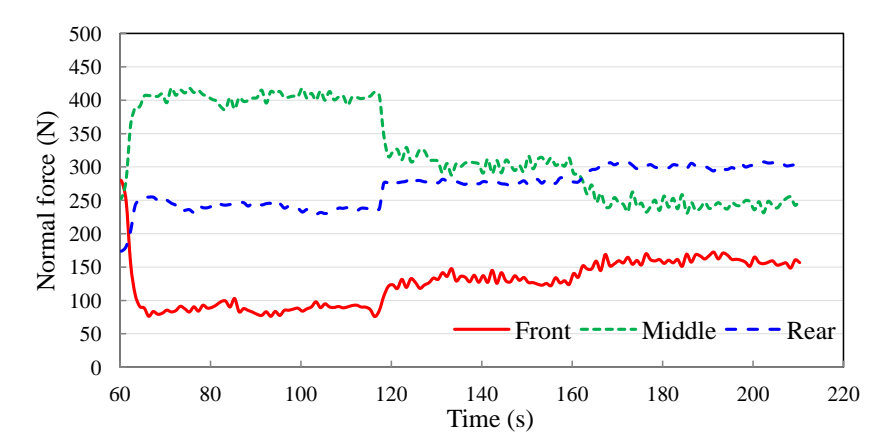


FIGURE 4.31. Experimental results: Normal force on the starboard wheels of the RCP with $\eta=97$ N and $\eta=69$ N

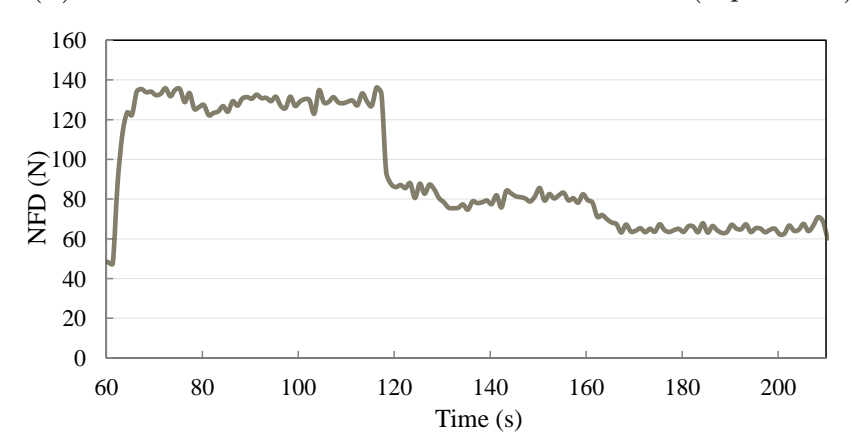
In another set of experiments the load distribution was modified online during each test. In these experiments the RCP traveled on a straight line on soft, sandy soil. The rover started its motion with the additional mass elements attached to the front of the rover and no redundant actuation applied to the bogies. The position of the mass elements was not changed during the manoeuvre. The angular and translational velocities of the rover were the same as in the previous experiments. The normal

force readings from the starboard sensors are shown in Fig. 4.32a. The results show that in the first part of the motion which corresponds to the Front_Config without redundant actuation, the load was distributed unevenly, with the middle wheel carrying most of the load. The second part of the motion started at t=120 s where 16 Nm moment about the bogie joints was introduced via the pneumatic actuators. Although the rover configuration remained at Front_Config, this modification resulted in reduction of the load on the middle wheels by transferring it to the rear and front wheels. To magnify this effect the actuation was increased to 32 Nm at t=160 s. As expected, this modification further balanced the load distribution among the wheels. In the experiments, the magnitude of the moment that the pneumatic actuators introduced on the bogie joint was calculated from the multiplication of the actuator force applied on the bogie and the distance from the application point to the bogie joint.

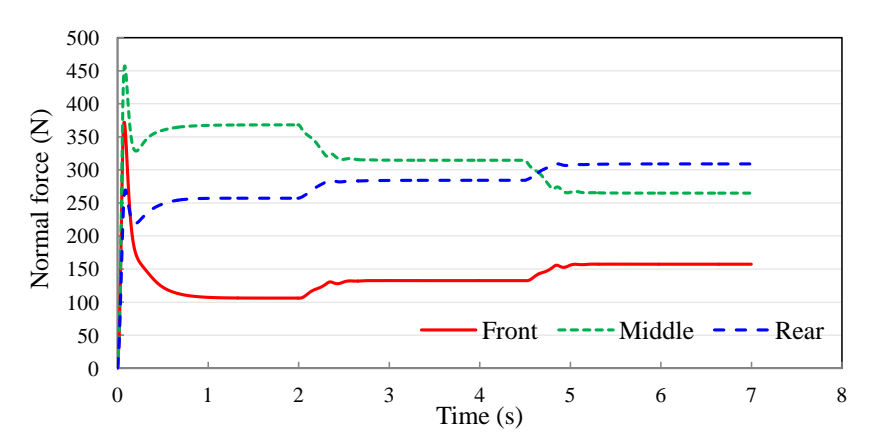
Fig. 4.32b shows the NFD of the RCP during the test. The results show that redundant actuation alone without CoM repositioning was able to reduce NFD significantly. Online adjustment of the redundant actuation is specially useful for rover manoeuvres on terrains with variable slope angles. Data from force sensors can be used internally during the rover operation to calculate the required redundant actuation to obtain the desired load distribution among the wheels. The same scenario was simulated with the multibody library for a shorter period of time. The time history of the normal forces in Fig. 4.32c shows that the simulation with the multibody model captured the effect of actuation on the force distribution.



(A) Effect of redundant actuation on normal forces (experiment)



(B) Resultant NFD based on experiment



(C) Effect of redundant actuation on normal forces (simulation)

FIGURE 4.32. Effect of redundant actuation on the NFD

4.8.2 Effect of reconfiguration on drawbar pull. In the previous section it was experimentally shown that the CoM repositioning and redundant actuation have a significant effect on the normal force distribution. The final objective, however, is the improvement of the rover mobility. The ability of the rover to develop drawbar pull plays the key role in this. To this end, a similar set of experiments was conducted to study the way drawbar pull changes with variation of NFD. In these experiments NFD was modified by means of a combination of repositioning of CoM and redundant actuation. The time history of drawbar pull during these tests is illustrated in Fig. 4.33.

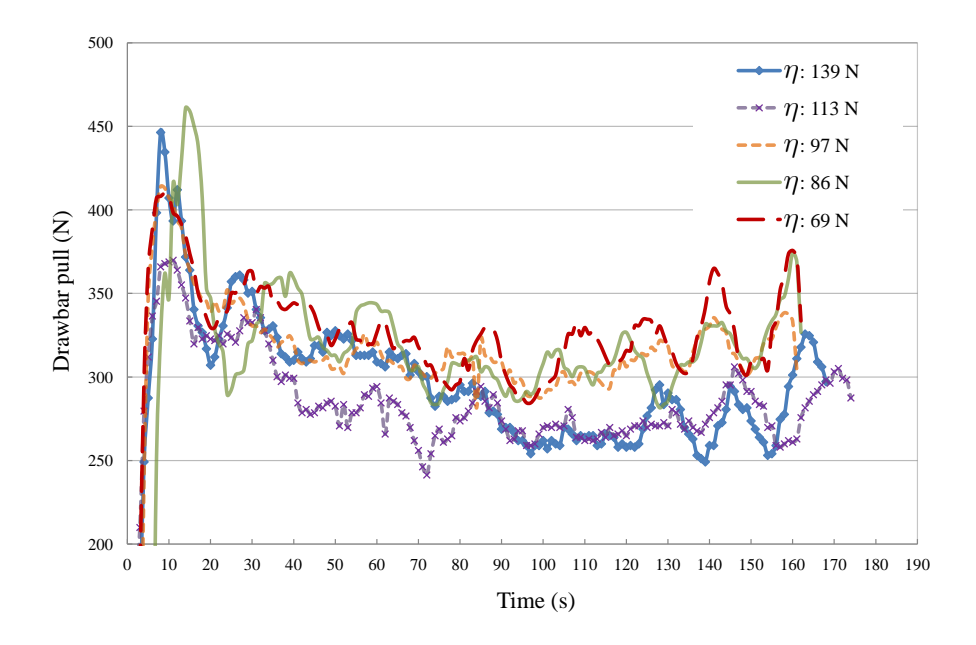


FIGURE 4.33. Drawbar pull during experiments with 60% slip and several NFD values

For a constant ratio of 60% slip, the configurations with lower NFD provided more drawbar pull than the ones with higher NFD. It can be shown based on the results of Section 4.3.1 that the relation between the NFD and the drawbar pull is also non-linear. The average value of the drawbar pull for each test along with the

Table 4.6. Experimental results of drawbar pull for different values of the NFD (averaged for each test)

| Case | 1 | 2 | 3 | 4 | 5 | 6 | 7 |
|------------|-------|-------|-------|-------|-------|-------|-------|
| η (N) | 69.0 | 82.3 | 85.9 | 97.3 | 111.3 | 113.2 | 139.4 |
| F_D (N) | 322.9 | 313.9 | 307.9 | 306.8 | 281.8 | 272.6 | 268.2 |

value of NFD corresponding to the rover configuration in that test are tabulated in Table 4.6. Only readings from the steady-state period of the motion were considered for this.

4.9 Comparison of experimental and simulation results

Among the experiments reported in the previous section four cases were selected for simulation. Parameters of soil "A" from Table 4.1 were used in the simulation. The same angular and translational velocity specifications used in the experiments were chosen as simulation inputs. Table 4.7 includes details of the configuration and redundant actuation in the selected tests. The translational velocity of the rover was specified via a rheonomic constraint on the translational motion of the body, as explained in Section B.4.2. This is similar to the role of a winch. The constraint force associated with this constraint is equivalent to the drawbar pull of the rover. Figure 4.34 shows the drawbar pull time history obtained from experimental and simulation tests.

Experiments 1 and 2 only differed in the position of the two mass elements which resulted in a more uniform load distribution in the latter. As described in Section 4.6.3, each of these elements has the mass of 11.25 kg. Both experiment and simulation results confirmed that in Experiment 2, which has a lower value of NFD, the developed drawbar pull is higher. In Experiment 3 the position of the CoM was the same as in Experiment 2. However, after the initial period of the

| Experiment | Mass element | Bogie actuation | NFD (η) |
|------------|--------------|-----------------|--------------|
| No. | position | (Nm) | (N) |
| 1 | Rear | 0 | 141 |
| 2 | Front | 0 | 125 |
| 3 | Front | 9 | 70 |
| 4 | Front | 32 | 63 |

Table 4.7. Operation conditions of the tests

manoeuvre the pneumatic actuators exerted a 9 Nm torque on each bogie, reducing the NFD for the rest of the motion. During this phase of the motion the drawbar pull showed an increase in both simulation and experiment. In Experiment 4 the actuation was increased in two steps during the motion: first, to 16 Nm and then to 32 Nm. After each increase in the value of the redundant actuation the rover reached a more uniform load distribution among the wheels, leading to its improved ability in developing drawbar pull. Therefore, both experimental and simulation results showed that for a given slip ratio it was possible to improve the ability of the rover to generate higher drawbar pull via decreasing the NFD.

The simulation results capture the same trends that can be appreciated in the experiments. Comparing the plots, differences can be seen in the mean value of drawbar pull during the rover steady state motion between simulation and experimental results. These difference can be explained by simplifications introduced in the terramechanics relations, and also the uncertainty and variability of the terrain parameters.

4.10 Effect of soil parameters on F_D -vs.-NFD relation

The relation between the rover ability to develop drawbar pull and the NFD varies with the type of soil. The effect of modifying the NFD on development of drawbar pull is more significant on some types of soil.

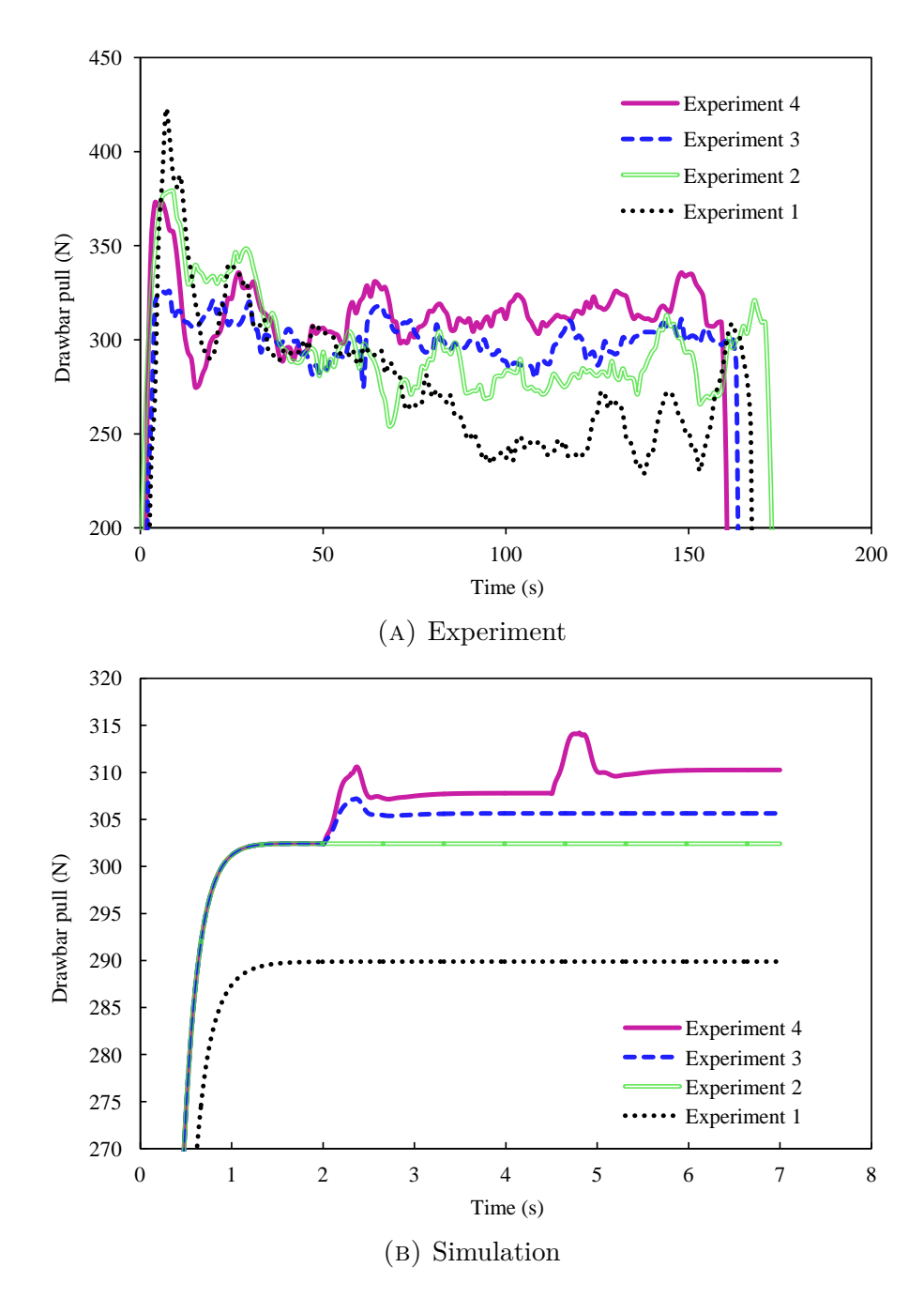


FIGURE 4.34. Experimental (a) and simulation (b) results from the drawbar pull experiments

The frictional component of the pressure-sinkage modulus k_{ϕ} , was found to be the most influential parameter in this regard. As discussed in Section 4.3.1, higher values of k_{ϕ} cause the F_D -vs.- F_n plot to be closer to a straight line. In the following section this study is taken to a higher level and the effect of k_{ϕ} on the relation between the climbing ability of the rover and the NFD is discussed.

4.10.1 Effect of the pressure - sinkage parameter k_{ϕ} . In order to study the effect of k_{ϕ} on the slope climbing ability of the rover, a new set of simulations was conducted on the model of the RCP. The climbing manoeuvre of a slope with constant velocity was simulated. Three different slopes described in Table 4.8 were used. Other terrain properties were the same as in Table 4.1. The slope angle for each case was selected so that the slip developed by the RCP with a uniform normal force distribution was the same in all cases studied, to make them comparable.

Table 4.8. Slope characteristics for the simulation of the climbing manoeuvre of the RCP

| Slope | $k_{\phi} (\mathrm{kN/m}^{n+2})$ | Angle (deg) |
|-------|-----------------------------------|-------------|
| 1 | 2000 | 10.0 |
| 2 | 1410 | 9.3 |
| 3 | 820 | 8.7 |

Results are presented in Fig. 4.35. For small values of NFD, $\eta < 100$ N, the slip remained near 40% in the three cases. However, for the terrain with the lowest k_{ϕ} (slope 3) the rover was not able to develop enough drawbar pull for $\eta > 100$ N, which resulted in the slip ratio rising up to 90%. A similar response was observed on slope 2 for $\eta > 225$ N, while on slope 1 the slip did not exceed 60%. These results suggest that the rover ability to climb a slope is more sensitive to load distribution on terrain with smaller values of k_{ϕ} .

4.10.2 Effect of larger normal loads. Apart from the soil, vehicle weight also can influence on the role of the NFD in improving the rover mobility. Based on

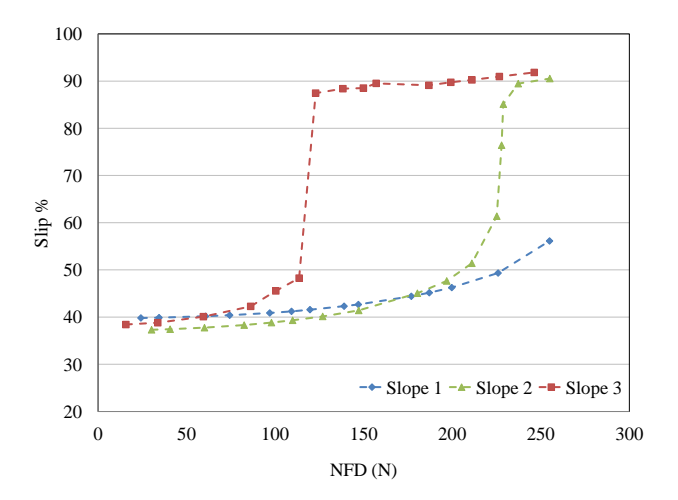


FIGURE 4.35. Slip-vs.-NFD plots for different slopes described in Table 4.8, with a 22.5 kg payload on the RCP

simulation studies, reducing the NFD has a more significant impact on the performance of heavier rovers.

According to Fig. 4.3 regardless of the slip ratio, large normal forces accentuate the nonlinearity of the F_D -vs.- F_n plot, displacing the operation point of the vehicle towards the right side of the F_D -vs.- F_n plot depicted in Fig. 4.5. When the rover operates in this region, making the normal force distribution more uniform will improve the mobility of the vehicle more significantly.

To study the effect of larger loads, two simulation sets with two different values of the extra weight added to the rover chassis were carried out. The selected values for the payload were 22.5 and 45 kg. The terrain properties were the ones listed under soil "B" in Table 4.1. The RCP climbing a slope of 7.5° with constant speed was simulated and the results are shown in Fig. 4.36.

The RCP showed a similar behaviour in the two cases for $\eta < 115$ N. When the NFD exceeds 115 N, the rover with a 45-kg payload developed a slip close to 90%, while with the lighter payload of 22.5 kg it was able to climb the slope keeping the slip under 40% until the NFD reached 150 N.

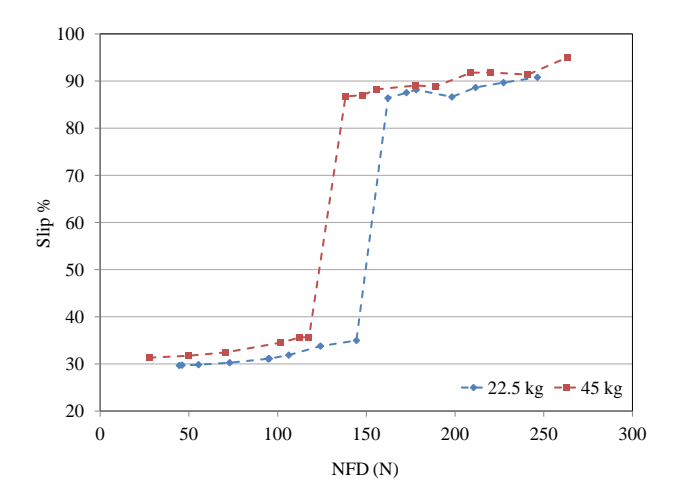


FIGURE 4.36. Slip-vs.-NFD plots for different payloads for the RCP climbing a 7.5° slope on soil "B" from Table 4.1

4.11 Obstacle climbing

Redundant actuation can also be employed to improve the rover performance during obstacle negotiation. To illustrate this concept the motion of the RCP overcoming a 0.1-m and 0.3-m-high obstacles (Figs. 4.37 and 4.38) was simulated using the multibody dynamics library.

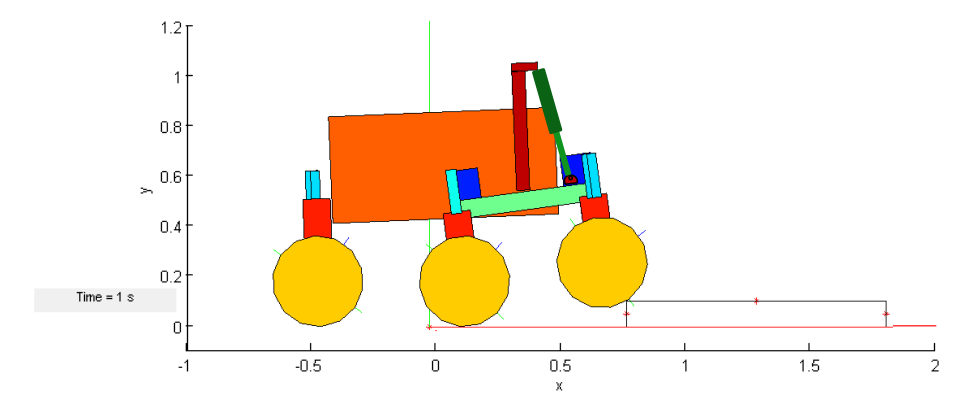


FIGURE 4.37. Multibody model of the RCP climbing a step obstacle of height $h=0.1~\mathrm{m}$ with no actuators

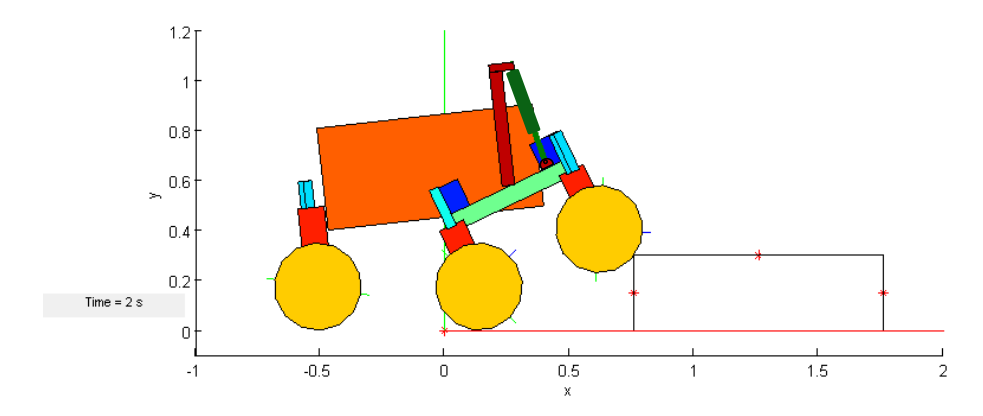


FIGURE 4.38. Multibody model of the RCP climbing a step obstacle of height $h=0.3~\mathrm{m}$ with actuators

The ground and step are assumed to be rigid surfaces and the wheel-ground interaction is defined by kinematic constraints, i.e., no-slip and no-penetration conditions. This represents a desired motion of the rover. Additionally, the same condition was enforced on the transition between the two faces of the obstacle, i.e., the wheels remaining in contact with the obstacle and revoluting with no slip about the corner. To this end, a virtual pin joint was defined and was activated once the contact between the wheel and the obstacle corner established, as shown in Fig. 4.39. Under these conditions, reaction forces F_{τ} and F_n represent respectively, the traction and normal force that the terrain or the obstacle surface need to provide so that the kinematic specifications are maintained during the manoeuvre.

In the simulation, the front and middle wheels of the RCP were actuated with a driving torque under velocity control, and the rear wheels were not powered. The motors for all the wheels were identical and a proportional controller was used to provide the required torque to maintain the target angular velocity for the wheels, ω_{ref} . The motor torque was bounded to be smaller that T_{lim} . Accordingly, the driving torques applied to the rover wheels were evaluated as

$$T_m = \min \left(T_{lim}, \ k \left(\omega - \omega_{ref} \right) \right) \tag{4.4}$$

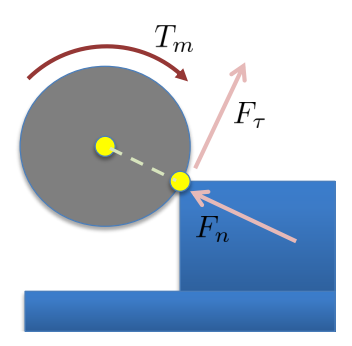


FIGURE 4.39. Modelling the no-slip revolution of the wheel about the corner of the step obstacle by placing a virtual pin joint at the contact point

where T_m is the motor driving torque, ω the angular velocity of the wheel relative to the suspension frame, ω_{ref} the desired angular velocity of the wheel, k the proportional gain, and T_{lim} the upper limit of the torque that can be delivered by the motor. In this study, ω_{ref} was set to 1.2 rad/s, and k = 100 Nms. This represented the real actuation system mounted on the RCP, where the rover is commanded by angular velocity input and the maximum available torque is limited by the size of the motors.

The driving torque requirement criterion was used to compare several redundant actuation strategies for the RCP. In each test a constant torque T_g in the range of $0 < T_g < 30$ Nm was exerted on the articulation between the bogies and the body. To assist climbing T_g must be applied in a way that it produces a normal load transfer from the front to the middle wheels. This action helps the front wheels to roll over the corner of the step. For each simulation the maximum torque T_{max} that the motors of the wheels must be able to provide in order to complete the manoeuvre was found. The magnitude of T_{max} dictates the required size of the wheel motors and is used as an indicator to compare different actuation strategies in this study.

In Figs. 4.40 and 4.41 the time-history of the motor torques of the front and middle wheels when the rover climbed a 0.1-m-high step are plotted. As stated

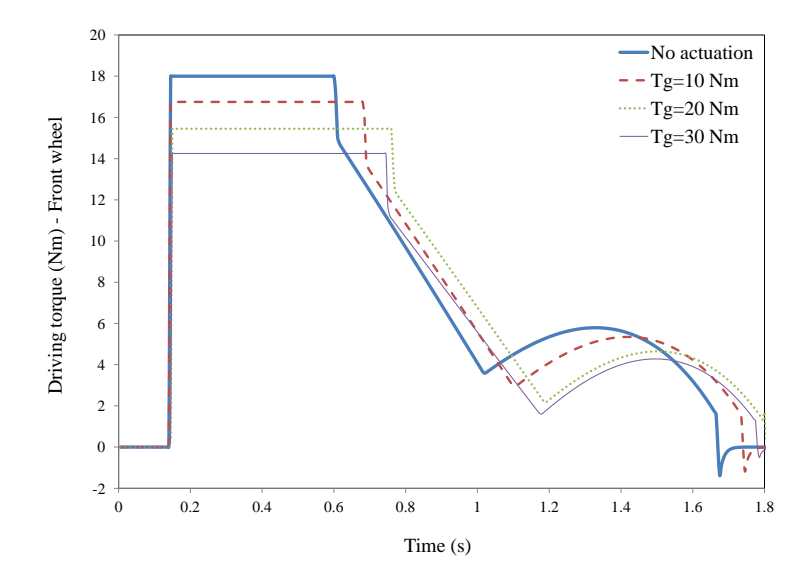


FIGURE 4.40. Torque applied to the front wheels of the RCP during the climbing a 0.1-m-high step for different values of the redundant actuation torque (T_g)

earlier, the rear wheels were not actuated. The rover is symmetric with respect to its longitudinal axis and the obstacle orientation was such that the wheels on both sides of the rover climbed the obstacle simultaneously. Therefore, only the results from the starboard side are presented in the plots.

The plots show that by actuating the bogies the maximum required driving torque of the wheels to complete the manoeuvre was reduced. Climbing the vertical wall is the part of the manoeuver which required the maximum torque from the motors of the wheels. The simulation was repeated for climbing a 0.3-m-high step. It was observed that similar to the previous case, the required motor torque of the wheels was reduced when bogie actuation was introduced. It must be noted that the negative values of the wheel torque are the result of velocity control operation mode. Equal velocity command was sent to all the wheels throughout the climbing. However, due to the irregularity of the ground in order to keep all the velocities equal, negative torques had to be applied by the controller to some wheel at different parts of

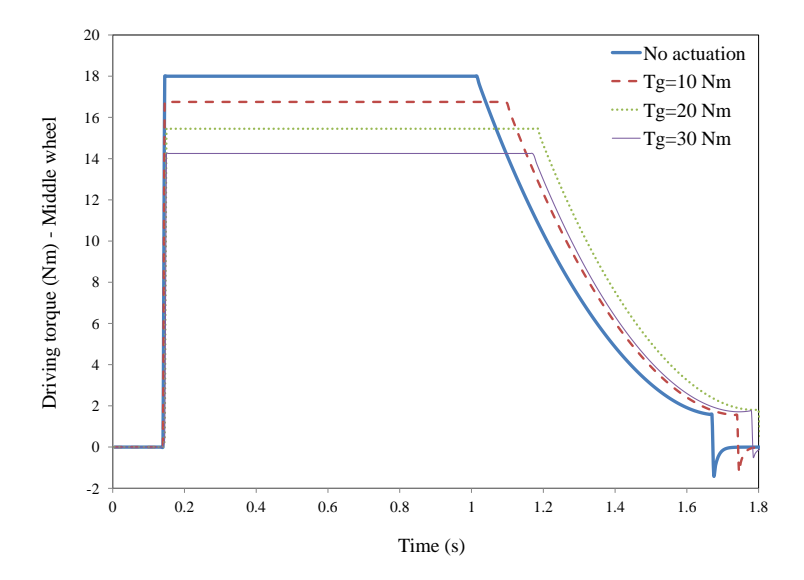


FIGURE 4.41. Torque applied to the middle wheels of the RCP during the climbing a 0.1-m-high step for different values of the redundant actuation torque (T_g)

the manoeuvre. As stated earlier, the important part of the motion for the purpose of this study was climbing the vertical wall. During this period the front wheels require the maximum torque. To obtain these results, a constant internal torque was applied on the bogic joints for the whole duration of the climbing manoeuvre. However, more complex control schemes can be adopted to regulate the internal torque in order to optimize the rover power consumption.

Finally, the presented results suggest that larger values of T_g will further reduce the required wheel motor torque T_{max} , but this requires a more powerful actuator at the articulation between the bogies and the body. Therefore, there is a trade-off between the torque requirement of the wheel motors and the bogie motors.

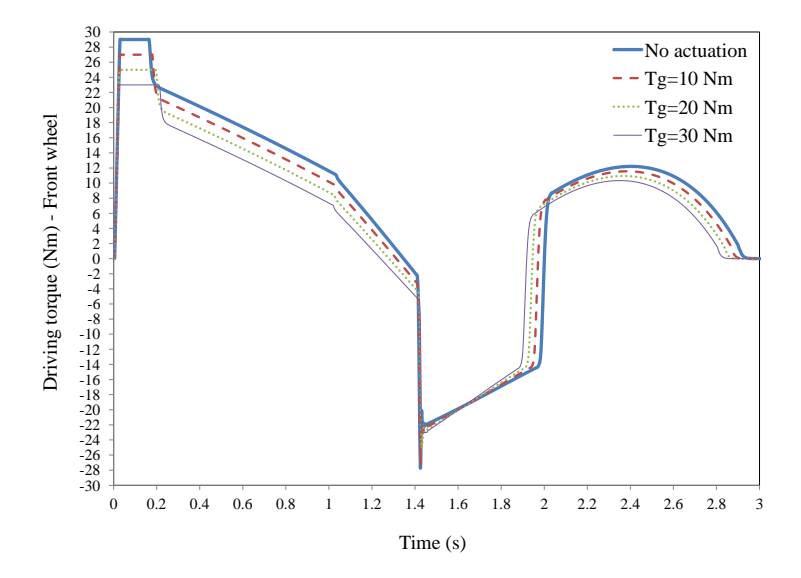


FIGURE 4.42. Torque applied to the front wheels of the RCP during the climbing a 0.3-m-high step for different values of the redundant actuation torque (T_q)

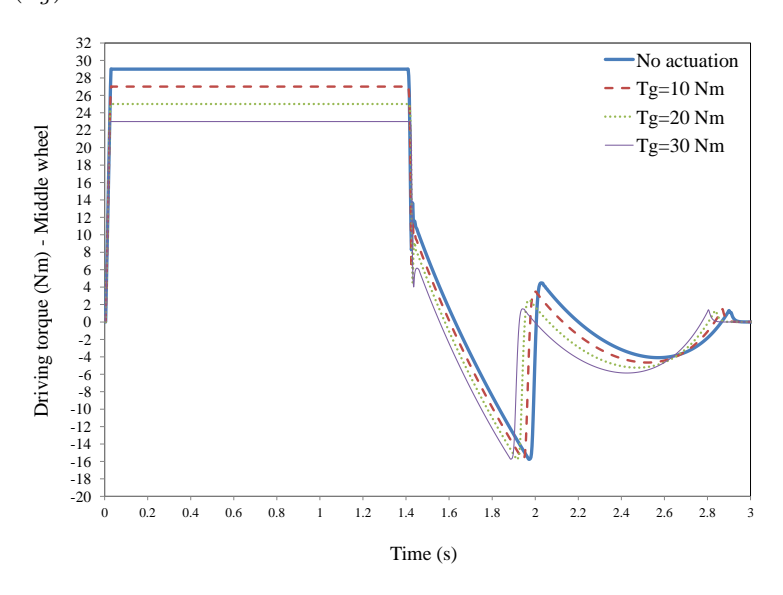


FIGURE 4.43. Torque applied to the front wheels of the RCP during the climbing a 0.3-m-high step for different values of the redundant actuation torque (T_q)

4.12 Multipass effect

The discussion in the previous sections relied on the assumptions that all the wheels had the same slip ratio and moved on the same type of soil. However, the normal force distribution can still provide relevant information about rover performance in cases in which these assumptions do not hold.

In this section we study those type of applications where the wheels are operated under velocity control with the same angular velocity command. In that case, when the rover travels on a straight line, given that all the components of the rover have the same translational velocity, it is reasonable to assume that all the wheels have the same slip ratio. However, in such applications the robot might travel on a nonhomogeneous terrain and therefore, each wheel would experience a different type of soil. Even in the case of homogeneous terrain, in some cases, the terrain can undergo significant property changes, due to the compaction caused by the passage of the wheels. In the operation of multi-axle vehicles on such terrains, the successive wheels experience a soil with different properties compared to the one experienced by the front wheels. This phenomenon is referred to as multipass effect. In order to find the most effective load distribution on these types of terrain, multipass effect has to be included in the model of the system. A special case is addressed in our study in which all the wheels have the same slip ratio and the variation of the soil properties is due to the multipass effect. Study of more general cases, where the wheels have different slip ratios and the rover travels on a non-homogeneous terrain follows the same methodology but is not discussed in detail in this thesis.

In the following sections, first terramechanics models which considers multipass effect in the calculation of terrain reaction forces are introduced. Then, a maximization problem is solved to find the set of normal forces that results in the highest total tangential force that the rover can develop. The analysis is performed for a given slip ratio of the wheels and certain soil and wheel properties.

4.12.1 Theory. The terramechanics expressions in Section 4.2 need to be modified to consider the effect of soil compaction by the front wheels of the vehicle. Earlier work in this area was reported in [52] and [51], where the rolling resistance of a wheel was evaluated assuming that the pressure-sinkage behaviour of the soil remains the same for all the passes. Therefore, the variation of the soil reaction forces in different passes must be due to the variation of the soil density or compaction. This assumption was later demonstrated experimentally [120], [121], [122].

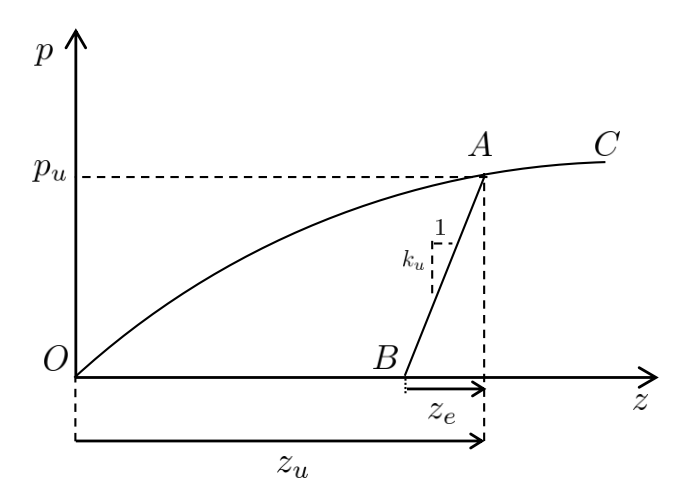


FIGURE 4.44. Schematic of repetitive loading characteristics of soil, obtained from reported bevameter tests [2]

Wong et al. [2] reported the results of pressure-sinkage bevameter tests on several terrain types. Their results suggest that the pressure-sinkage relation follows a curve like the one in Fig. 4.44. According to these results, first, the pressure under the wheel increases with sinkage along curve O-A. This curve is obtained based on the soil properties according to Eq. (3.11). When unloading starts at pressure p_u and total sinkage z_u , the pressure-sinkage relationship follows line A-B, i.e.,

$$p = p_u - k_u(z_u - z) \tag{4.5}$$

The slope of the A-B line is parameterized by k_u which is a function of z_u :

$$k_u = k_o + A_u z_u \tag{4.6}$$

where k_o and A_u have the units of kN/m³ and kN/m², respectively.

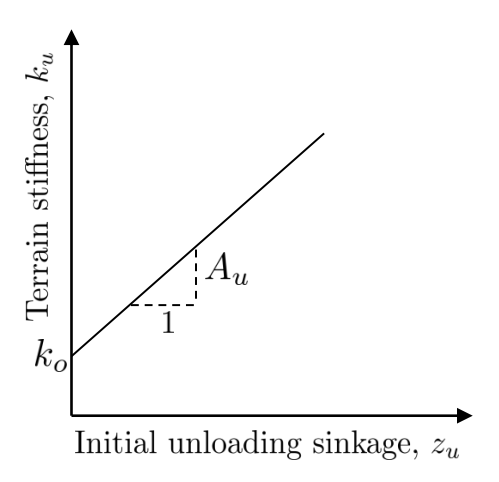


FIGURE 4.45. Relationship between the soil stiffness and initial unloading sinkage

This relation is shown in Fig. 4.45. Based on Eq. (4.6) higher sinkage at the end of the previous loading results in more soil compaction, which reduces the elastic rebound (z_e) during unloading.

The elastic rebound of the soil takes the total sinkage back to $z = z_u - z_e$. When the terrain is subject to the next wheel passage Eq. (4.5) can also represent the elastic reloading during which the sinkage can increase up to z_u . If the pressure on the terrain exceeds p_u the plastic deformation that occurs follows the original pressure-sinkage curve O-A-C.

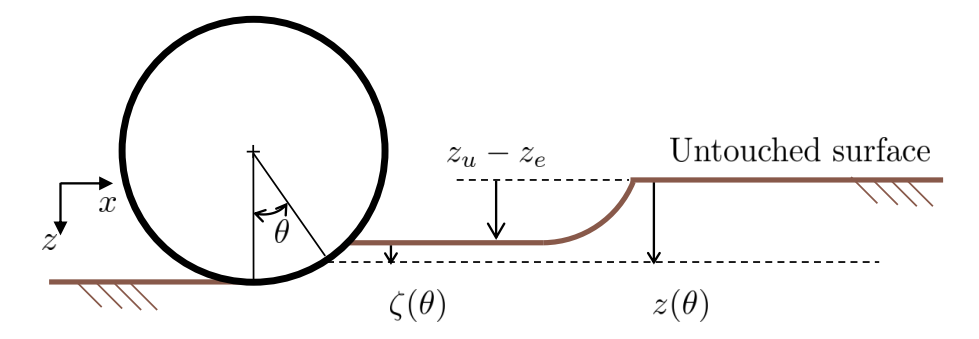


FIGURE 4.46. Schematic of wheel passage on a compacted soil and wheel's local and absolute sinkage measurements

In order to determine the terrain reactions the total sinkage has to be used in Eq. (3.11). The total sinkage at each point along the wheel-terrain contact area can be obtained from

$$z(\theta) = \zeta(\theta) + z_u - z_e \tag{4.7}$$

where $\zeta(\theta)$ is the sinkage measured locally from the surface of the already compacted terrain as shown in Fig. 4.46.

One complication associated with this method is that for each point on the terrain surface, the information about its deformation history, z_u and z_e , as well as its hardening parameters, k_o and A_u need to be stored [107]. Also, in the above approach the effect of wheel slip on the modification of terrain properties during each passage was not considered. An alternative approach was introduced in [122], where the variation of drawbar-pull, motion resistance force and torque, slip, sinkage, and tire deflection due to multiple wheel passages was studied with an extensive set of experiments. Driven wheels were found to cause significant changes in soil properties, while towed ones had only minor effects on them. A set of relations that fit these reported experimental results was presented in [3]. These relations can be used in simulation scenarios where multipass effect needs to be considered.

The approach followed in [3] is to update the soil parameters after each passage and find the terrain reactions by feeding the updated parameters to the terrame-chanics model. Therefore, the terramechanics model used to compute the reactions is the same for every passage. To this end, based on Holm's experimental results [122], Senatore and Sandu [3] introduced relations which give the variation of the soil properties as a function of the number of past passages and the condition of the previous passage. For example, Eq. (4.8) was proposed to represent the variation of the soil density as a function of the number of passes n_p and the slip ratio of the previous pass i_{s0} :

$$\gamma_{sn} = \gamma_s \left[1 + \left(1 - e^{\frac{-i_{s0}}{k_1}} \right) k_2 + k_3 n_p \right]$$
(4.8)

where γ_s is the density of the untouched soil, and k_1 , k_2 , and k_3 are dimensionless fitting constants.

Due to the lack of experimental data on the effect of multiple passages on the classical terramechanics parameters Senatore and Sandu [3] assumed that two other soil parameters have the same behaviour as the soil density and the rest remain unchanged. These two parameters are c, soil cohesion parameter, and K, soil shear displacement modulus. Under the above assumption, the way these parameters change follows the model given in Eq. (4.8), i.e.,

$$c_{sn} = c_s \left[1 + \left(1 - e^{\frac{-i_{s0}}{k_1}} \right) k_2 + k_3 n_p \right]$$
 (4.9)

$$K_{sn} = K_s \left[1 - \left(1 - e^{\frac{-i_{s0}}{k_1}} \right) k_2 - k_3 n_p \right]$$
 (4.10)

and k_1 , k_2 , and k_3 have the same value in all three equations (4.8), (4.9), and (4.10).

To include multipass effect in our generic multibody dynamics library the approach in [3] was adopted. Before calculation of the terrain reactions, the soil parameters are updated based on the history of the soil. The number of previous passages and the slip ratio of the last pass are used as the input to Eqs. (4.8)–(4.10) to obtain the updated value of γ , c, and K.

For comparison, some simulation results reported in [3] were reproduced using our code. Figure 4.47a shows the reported simulation results of the drawbar pull developed by the wheel for a range of slip ratios between 0.1 and 0.9 [3]. The same simulation tests were repeated for the second wheel pass after updating the soil properties. Information on the slip ratio of the first pass was required in order to simulate the second pass. Two cases were considered:

- Towed wheel in the first pass. A slight increase in the drawbar pull can be observed in the plot for this case.
- 50% slip in the first pass. Under this assumption, the soil compaction due to the first pass was considerable and therefore, the drawbar pull generated in the second pass was higher.

In order to reproduce these results using our library the soil properties and multipass parameters need to be known. The multipass parameters are given and listed in Table 4.9. The soil properties introduced in [3] are in a format slightly different from the one required by our library. The advantage of this alternative format is that the dimension of the pressure-sinkage parameters is no longer dependent on the value of n; on the other hand, the soil properties become a function of the wheel width.

In [3] the soil properties are reported in this alternative format but no information about the wheel dimensions and the vertical load supported by the wheel is provided. Due to this lack of information it was not possible to reproduce exactly the same simulation results using our multibody dynamics library.

Table 4.9. Parameters defined in [3] for the multipass model

| k_1 | k_2 | k_3 |
|--------|--------|--------|
| 0.1178 | 0.1672 | 0.0348 |

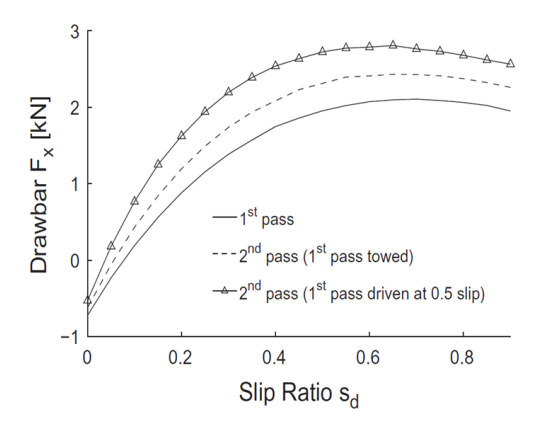
Table 4.10. Parameters introduced in [3] for terramechanics model

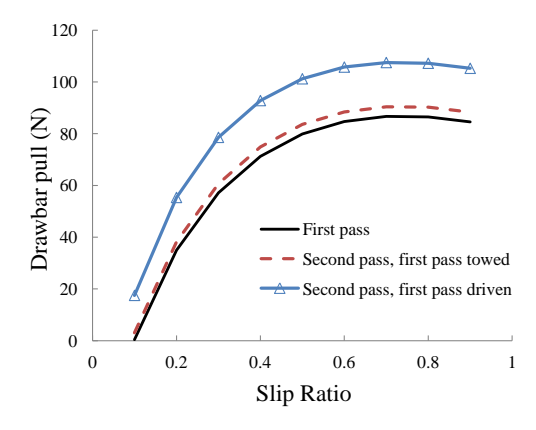
| \overline{n} | c | ϕ | k_c | k_{ϕ} | K |
|----------------|-----------|--------|---------------------------------|-------------------------|-------|
| (-) | (N/m^2) | (deg) | $(\mathbf{N}/\mathbf{m}^{n+1})$ | $(\mathrm{kN/m}^{n+2})$ | (m) |
| 0.7 | 1150 | 31.1 | 22131 | 441 | 0.015 |

Assumptions had to be made to choose the value of the missing parameters. The wheel width was assumed to be the same as the one of the RCP (0.15 m). The soil parameters given in [3] could then be converted to the format used in Table 4.10. The vertical load was set to 500 N. Figure 4.47b shows the simulation results of the drawbar pull provided by the GMDL, for the above scenarios. Comparison of Figs. 4.47a and 4.47b shows that modifications introduced in the soil model used in the GMDL led to prediction of the same behaviour reported in [3].

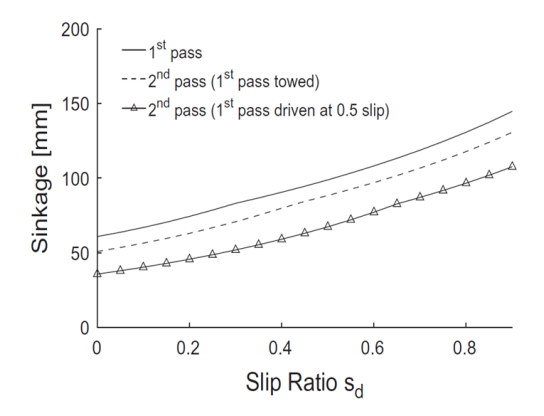
Figures 4.47c and 4.47d illustrate the wheel sinkage values reported in [3] and the ones obtained using the multibody library for the above scenarios, respectively. With the same reasoning, the sinkage of the second pass with the previous driven wheel pass is the lowest among the three as the wheel moves on a more compacted soil. The two sets of results show a similar trend in the way sinkage changes with different wheel slip and soil history. The comparison of the simulation results obtained by our code and with the ones reported in [3] allows for further validation of our library.

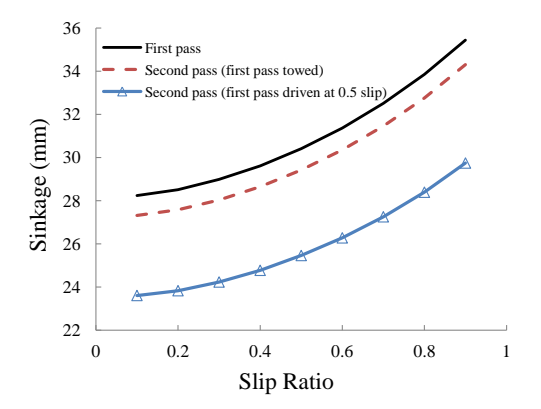
As discussed in Section 4.4, the objective of this study is to find the normal force distribution among the wheels of a vehicle which results in the development of the highest possible drawbar pull. The same objective is investigated here while considering the multipass effect. When considering multipass, the F_D -vs.- F_n relations





- (A) Drawbar pull variation reported by [3]
- (B) Drawbar pull variation results by the generic multibody dynamics library





- (C) Sinkage variation reported by [3]
- (D) Sinkage variation results by the generic multibody dynamics library

FIGURE 4.47. Multipass effect predicted by [3] and with the generic multibody dynamics library

for different wheels of the vehicle do not follow the same curve. In multi-axle vehicles, even when all the wheels have the same slip ratio, soil properties may not be the same for successive wheels passing the same patch of soil. For example, in the case of the RCP which has three axles, F_D -vs.- F_n curves for front, middle, and rear wheels can be different.

| iı | n the RC | P simulat | ion | | | | | |
|----|----------|-----------|-----|-------------|---|-------|---------|-------|
| | | | | | | | | |
| n. | C | φ | k. | k_{\cdot} | K | k_1 | k_{2} | k_2 |

Table 4.11. Soil parameters used for terramechanics and multipass models

| \overline{n} | c | ϕ | k_c | k_{ϕ} | K | k_1 | k_2 | k_3 |
|----------------|-----------|--------|---------------------------------|-------------------------|-------|--------|--------|--------|
| (-) | (N/m^2) | (deg) | $(\mathbf{N}/\mathbf{m}^{n+1})$ | $(\mathrm{kN/m}^{n+2})$ | (m) | (-) | (-) | (-) |
| 1 | 220 | 33.1 | 1400 | 820 | 0.015 | 0.1178 | 0.1672 | 0.0348 |

Motion of a single wheel with the same dimensions as the RCP wheels, on soft soil, with 50% slip was simulated using the generic multibody dynamics library. The soil parameters for this simulation are the ones listed under soil "B" in Table 4.1. Due to the smaller value of k_{ϕ} in soil "B", it undergoes a more significant compaction under the same load compared to soil "A", which makes it more suitable for the study of the multipass effect. The soil parameters are shown in Table 4.11. Parameters n, c, ϕ , k_c , k_{ϕ} , and K are used in the terramechanics model, while k_1 , k_2 , and k_3 are multipass parameters used in Eqs. (4.8)–(4.10).

Simulation results show that the passage of each wheel further compacts the soil and as a result in the subsequent passages the wheels will experience less sinkage in the compacted soil compared to the front wheels. Smaller sinkage leads to less resistant force R_c . Also, for a given normal force and slip ratio, drawbar pull generated on compacted soil is larger. Therefore, as it can be seen in Fig. 4.48a, for a certain value of the normal force the successive wheels develop more drawbar pull than the first wheels. This behaviour of the soil suggests that shifting the load toward the rear of the vehicle can increase the drawbar pull developed by the rover and improve its mobility.

4.12.1.1 Maximization problem. In order to determine the normal force distribution that maximizes the total drawbar pull of a rover, first, the F_D -vs.- F_n curves of all the wheels of the rover have to be generated. The data point required to obtain these curves can be obtained from the simulation of a single wheel motion on soft

soil, as described in the previous section. For a vehicle with k wheels, the F_D -vs.- F_n curve corresponding to wheel s is generated based on the parameters of the soil, wheel slip, and number and condition of previous passes on the soil. Each curve is then approximated by a polynomial. The polynomials provide the value of the DBP that each wheel can develop as a function of its normal load: $F_{Di} = f_i(F_n)$. The maximization problem can be formulated as follows:

$$\max_{\mathbf{f_n}} \sum_{i=1}^{p} F_{Di} \quad \text{s.t. } \sum_{i=1}^{p} F_{ni} = w_t \quad \text{and} \quad F_{Di} > 0$$
 (4.11)

where $\mathbf{f}_n = [F_{n1}, F_{n2}, \dots, F_{np}]^{\mathrm{T}}$ is the *p*-dimensional array of normal forces applied on the wheels of the rover, F_{ni} is the normal force at the i^{th} wheel, and w_t is the total load on the rover that has to be balanced by the terrain normal reactions. Next, the method developed in this section will be used to determine the optimum load distribution of the RCP for the given operation conditions.

Determining the exact load transfer that results in the optimum drawbar pull requires the solution of a maximization problem. From Fig. 4.48a it can be seen that the peak for each curve occurs at a certain normal force. Therefore, for example in the case of the rear wheel, which is associated with pass 3, if the normal load exceeds 550 N the developed drawbar pull decreases. This decrease is due to the fast growth of the rolling resistance force when the wheel sinkage is large. Moreover, these curves adopt a different shape for each value of the slip ratio and this difference has to be considered if the slip ratio of the wheels of the rover are not identical. The best distribution also depends on the total vertical load and weight of the rover.

4.12.2 Effect of normal force distribution considering the multiple pas-

sages. The methodology introduced in Section 4.12.1 is employed in the following simulation studies. The straight line motion of the RCP on flat, sandy soil with given values of the angular velocity of the wheels and slip ratio was simulated. The same

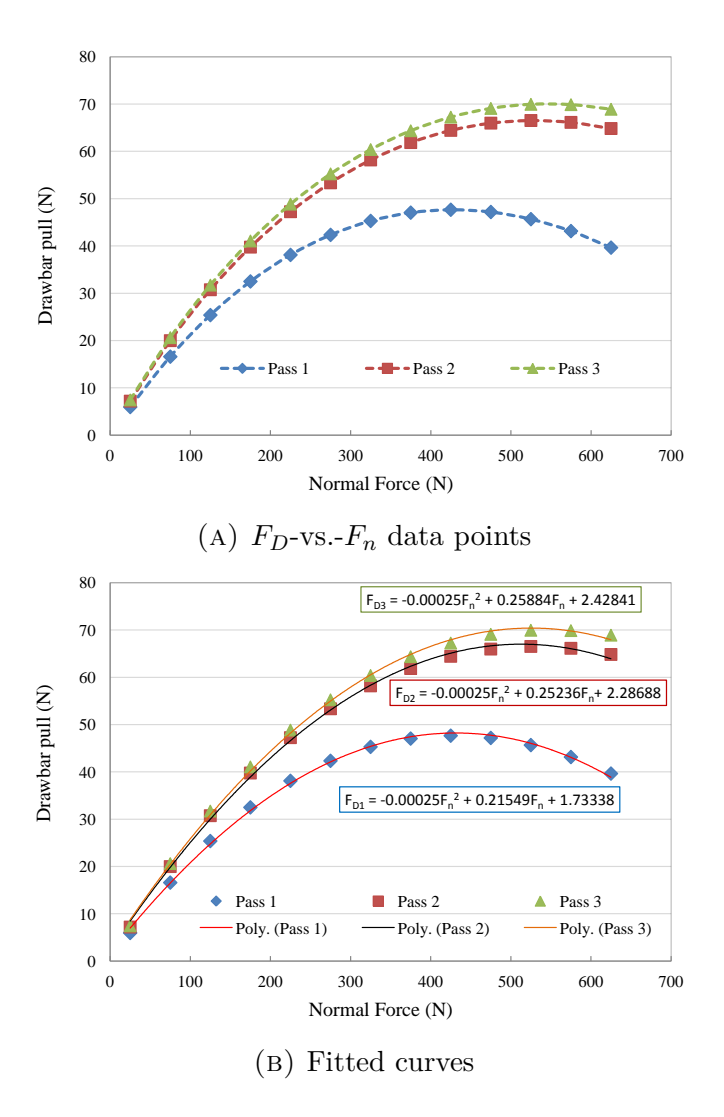


Figure 4.48. F_D -vs.- F_n relation for different number of wheel passages with 50% slip on soil "B"

scenarios described in Section 4.9 for the drawbar pull tests were used again. As already mentioned, a rheonomic constraint was defined to specify the translational velocity of the rover. The force associated with this constraint represented the drawbar pull developed by the rover. The objective of this study was to find the best normal force distribution for each scenario while considering the multipass effect.

Table 4.12. Solution of the maximization problem for the RCP operation on soil "B" with 50% slip

| Wheel | Front (F_{n1}) | Middle (F_{n2}) | Rear (F_{n3}) |
|-----------|------------------|-------------------|-----------------|
| F_n (N) | 181.5 | 259.1 | 271.8 |

In the first example the wheel slip was set to 50% and the rover operated on soil "B" of Table 4.1. This was the same operation condition as discussed in Section 4.12.1 for a single wheel simulation. Therefore, the three curves illustrated in Fig. 4.48a can represent the F_D -vs.- F_n curves for the front, middle, and rear wheels of the RCP. The polynomials which were fitted to the curves in Fig. 4.48a are displayed in Fig. 4.48b:

$$\begin{cases} F_{D1} = -0.00025F_n^2 + 0.21549F_n + 1.73338 \\ F_{D2} = -0.00025F_n^2 + 0.25236F_n + 2.28688 \\ F_{D3} = -0.00025F_n^2 + 0.25884F_n + 2.42841 \end{cases}$$

Second-degree polynomials were chosen for approximating the curves as the coefficient of higher-degree terms were found to be very small for the examples studies here. A maximization problem was solved to maximize $F_D = \sum_{i=1}^3 F_{Di}$ subject to the following constraint imposed by the total weight of the RCP:

$$w_t = 2(F_{n1} + F_{n2} + F_{n3}) = 1424.7 \text{ N}$$
 (4.12)

where F_{n1} , F_{n2} , and F_{n3} correspond to the normal forces on the front, middle, and rear wheels, respectively. The maxima of function F_D was found using its derivative with respect to F_n . The result of the maximization problem is shown in Table 4.12. With this set of normal forces, which results in an NFD of 43.7 N, the drawbar pull of the rover is maximized. Therefore, as these results suggest, if the multipass effect is considerable the best load distribution is not the even distribution.

Table 4.13. Solution of the maximization problem for the RCP operation on soil "A" with 60% slip

| Wheel | Front (F_{n1}) | $Middle(F_{n2})$ | Rear (F_{n3}) |
|-----------|------------------|------------------|-----------------|
| F_n (N) | 152.2 | 270.5 | 289.7 |

In order to verify the results of the optimization problem the drawbar pull test with the RCP was simulated using the same soil and slip ratio. The simulation was repeated for a range of different normal force distributions. The variation in load distribution was achieved by placing additional mass elements along the longitudinal axis of the rover body and introducing redundant actuation. Fig. 4.49a shows the drawbar pull developed for different load distributions. The maximum drawbar pull occurs with the load distribution obtained from the solution of the maximization problem ($\eta = 43.7$ N). More uniform normal force distributions developed smaller drawbar pulls.

The next simulation example was designed to mimic the experimental tests described in Section 4.9. The same slip ratio of 60% was prescribed for the motion of the RCP and soil "A" from Table 4.1 was used. The F_D -vs.- F_n curves for the soil and slip ratio of this scenario were obtained by simulating a single wheel motion. The following equations represent the second degree polynomials which closely fit the curves:

$$\begin{cases} F_{D1} = -0.00016F_n^2 + 0.25183F_n + 0.21912 \\ F_{D2} = -0.00016F_n^2 + 0.29135F_n + 0.56284 \\ F_{D3} = -0.00016F_n^2 + 0.29848F_n + 0.66572 \end{cases}$$

Again, the maximization problem was formulated with the above equations and subject to Eq. (4.12). The optimum normal forces in this case which result in an NFD of 66.6 N, are shown in Table 4.13.

Figure 4.49b shows the drawbar pull developed by the RCP in the simulations with 60% slip on soil "A". As in the previous example, the load distribution obtained in the maximization problem resulted in the maximum drawbar pull.

Further discussion on the results obtained for the second example is required. The second scenario is intended to represent the RCP drawbar pull experiments in the Mars Dome. However, several factors make the simulation results not close to reality. As it is described in Appendix A the terramechanics parameters were identified through simulation of numerous experimental tests. On the other hand, multipass parameters k_1 , k_2 , and k_3 used for simulations in this section are the ones introduced in [3]. Obtaining the multipass parameters for the soil in Mars Dome would have required further experimentation which has not yet been carried out. Therefore, due to uncertainty in soil parameters the suggested values of the normal force in Table 4.13 do not necessarily result in the highest drawbar pull in the real operation of the RCP. Also, the simulation results shown in Fig. 4.49b cannot precisely predict the value of the developed drawbar pull in the experiments. However, despite the discrepancies in the numerical values, both simulation and experimental results suggested that in the range of $60 < \eta < 150$ N, lower NFD results in development of higher drawbar pull. The experimental results supporting this behaviour were presented in Section 4.8.2. The ellipsoid in Fig. 4.49b shows the range of the NFD covered during the experiments. The multipass effect was assumed to be negligible during the experiments and consequently, the objective was to achieve an NFD of 0 N. Achieving a perfectly even distribution was not possible due to the limitations which existed on the position of the CoM and maximum allowable redundant actuation. Therefore, experimental tests for rover configurations with $\eta < 60$ were not carried out.

Comparison of the two examples discussed in this section showed that even with similar multipass parameters, due to the differences in the soil parameters and in the slip ratio the shape of F_D -vs.- F_n curves were not the same. Although the rover weight was the same in the two cases, two different solutions were obtained in the maximization problems. It must be noted that due to the nonlinear shape of the curves the obtained results cannot be scaled for a different rover weight.

Therefore, for every scenario the following three steps must be taken. First, single wheel motion simulation has to be repeated for a range of normal force to obtain the F_D -vs.- F_n curve for each passage. Next, the polynomials that closely approximate the curves need to be found. Finally, the maximization problem must be solved to find the optimum normal force distribution.

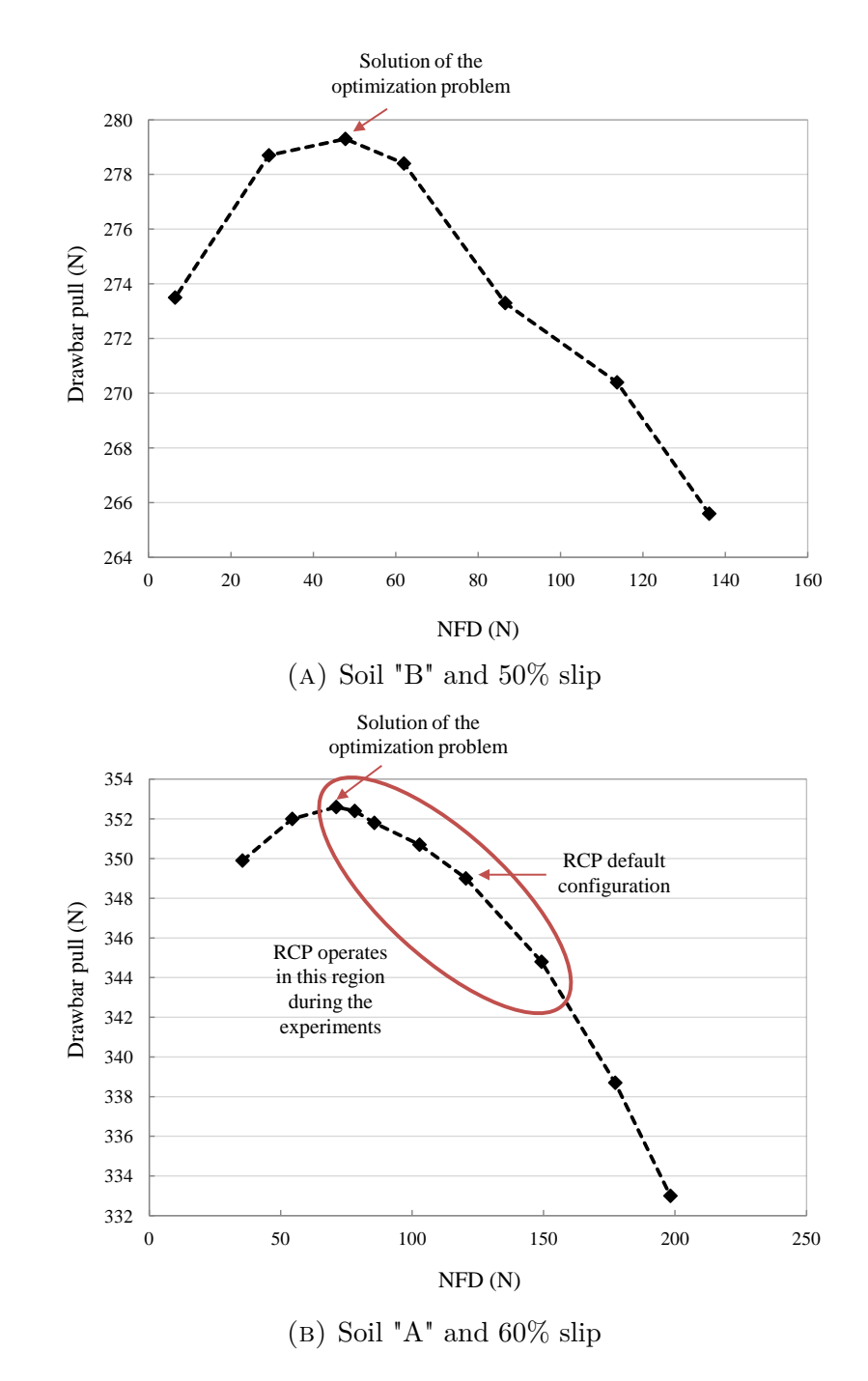


FIGURE 4.49. Drawbar pull variation for a range of NFD values considering multipass effect

CHAPTER 5

Closing Remarks

5.1 Conclusions

The performance analysis of rovers operating on unstructured terrain can be investigated using performance indicators based on different possible models. We particularly looked at the possibility of applying what we term observative models for the analysis. A central idea of the proposed approach is to model the vehicle-terrain interaction with representative, desired kinematic specifications, and use the resulting constraint reactions as primary variables to evaluate the effect of system parameter changes on the dynamic behaviour and performance. As shown in Chapter 3, such models can capture the effect of changes in system parameters on the dynamic behaviour. Observative models can be used to streamline the design and operation of planetary exploration vehicles. These can have a number of advantages: they are computationally inexpensive, can be used for sensitivity and inverse-dynamics analyses, and can be employed regardless of the properties of the terrain on which the rover operates. They give rise to the possibility of developing performance indicators as functions of rover parameters and state. The resulting constraint reactions are complementary to the motion restricted by the kinematic specifications. It was shown

CHAPTER 5. CLOSING REMARKS

that tangential and normal forces defined via such models can be used as performance indicators of a rover, thereby eliminating the need for the detailed parametrization of the soil.

The performance indicators defined using the observative modelling approach were compared to the results obtained with the predictive forward-dynamics simulations using terramechanics relations. They were also validated against experimental results using a rover prototype. Results showed that the reaction forces associated with both the no-slip and no-penetration conditions can be meaningful indicators of rover mobility for design and operation analyses. Tangential forces can be used to assess how a change in the system parameters can influence the development of slip. Normal force distribution obtained based on the observative approach was used to investigate different inertia distributions of the experimental rover prototype to increase its ability to develop traction and drawbar pull.

In Chapter 4, the effect of normal force distribution on the mobility of wheeled robots was studied. A performance indicator that quantifies the dispersion of the normal force at the wheel-terrain interfaces was defined. This indicator can be used to enhance the mobility of a wheeled robot on soft soil, including slope negotiation manoeuvres, providing guidelines for configuration and actuation changes on the rover suspension in order to increase drawbar pull. The actual impact of the normal force distribution on the available drawbar pull was found to depend on a set of factors. As a case study, the effect of the defined indicator on the performance of a six-wheeled rover prototype was considered. Simulation results confirmed that reducing the normal force dispersion resulted in improved rover performance in drawbar-pull tests. These results were experimentally validated with a rover prototype. The normal load distribution was modified via CoM repositioning and redundant actuation. To realize redundant actuation a set of pneumatic actuators were installed on the rover. The result of drawbar pull tests with the modified rover chassis validated the simulation

results and confirmed the effectiveness of redundant actuation to modify the NFD in the course of rover operations. Furthermore, simulation results of step climbing manoeuvres showed that with the aid of bogie actuation the rover can climb larger obstacles with a lower torque requirement on the wheels. Finally, the optimal normal force distribution was determined including the consideration of the multipass effect. Optimum load distributions were obtained as the solution of a maximization problem. Simulations confirmed that these distributions resulted in the development of the maximum possible drawbar pull.

The simulation studies in this thesis were carried out using our generic multibody dynamics library. The motivation for developing this library was providing a generic analysis tool which also specifically addresses the challenges in modelling mobile robots and their interaction with the environment. To this end, the terramechanics relations which are originally developed for planar motion were implemented in the library for spatial simulation. The multibody models of several rover concepts were developed in order to provide a virtual prototyping platform to test ideas and algorithms. Several formulations and algorithms to solve dynamic equations of multibody systems, as well as few integrators are implemented in the library. The open architecture of the code makes it suitable for various analyses of complex systems by providing access to the internal functions of the library and exposing the terms and parameters of the system model during the simulation. This also enables the user to have control over the solution of redundantly constrained systems as well as providing options for customizing the way the system interacts with the environment.

5.2 Recommendations for future work

The concept of observative models introduced in Chapter 3 provides a novel framework for analysis of rover performance. We used such models to obtain information about the reaction forces developed at the wheel in order to analyze the

CHAPTER 5. CLOSING REMARKS

mobility of the rover. However, the study of other aspects of the rover behaviour, such as steerability, power consumption, stability, etc., can also benefit from the proposed concept. Furthermore, the application of this concept is not limited to rovers and can be extended to other mechanical systems as well.

The guidelines on the distribution of normal forces in wheeled robots, proposed in Chapter 4, were based on the F_D -vs.- F_n relationship obtained for each wheel. The study was extended to a more general scenario, where multipass effect resulted in variation of the F_D -vs.- F_n relation among different wheels of the rover. In this regard, considering other conditions that can also affect this relation would extend the applicability of the study and would provide design and operational guidelines for more complex cases. Furthermore, the NFD defined in this work has the unit of Newtons and is suitable to compare the effect of different design and operation parameters on the performance of a single system. It can be useful to define a non-dimensional performance indicator in order to compare several systems in terms of their mobility. However, selection of proper way of normalizing NFD requires further investigations.

Several analysis tools have been included in the multibody library. Parametrization of systems using other sets of coordinates has been discussed which can provide interesting insights into their behaviour. A minimum set of coordinates which uses the joint variables as the degrees of freedom is one of the useful ways of parametrization of multibody systems. It would be valuable to make use of this alternative parameterizations for analysis of multibody systems.

- [1] A. Azimi, M. Hirschkorn, B. Ghotbi, J. Kövecses, J. Angeles, P. Radziszewski, M. Teichmann, M. Courchesne, and Y. Gonthier, "Terrain modelling in simulation-based performance evaluation of rovers," *Canadian Aeronautics and Space Journal*, vol. 57, no. 1, pp. 24–33, 2011.
- [2] J. Wong, M. Garber, and J. Preston-Thomas, "Theoretical prediction and experimental substantiation of the ground pressure distribution and tractive performance of tracked vehicles," *Proceedings of the Institution of Mechanical Engineers, Part D: Transport Engineering*, vol. 198, no. 4, pp. 265–285, 1984.
- [3] C. Senatore and C. Sandu, "Off-road tire modeling and the multi-pass effect for vehicle dynamics simulation," *Journal of Terramechanics*, vol. 48, no. 4, pp. 265–276, 2011.
- [4] "Mars Pathfinder." [Internet], [cited 2015, November 30]. Available from: http://mars.nasa.gov/programmissions/missions/past/pathfinder/.
- [5] "Mars Exploration Rover Mission." [Internet], [cited 2015, November 30]. Available from: http://mars.nasa.gov/mer/home/.
- [6] S. W. Squyres, A. H. Knoll, R. E. Arvidson, J. W. Ashley, J. Bell, W. M. Calvin, P. R. Christensen, B. C. Clark, B. A. Cohen, P. De Souza, et al., "Exploration of Victoria crater by the Mars rover Opportunity," Science, vol. 324, no. 5930, pp. 1058–1061, 2009.

- [7] R. Volpe, "Rover technology development and mission infusion beyond MER," in 2005 IEEE Aerospace Conference, (Big Sky, MT, USA), pp. 971–981, 2005.
- [8] M. Van Winnendael, P. Baglioni, A. Elfving, F. Ravera, J. Clemmet, and E. Re, "The ExoMars Rover-Overview of phase B1 results," in *Proceedings of the 9th International Symposium on Artificial Intelligence, Robotics and Automation in Space*, (Los Angeles, CA, USA), 2008.
- [9] C. R. Neal, "The Moon 35 years after Apollo: What's left to learn?," *Chemie der Erde-Geochemistry*, vol. 69, no. 1, pp. 3–43, 2009.
- [10] "Curiosity Rover." [Internet], [cited 2015, November 30]. Available from: http://mars.nasa.gov/msl/mission/overview/.
- [11] M. Van Winnendael, P. Baglioni, and J. Vago, "Development of the ESA ExoMars rover," in *Proceedings of 8th International Symposium on Artificial In*telligence, Robotics Automation in Space, (Munich, Germany), pp. 5–8, 2005.
- [12] "2020 Mission Plans." [Internet], [cited 2015, November 30]. Available from: http://mars.nasa.gov/programmissions/missions/future/mars2020/.
- [13] "MapleSim." [Internet], [cited 2015, November 30]. Available from: http://www.maplesoft.com/products/maplesim/.
- [14] T. Thueer, A. Krebs, R. Siegwart, and P. Lamon, "Performance comparison of rough-terrain robots – simulation and hardware," *Journal of Field Robotics*, vol. 24, no. 3, pp. 251–271, 2007.
- [15] "SIMPACK." [Internet], [cited 2015, November 30]. Available from http://www.simpack.com/.
- [16] "Siemens PLM Software." [Internet], [cited 2015, November 30]. Available from: http://www.plm.automation.siemens.com/.
- [17] "RecurDyn." [Internet], [cited 2015, November 30]. Available from: http://eng.functionbay.co.kr/.

- [18] "Adams." [Internet], [cited 2015, November 30]. Available from: http://www.mscsoftware.com/product/adams.
- [19] "Vortex by CM Labs." [Internet], [cited 2015, November 30]. Available from: http://www.cm-labs.com/robotics.
- [20] "Gazebo." [Internet], [cited 2015, November 30]. Available from: http://gazebosim.org/.
- [21] "MBDyn." [Internet], [cited 2015, November 30]. Available from: https://www.mbdyn.org/.
- [22] "SimMechanics." [Internet], [cited 2015, November 30]. Available from: http://www.mathworks.com/products/simmechanics/.
- [23] "SOLIDWORKS Motion." [Internet], [cited 2015, November 30]. Available from: http://www.solidworks.com/sw/products/simulation/motion-analysis.htm.
- [24] "DARTS." [Internet], [cited 2015, November 30]. Available from: http://dshell.jpl.nasa.gov/DARTS/index.php.
- [25] A. Jain, J. Guineau, C. Lim, W. Lincoln, M. Pomerantz, G. Sohl, and R. Steele, "ROAMS: Planetary surface rover simulation environment," in *Proceedings of the 7th International Symposium on Artificial Intelligence, Robotics and Automation in Space: i-SAIRAS 2003*, (Nara, Japan), 2003.
- [26] "ROAMS." [Internet], [cited 2015, November 30]. Available from: http://dshell.jpl.nasa.gov/ROAMS/index.php.
- [27] B. Trease, R. Arvidson, R. Lindemann, K. Bennett, F. Zhou, K. Iagnemma, C. Senatore, and L. Van Dyke, "Dynamic modeling and soil mechanics for path planning of the Mars Exploration Rovers," in *Proceedings of the ASME 2011 International Design Engineering Technical Conferences & Computers and Information in Engineering Conference*, (Washington, DC, USA), 2011.

- [28] R. Lindemann, D. B. Bickler, B. D. Harrington, G. M. Ortiz, C. J. Voothees, et al., "Mars Exploration Rover mobility development," Robotics & Automation Magazine, IEEE, vol. 13, no. 2, pp. 19–26, 2006.
- [29] P. Lamon and R. Siegwart, "Wheel torque control in rough terrain-modeling and simulation," in *Proceedings of the 2005 IEEE International Conference on Robotics and Automation*, pp. 867–872, IEEE, 2005.
- [30] A. Jain, J. Cameron, C. Lim, and J. Guineau, "SimScape terrain modeling toolkit," in Second International Conference on Space Mission Challenges for Information Technology SMC-IT 2006, (Pasadena, CA, USA), 2006.
- [31] "SimScape." [Internet], [cited 2015, November 30]. Available from: http://dshell.jpl.nasa.gov/SimScape/index.php.
- [32] AESCO, Matlab/Simulink Module AESCO Soft Soil Tyre Model (AS²TM) User's Guide, 2003.
- [33] I. C. Schmid, "Interaction of vehicle and terrain results from 10 years research at IKK," *Journal of Terramechanics*, vol. 32, no. 1, pp. 3–26, 1995.
- [34] R. Bauer, T. Barfoot, W. Leung, and G. Ravindran, "Dynamic simulation tool development for planetary rovers," *International Journal of Advanced Robotic* Systems, vol. 5, no. 3, pp. 311–314, 2008.
- [35] M. G. Bekker, *Introduction to Terrain-Vehicle Systems*. Ann Arbor: The University of Michigan Press, 1969.
- [36] J. Y. Wong, Theory of Ground Vehicles. New Jersey: John Wiley & Sons, Inc, fourth ed., 2008.
- [37] S. Michaud, L. Richter, N. Patel, T. Thüer, T. Huelsing, L. Joudrier, R. Siegwart, and A. Ellery, "RCET: Rover Chassis Evaluation Tools," in *Proceedings of the 8th ESA Workshop on Advanced Space Technology for Robotics and Automation (ASTRA)*, (Noordwijk, The Netherlands), 2004.

- [38] D. Apostolopoulos, Analytic Configuration of Wheeled Robotic Locomotion.

 PhD thesis, Robotics Institute, Carnegie Mellon University, 2001.
- [39] Surrey Space Center, "Rover Mobility Performance Evaluation Tool (RMPET): a systematic tool for rover chassis evaluation via application of Bekker theory," in *Proceedings of the 8th ESA Workshop on Advanced Space Technologies for Robotics and Automation ASTRA 2004*, (Noordwijk, The Netherlands), 2004.
- [40] R. N. Yong and E. A. Fattah, "Prediction of wheel-soil interaction and performance using the finite element method," *Journal of Terramechanics*, vol. 13, no. 4, pp. 227–240, 1976.
- [41] K. Xia, "Finite element modeling of tire/terrain interaction: Application to predicting soil compaction and tire mobility," *Journal of Terramechanics*, vol. 48, pp. 113–123, 2011.
- [42] J. Perumpral, J. Liljedahl, and W. Perloff, "A numerical method for predicting the stress distribution and soil deformation under a tractor wheel," *Journal of Terramechanics*, vol. 8, no. 1, pp. 9–22, 1971.
- [43] R. Yong and E. Fattah, "Prediction of wheel-soil interaction and performance using the finite element method," *Journal of Terramechanics*, vol. 13, no. 4, pp. 227–240, 1976.
- [44] P. Boosinsuk and R. Yong, "Soil compliance influence on tyre performance," in *Proceedings of the 8th International ISTVS Conference*, (Cambridge, UK), 1984.
- [45] C. H. Liu and J. Y. Wong, "Numerical simulation of tire-soil interaction based on critical state soil mechanics," *Journal of Terramechanics*, vol. 33, pp. 209– 221, 1996.
- [46] T. Shikanai, K. Hashiguchi, Y. Nohse, M. Ueno, and T. Okayasu, "Precise measurement of soil deformation and fluctuation in drawbar pull for steeland rubber-coated rigid wheel," *Journal of Terramechanics*, vol. 37, pp. 21–39,

2000.

- [47] D. A. Horner, J. F. Peters, and A. Carrillo, "Large scale discrete element modeling of vehicle-soil interaction," *Journal of engineering mechanics*, vol. 127, no. 10, pp. 1027–1032, 2001.
- [48] A. Oida, S. Ohkubo, and H. Schwanghart, "Effect of tire lug cross section on tire performance simulated by distinct element method," in *Proceedings of* the 13th International Conference of ISTVS, (Munich, Germany), pp. 345–352, 1999.
- [49] M. Momozu, A. Oida, and H. Nakashima, "Simulation of shear box test by the distinct element method," in *Proceedings of the 6th Asia-Pacific ISTVS conference*, (Bangkok, Thailand), pp. 181–8, 2001.
- [50] A. Azimi, J. Kövecses, and J. Angeles, "Wheel-soil interaction model for rover simulation and analysis using elastoplasticity theory," *Robotics, IEEE Trans*actions on, vol. 29, no. 5, pp. 1271–1288, 2013.
- [51] M. G. Bekker, Theory of Land Locomotion. Ann Arbor, Michigan: The University of Michigan Press, 1965.
- [52] M. G. Bekker, Off the Road Locomotion. Ann Arbor, Michigan: The University of Michigan Press, 1960.
- [53] J. Wong and A. Reece, "Prediction of rigid wheel performance based on the analysis of soil-wheel stresses. part I. performance of driven rigid wheels," *Jour*nal of Terramechanics, vol. 4, no. 1, pp. 81–98, 1967.
- [54] K. Iagnemma, "A laboratory single wheel testbed for studying planetary rover wheel-terrain interaction," tech. rep., MIT Field and Space Robotics Laboratory 01-05-05, 2005.
- [55] K. Yoshida and T. Shiwa, "Development of a research testbed for exploration rover at Tohoku University," The Journal of Space Technology and Science, vol. 12, no. 1, pp. 9–16, 1996.

- [56] S. Michaud, L. Richter, T. Thueer, A. Gibbesch, T. Huelsing, N. Schmitz, S. Weiss, A. Krebs, N. Patel, L. Joudrier, et al., "Rover chassis evaluation and design optimisation using the RCET," in Proceedings of ASTRA, 9th ESA Workshop on Advanced Space Technologies for Robotic and Automation, 2006.
- [57] K. Iizuka, Y. Sato, Y. Kuroda, and T. Kubota, "Study on wheel of exploration robot on sandy terrain," in *Proceedings of the 2006 IEEE International Con*ference on Intelligent Robots and Systems, (Beijing, China), pp. 4272–4277, 2006.
- [58] S. Hutangkabodee, Y. H. Zweiri, L. D. Seneviratne, and K. Althoefer, "Validation of soil parameter identification for track-terrain interaction dynamics," in *Proceedings of the 2007 IEEE/RSJ International Conference on Intelligent Robots and Systems*, (San Diego, CA, USA), pp. 3174–3179, 2007.
- [59] B. Rebele, A. Wedler, M. Apfelbeck, and H. Hirschmüller, "Advanced testbed and simulation environment for planetary exploration and mobility investigations," *IEEE Transactions on Pattern Analysis and Machine Intelligence*, vol. 30, no. 2, pp. 328–341, 2008.
- [60] G. Ishigami, A. Miwa, K. Nagatani, and K. Yoshida, "Terramechanics-based model for steering maneuver of planetary exploration rovers on loose soil," *Journal of Field Robotics*, vol. 24, no. 3, pp. 233–250, 2007.
- [61] L. Ding, K. Nagatani, K. Sato, A. Mora, K. Yoshida, H. Gao, and Z. Deng, "Terramechanics based high-fidelity dynamics simulation for wheeled mobile robot on deformable rough terrain," in *Proceedings of the 2010 IEEE Inter*national Conference on Robotics and Automation, (Anchorage, AK, USA), pp. 4922–4927, 2010.
- [62] J. Wong and A. Reece, "Prediction of rigid wheel performance based on the analysis of soil-wheel stresses. part II. performance of towed rigid wheels," *Journal of Terramechanics*, vol. 4, no. 2, pp. 7–25, 1967.

- [63] D. Gee-Clough, "The Bekker theory of rolling resistance amended to take account of skid and deep sinkage," *Journal of Terramechanics*, vol. 13, no. 2, pp. 87–105, 1976.
- [64] I. Shmulevich, U. Mussel, and D. Wolf, "The effect of velocity on rigid wheel performance," *Journal of Terramechanics*, vol. 35, pp. 189–207, 1998.
- [65] Z. Jia, W. Smith, and H. Peng, "Fast analytical models of wheeled locomotion in deformable terrain for mobile robots," *Robatica*, vol. 31, no. 1, pp. 35–53, 2012.
- [66] B. J. Chan and C. Sandu, "Development of a 3-D quasi-steady-state tyre model for on-road and off-road vehicle dynamics simulations: Part II-off-road rigid wheel model," *International Journal of Vehicle Systems Modelling and Testing*, vol. 9, no. 2, pp. 107–136, 2014.
- [67] B. J. Chan and C. Sandu, "Development of a 3-D quasi-steady state tyre model for on-road and off-road vehicle dynamics simulations: Part III-off-road flexible tyre model," *International Journal of Vehicle Systems Modelling and Testing*, vol. 9, no. 2, pp. 151–176, 2014.
- [68] B. Ghotbi, A. Azimi, J. Kövecses, and J. Angeles, "Sensitivity analysis of mobile robots for unstructured environments," in Proceedings of the ASME 2011 International Design Engineering Technical Conferences & Computers and Information in Engineering Conference IDTC/CIE 2011, DETC2011-48440, (Washington, DC, USA), 2011.
- [69] H. Moore, G. Clow, and R. Hutton, "A summary of Viking sample-trench analyses for angles of internal friction and cohesions," *Journal of Geophysical Research: Solid Earth* (1978–2012), vol. 87, no. B12, pp. 10043–10050, 1982.
- [70] J. Matijevic, J. Crisp, D. Bickler, R. Banes, B. Cooper, H. Eisen, et al., "Characterization of the Martian surface deposits by the Mars Pathfinder rover, Sojourner," Science, vol. 278, no. 5344, pp. 1765–1768, 1997.

- [71] H. J. Moore, D. B. Bickler, J. A. Crisp, H. J. Eisen, J. A. Gensler, A. F. Haldemann, J. R. Matijevic, L. K. Reid, and F. Pavlics, "Soil-like deposits observed by Sojourner, the Pathfinder rover," *Journal of Geophysical Research: Planets* (1991–2012), vol. 104, no. E4, pp. 8729–8746, 1999.
- [72] R. Sullivan, R. Anderson, J. Biesiadecki, T. Bond, and H. Stewart, "Martian regolith cohesions and angles of internal friction from analysis of MER wheel trenches," in *Lunar and Planetary Science Conference*, vol. 38, 2007.
- [73] L. Seneviratne, Y. Zweiri, S. Hutangkabodee, Z. Song, X. Song, S. Chhaniyara, S. Al-Milli, and K. Althoefer, "The modelling and estimation of driving forces for unmanned ground vehicles in outdoor terrain," *International Journal of Modelling, Identification and Control*, vol. 6, no. 1, pp. 40–50, 2009.
- [74] L. Ojeda, J. Borenstein, and G. Witus, "Terrain trafficability characterization with a mobile robot," in *Proceedings of the SPIE Defense and Security Con*ference, (Orlando, FL, USA), pp. 235–243, 2005.
- [75] K. Iagnemma, S. Kang, H. Shibly, and S. Dubowsky, "Online terrain parameter estimation for wheeled mobile robots with application to planetary rovers," *IEEE Transactions on Robotics*, vol. 20, no. 5, pp. 921 – 927, 2004.
- [76] L. Ding, K. Yoshida, K. Nagatani, H. Gao, and Z. Deng, "Parameter identification for planetary soil based on decoupled analytical wheel-soil interaction terramechanics model," in *Proceedings of 2009 IEEE/RSJ international conference on intelligent robots and systems*, (St. Louis, MO, USA), pp. 4122–4127, 2009.
- [77] P. Lamon, A. Krebs, M. Lauria, R. Siegwart, and S. Shooter, "Wheel torque control for a rough terrain rover," in *Proceedings of the 2004 IEEE International Conference on Robotics and Automation*, (New Orleans, LA, USA), 2004.
- [78] T. Thueer and R. Siegwart, "Mobility evaluation of wheeled all-terrain robots," *Robotics and Autonomous Systems*, vol. 58, no. 5, pp. 508–519, 2010.

- [79] P. Zhang, Z. Deng, M. Hu, and H. Gao, "Mobility performance analysis of Lunar rover based on terramechanics," in Advanced Intelligent Mechatronics, 2008. AIM 2008. IEEE/ASME International Conference on, pp. 120–125, 2008.
- [80] K. Iagnemma and S. Dubowsky, "Mobile robot rough-terrain control (RTC) for planetary exploration," in *Proceedings of the 26th ASME Biennial Mechanisms* and Robotics Conference, DETC, vol. 2000, 2000.
- [81] K. Iagnemma and S. Dubowsky, "Vehicle wheel-ground contact angle estimation: with application to mobile robot traction control," in proceeding of the 7th International Symposium on Advances in Robot Kinematics, ARK 00, 2002.
- [82] K. Yoshida and H. Hamano, "Motion dynamics of a rove rwith slip-based traction model," in *Proceeding of 2002 IEEE International Conference on Robotics and Automation*, (Washington, DC), pp. 3155–3160, 2002.
- [83] K. Yoshida, T. Watanabe, N. Mizuno, and G. Ishigami, "Slip, traction control, and navigation of a Lunar rover," in Proceedings of the 7th International Symposium on Artificial Intelligence, Robotics and Automation in Space, NARA, Japan, 2003.
- [84] G. Ishigami, A. Miwa, K. Nagatani, and K. Yoshida, "Terramechanics-based analysis on slope traversability for a planetary exploration rover," in *Proceed*ings of the International Symposium on Space Technology and Science, vol. 25, pp. 1025–1030, 2006.
- [85] S. Sreenivasan and B. Wilcox, "Stability and traction control of an actively actuated micro-rover," *Journal of Robotic Systems*, vol. 11, no. 6, pp. 487–502, 1994.
- [86] E. Papadopoulos and D. Rey, "A new measure of tipover stability margin for mobile manipulators," in *In Proceedings of 1996 IEEE International Confer*ence on Robotics and Automation, vol. 4, pp. 3111–3116, 1996.

- [87] C. Grand, F. BenAmar, F. Plumet, and P. Bidaud, "Stability control of a wheel-legged mini-rover," in *In Proceedings of the 5th Int. Conference on Climbing on Walking Robots (CLAWAR02)*, pp. 323–331, 2002.
- [88] Ö. Kilit and A. Yontar, "Stability of a new Mars rover with multi-stage bogie mechanism," in *In Proceedings of the 4th International Conference on Recent Advances in Space Technologies (RAST09)*, pp. 145–149, IEEE, 2009.
- [89] K. Iagnemma and S. Dubowsky, "Traction control of wheeled robotic vehicles in rough terrain with application to planetary rovers," The International Journal of Robotics Research, vol. 23, no. 10-11, pp. 1029–1040, 2004.
- [90] P. Schenker, T. Huntsberger, P. Pirjanian, S. Dubowsky, K. Iagnemma, and V. Sujan, "Rovers for intelligent, agile traverse of challenging terrain," in *International Conference on Advanced Robotics*, pp. 1683–1692, 2003.
- [91] G. Ishigami, Terramechanics-based Analysis and Control for Lunar/Planetary Exploration Robots. PhD thesis, Department of Aerospace Engineering, Tohoku University, 2008.
- [92] C. Grand, F. BenAmar, F. Plumet, and P. Bidaud, "Stability and traction optimization of reconfigurable vehicles. Application to a hybrid wheel-legged robot," *The International Journal of Robotics Research*, vol. 23, no. 10–11, pp. 1041–1058, 2003.
- [93] G. Freitas, G. Gleizer, F. Lizarralde, L. Hsu, and N. R. S. dos Reis, "Kinematic reconfigurability control for an environmental mobile robot operating in the amazon rain forest," *Journal of Field Robotics*, vol. 27, no. 2, pp. 197–216, 2010.
- [94] K. Yoshida, T. Watanabe, N. Mizuno, and G. Ishigami, "Terramechanics-based analysis and traction control of a Lunar/planetary rover," in *Field and Service Robotics*, pp. 225–234, Springer, 2006.

- [95] K. J. Waldron and M. E. Abdallah, "An optimal traction control scheme for off-road operation of robotic vehicles," *IEEE/ASME Transactions on Mecha*tronics, vol. 12, no. 2, pp. 126–133, 2007.
- [96] Y. Kuroda, T. Teshima, Y. Sato, and T. Kubota, "Mobility performance evaluation of planetary rover with similarity model experiment," in *Proceedings of the 2004 IEEE International Conference on Robotics and Automation*, (New Orleans, LA, USA), pp. 2098–2103, 2004.
- [97] T. Kubota and T. Naiki, "Novel mobility system with active suspension for planetary surface exploration," in *Proceedings of the 2011 IEEE Aerospace Conference*, AERO 2011, (Big Sky, MT, USA), pp. 1 – 9, 2011.
- [98] S. Hutangkabodee, Y. H. Zweiri, L. D. Seneviratne, and K. Althoefer, "Performance prediction of a wheeled vehicle on unknown terrain using identified soil parameters," in *Proceedings of the 2006 IEEE International Conference on Robotics and Automation*, (Orlando, FL, USA), pp. 3356–3361, 2006.
- [99] A. Gibbesch and B. Schäfer, "Advanced modelling and simulation methods of planetary rover mobility on soft terrain," in *Proceedings of the 8th Workshop on Advanced Space Technologies for Robotics and Automation*, (Noordwijk, The Netherlands), 2004.
- [100] K. Iagnemma, A. Rzepniewski, S. Dubowsky, and P. Schenker, "Control of robotic vehicles with actively articulated suspensions in rough terrain," Autonomous Robots, vol. 14, no. 1, pp. 5–16, 2003.
- [101] C. Johnson and C. Sandu, "Comparative analysis of lightweight robotic wheeled and tracked vehicle," in the 12th European Conf. of the ISTVS, no. 26, (Pretoria, South Africa), 2012.
- [102] G. Campion, G. Bastin, and B. D'Andréa-Novel, "Structural properties and classification of kinematic and dynamic models of wheeled mobile robots," *IEEE Transactions on Robotics and Automation*, vol. 12, no. 1, pp. 47–62,

1996.

- [103] K. Iagnemma, C. Senatore, B. Trease, R. Arvidson, K. Bennett, A. Shaw, F. Zhou, L. Van Dyke, and R. Lindemann, "Terramechanics modeling of Mars surface exploration rovers for simulation and parameter estimation," in *Proceedings of the ASME 2011 International Design Engineering Technical Conferences & Computers and Information in Engineering Conference*, (Washington, DC, USA), 2011.
- [104] C. Senatore and C. Sandu, "Torque distribution influence on tractive efficiency and mobility of off-road wheeled vehicles," *Journal of Terramechanics*, vol. 48, no. 5, pp. 372–383, 2011.
- [105] B. Ghotbi, F. González, J.Kövecses, and J. Angeles, "A novel concept for analysis and performance evaluation of wheeled rovers," *Mechanism and Machine Theory*, vol. 83, pp. 137–151, 2015.
- [106] K. Iagnemma, A. Rzepniewski, S. Dubowsky, P. Pirjanian, T. Huntsberger, and P. Schenker, "Mobile robot kinematic reconfigurability for rough-terrain," in Proceedings of the SPIE Symposium on Sensor Fusion and Decentralized Control in Robotic Systems III, vol. 4196, 2000.
- [107] A. Azimi, Wheel-Soil Interaction Modelling for Rover Simulation and Analysis. PhD thesis, Department of Mechanical Engineering, McGill University, 2013.
- [108] F. González and J. Kövecses, "Use of penalty formulations in dynamic simulation and analysis of redundantly constrained multibody systems," Multibody System Dynamics, vol. 29, pp. 57–76, 2013.
- [109] "Neptec." [Internet], [cited 2015, November 30]. Available from: http://www.neptec.com.
- [110] R. A. Lindemann and C. J. Voorhees, "Mars Exploration Rover mobility assembly design, test and performance," in *Proceedings of the IEEE International*

- Conference on Systems, Man and Cybernetics, (Waikoloa, HI, USA), pp. 450–455, 2005.
- [111] K. Nagatani, A. Ikeda, K. Sato, and K. Yoshida, "Accurate estimation of draw-bar pull of wheeled mobile robots traversing sandy terrain using built-in force sensor array wheel," in *Proceedings of the 2009 IEEE/RSJ International Conference on Intelligent Robots and Systems*, (St. Louis, MO, USA), pp. 11–15, 2009.
- [112] L. Ding, Z. Deng, H. Gao, K. Nagatani, and K. Yoshida, "Planetary rovers' wheel–soil interaction mechanics: New challenges and applications for wheeled mobile robots," *Intelligent Service Robotics*, vol. 4, no. 1, pp. 17–38, 2011.
- [113] O. Ani et al., "Analytical modeling and Multi-Objective Optimization (MOO) of slippage for Wheeled Mobile Robot (WMR) in rough terrain," Journal of Central South University, vol. 19, no. 9, pp. 2458–2467, 2012.
- [114] B. Ghotbi, F. González, J. Kövecses, and J. Angeles, "Effect of normal force dispersion on the mobility of wheeled robots operating on soft soil," in *Proceed*ings of the 2014 IEEE International Conference on Robotics and Automation, (Hong Kong, China), 2014.
- [115] B. Ghotbi, F. González, J. Kövecses, and J. Angeles, "Mobility assessment of wheeled robots operating on soft terrain," in *Springer Tracts in Advanced Robotics: Field and Service Robotics*, 2015.
- [116] M. Hirschkorn, *Dynamic Analysis of Rovers and Mobile Robots*. PhD thesis, Department of Mechanical Engineering, McGill University, 2013.
- [117] E. Bayo and R. Ledesma, "Augmented Lagrangian and mass-orthogonal projection methods for constrained multibody dynamics," *Nonlinear Dynamics*, vol. 9, no. 1-2, pp. 113–130, 1996.
- [118] N. M. Newmark, "A method of computation for structural dynamics," *Journal* of the Engineering Mechanics Division, ASCE, vol. 85, pp. 67–94, July 1959.

- [119] "The UTIAS Mars Dome." [Internet], http://sr.utias.utoronto.ca/index.php/facilities.
- [120] A. R. Reece, "Problems of soil vehicle mechanics," Tech. Rep. No. 97, Land Locomotion Laboratory, ATAC, Warren, MI, USA, 1964.
- [121] R. A. Liston and L. A. Martin, "Multi-pass behavior of a rigid wheel," in the 2nd International Conference of ISTVS, (Quebec), 1966.
- [122] I. C. Holm, "Multi-pass behaviour of pneumatic tires," *Journal of Terrame-chanics*, vol. 6, no. 3, pp. 47–71, 1969.
- [123] E. J. Haug, Computer Aided Kinematics and Dynamics of Mechanical Systems. Allyn and Bacon, 1989.
- [124] P. E. Nikravesh, Computer-Aided Analysis of Mechanical Systems. Prentice— Hall, 1988.
- [125] J. Angeles, Fundamentals of Robotic Mechanical Systems: Theory, Methods, and Algorithms. New York: Springer, third ed., 2007.
- [126] P. Flores, M. Machado, E. Seabra, and M. T. da Silva, "A parametric study on the Baumgarte stabilization method for forward dynamics of constrained multibody systems," *Journal of Computational and Nonlinear Dynamics*, vol. 6, no. 1, 2011.
- [127] E. Bayo, J. García de Jalón, and M. A. Serna, "A modified Lagrangian formulation for the dynamic analysis of constrained mechanical systems," Computer Methods in Applied Mechanics and Engineering, vol. 71, no. 2, pp. 183–195, 1988.
- [128] J. García de Jalón and E. Bayo, Kinematic and Dynamic Simulation of Multibody Systems. The Real-Time Challenge. New York: Springer-Verlag, 1994.

APPENDIX A

Soil parameter estimation for the RCP experiments

Various analyses reported in this thesis required modelling of the wheel-soil interaction. Simulation results were validated with experimental data of the same type of operation. Simulation tests can be comparable to the experimental ones if the set of soil parameters used in the terramechanics model represents the soil available in the experiments. Systematic identification of the soil parameters via bevameter and single wheel test bed was beyond the scope of this work. However, exact identification of the soil parameters was not required and only a reasonable approximation would serve the purpose of our study. It must be noted that, when validating the result of the simulations with the actual operation data, matching the numerical value of different quantities was not the objective. That is because the main goal of the simulation and experimental analyses in this thesis was studying the trend of change of various aspects of the rover performance versus the parameters of the system.

In order to obtain a set of soil parameters which can approximate the soil available in the experimental facilities the following approach was adopted: The result of series of drawbar pull experiments performed with different operation conditions were gathered to obtain a curve relating the drawbar pull to the wheel slip. These experiments were chosen to include different load distributions on the RCP and a wide range of wheel slip. In the 15 cases that were selected, the drawbar pull varied between 0 and 400 N. The classical terramechanics models that predict the terrain reactions require six soil parameters as input: n is the sinkage exponent, k_c , and k_ϕ the pressure-sinkage parameters used in Eq. (3.11), c, the terrain cohesion, ϕ , the internal friction angle, and K, the shear deformation modulus. Previous projects, carried out by MDA in the same experimental facilities (Mars Dome), reported an estimate of the soil properties. Among the above-mentioned parameters, values of c and k_c were adopted from the results of these projects. Also, Wong identified parameter n to be 1.1 for dry sand (Land Locomotion Lab) [36]. Here, n was chosen to be unity in order to keep the dimension of the rest of the soil parameters physically meaningful. The remaining three soil parameters were identified independently, but eventually the values estimated in this work did not fall far from the values reported by MDA. The methods to estimate the remaining soil parameters are described next.

The internal friction angle ϕ was estimated several times during the experiments. A box was slowly filled with sand to form a monticle whose angle was measured; this angle gave an estimation of the internal friction angle of the soil.

In order to find parameters K and k_{ϕ} each experiment was simulated in a forward-dynamics setting, using terramechanics relations. The angular velocity of the wheels in the simulation was set to match the one measured by the wheel encoders during the motion of the RCP. The effect of the variation of K and k_{ϕ} on the drawbar pull-slip curve and the wheel sinkage was studied. It was observed that the pressure-sinkage parameter k_{ϕ} mainly affected the sinkage value, while the shear deformation modulus K governed the shape of the drawbar pull-slip curve. Terramechanics relations confirm this observation: based on Eq. (3.11) for a certain load applied on the wheel, a higher value of k_{ϕ} results in a smaller wheel sinkage. Also, in Eq. (3.13) the

Table A.1. Set of soil parameters estimated via experimental results of the RCP operation in Mars Dome

| \overline{n} | c | ϕ | k_c | k_{ϕ} | K |
|----------------|-----------------|--------|---------------------------------|-------------------------|-------|
| (-) | $({\rm N/m^2})$ | (deg) | $(\mathbf{N}/\mathbf{m}^{n+1})$ | $(\mathrm{kN/m}^{n+2})$ | (m) |
| 1 | 220 | 33.1 | 1400 | 2000 | 0.015 |

relation between shear stress and normal stress includes an exponential term. This term itself is a function of the slip ratio and the shear deformation modulus, which suggests that smaller values of K result in a steeper slope of the drawbar pull-slip curve. The set of 15 simulations was repeated for different values of K and k_{ϕ} until an acceptable agreement in terms of the wheel sinkage and the shape of the drawbar pull-slip curve between the simulation and experimental results was achieved. The identified parameters are listed in Table A.1. The drawbar pull-slip data obtained from simulation using these parameters are compared with experimental data in Fig. A.1.

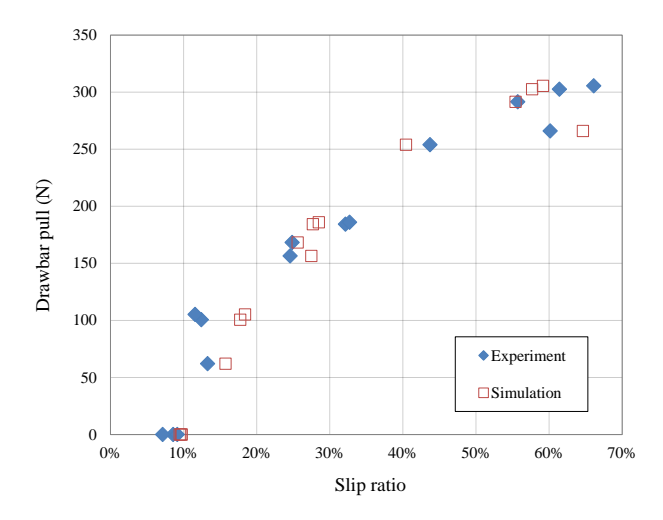


FIGURE A.1. The drawbar pull-slip curve obtained from experiments and simulations with soil parameters listed in Table A.1

APPENDIX B

The Generic Multibody Dynamics Library

B.1 Introduction

The study of large mechanical systems and their interaction with the environment can be a challenging task. The modelling of multibody systems which involve large rotations and proper representation of interaction forces (friction, contact, ...) are examples of the common sources of complexity in dynamic simulations. Additionally, determination of constraint forces particularly in the presence of redundant constraints requires especial attention. Performing various types of analyses can provide valuable information prior to the design and development of systems. Therefore, building a virtual prototyping environment to test design ideas and operation strategies can contribute greatly to design and improvement of complex mechanical systems. A modelling and simulation tool has been developed as part of this thesis that is capable of modelling the mechanical systems and their interaction with the environment. This simulation tool is developed from scratch in MATLAB and the

structure of the library together with its various features are described in this chapter. The simulation results obtained from this library has been verified against the solution of several benchmark problems.

An important motivation behind building this library was developing a toolbox which would allow full access to all dynamics terms and state variables during and after simulation runs. This is specially important in the analysis of complex systems where access to the dynamics terms and evaluation of user-defined indicators can enhances the understanding of the behaviour and performance of the system studies. Also, using this library it is possible to customize the simulation by defining new formulations, contact models, and constraints. Representing the interaction of a system with the environment is often among the most challenging parts in modelling. Some interaction models require full access to the states or other parameters of the system at every time-step or even at every iteration of the solver, in case of using implicit integrators. In the library developed in this research the user is free to implement their own force models.

This library can accommodate two approaches in designing simulation scenarios: kinematic prescription and force specification. One or a combination of these two approaches can be selected to simulate systems and their interaction with the environment. In Chapter 4 this feature is used to reproduce experimental tests in simulation where the input to they system is a mix of prescribed velocity and applied forces and moments.

Coordinate transformation can provide insight into the behaviour of the system. In the presented library bodies are defined using dependent coordinates expressed in the global inertial reference frame as described in Section B.3.1. Coordinate transformation to other sets, such as minimum set of coordinates or coordinates of the joint or task spaces, can be beneficial for analysis purposes. The algorithm

implemented in this library for transformation to a minimum set is described in Section B.10.3.

Finally, the library includes graphical representation routines to display simulation results and also develop animations. As part of the analysis results, the violation of the constraints and the mechanical energy of systems during the simulation period are displayed. In the following sections a more detailed description of the library is presented.

B.2 Structure and organization of the library

The package consists of the following elements:

- Folder < library > contains the generic routines used to set up, simulate and analyze the examples. Routines for graphic representation are included here as well. The library was written to enable code reusability, and thus the common functions and structures in this folder can be used by regular users to build their examples without the need to modify them.
- Folder <tutorials> contains simple examples with a detailed description of each part of the script.
- Folder <examples> contains some multibody models to illustrate the usage of the library. These can be used as templates to build new models.
- Folder <roverModels> contains the rover and single wheel models used in this thesis, as well as several predefined simulation scenarios.

For each example, the main part of the script which defines the model of the system and the simulation scenario appears in "mainscript.m". The interaction forces with the environment can be functions of time and states of the system. Evaluation of these forces can be required at some or all iterations of every time-step. These operations are carried out in a separate function called "updateForces.m". Customized

APPENDIX B. THE GENERIC MULTIBODY DYNAMICS LIBRARY

animation and a list of plots for each example are included in "animation.m" and "plotResults.m", respectively.

The required sections to model the system and setup the simulation in "main-script.m" are the following:

- Model and simulation parameters: In this section the variables related to the simulation settings are defined and initialized. Examples of these parameters are: characteristic dimensions or magnitudes of the system, global simulation settings (enable/disable actuation or configurations, etc.).
- Formulation parameters: The formulation type is chosen at this point and the parameters associated with the chosen formulation are defined.
- Integration parameters: The integrator is chosen from the available options and its parameters such as the integration step-size and the total duration of the simulation are defined.
- Definition of the mechanism: The mechanism is built by defining the bodies and prescribing their centre of mass position and inertial properties. Bodies are then connected via kinematic constraints.
- Definition of forces: Forces and torques acting on the system are defined and initialized.
- Retrieve indices: Indexes can be assigned to bodies, forces, and constraints to facilitate future access.
- Initial conditions: The initial configuration and velocities of the entire mechanism are defined by prescribing the initial values of the generalized coordinates and velocities.
- Pre-allocate storage: Storage is allocated to variables of interest in order to store their time history. This step is not strictly necessary but it speeds up the execution of the code.

- Numerical integration: Dynamics terms are assembled and the acceleration of the system is obtained at each time-step. The velocity and configuration of the system at the next time-step are obtained by numerical integration.
- Post processing: Some quantities such as constraint reactions and mechanical energy are evaluated as a function of data stored at runtime after the completion of integration.
- Display: Using the graphical capabilities of MATLAB the motion of the mechanism is animated and the requested quantities are plotted.

B.3 General dynamic equations

In this section the parametrization of motion and the dynamic equations adopted in this library are described.

B.3.1 Parametrization of the motion of a single body. The motion of a body i is parameterized using a set of 6 generalized velocities, namely its twist \mathbf{v}_i

$$\mathbf{v}_{i} = \begin{bmatrix} \mathbf{v}_{Gi} \\ \boldsymbol{\omega}_{i} \end{bmatrix} = \begin{bmatrix} \dot{x}_{Gi} \\ \dot{y}_{Gi} \\ \dot{z}_{Gi} \\ \vdots \\ \dot{\omega}_{xi} \\ \omega_{yi} \\ \omega_{zi} \end{bmatrix}$$
(B.1)

where \mathbf{v}_{Gi} is the velocity of the CoM of the body, and $\boldsymbol{\omega}_i$ is the angular velocity of the body. The scalar components of these are expressed in the global reference frame \mathcal{F}_0 .

In order to parameterize the rotation of a body, Euler parameters have been chosen [123, 124]. Accordingly, the position and orientation of body i are defined by a set of 7 generalized coordinates, composed of the coordinates of the centre of mass

APPENDIX B. THE GENERIC MULTIBODY DYNAMICS LIBRARY

of the body and the Euler parameters defining the rotation of the body with respect to \mathcal{F}_0 and expressed in this global reference frame.

$$\mathbf{q}_{i} = \begin{bmatrix} \mathbf{q}_{Gi} \\ \mathbf{p}_{i} \end{bmatrix} = \begin{bmatrix} x_{Gi} \\ y_{Gi} \\ z_{Gi} \\ e_{1i} \\ e_{2i} \\ e_{3i} \\ e_{0i} \end{bmatrix}$$
(B.2)

These 7 coordinates are not independent, because the Euler parameters must satisfy the algebraic constraint $\mathbf{p}_i^{\mathrm{T}}\mathbf{p}_i = 1$, where $\mathbf{p}_i = [\begin{array}{ccc} e_{1i} & e_{2i} & e_{3i} & e_{0i} \end{array}]^{\mathrm{T}}$. Matrix \mathbf{E}_i is defined as

$$\mathbf{E}_i = [e_{0i} \mathbf{I}_{3 \times 3} + \tilde{\mathbf{e}_i} - \mathbf{e}_i]$$
 (B.3)

where $\tilde{\mathbf{e}}$ is a 3 × 3 skew-symmetric matrix associated with $\mathbf{e} = [\begin{array}{cc} e_1 & e_2 & e_3 \end{array}]^{\mathrm{T}}$:

$$\tilde{\mathbf{e}} = \begin{bmatrix} 0 & -e_3 & e_2 \\ e_3 & 0 & -e_1 \\ -e_2 & e_1 & 0 \end{bmatrix}$$
 (B.4)

The relation between the time derivatives of the generalized coordinates $\dot{\mathbf{q}}_i$ and the generalized velocities \mathbf{v}_i of body i is given by

$$\begin{bmatrix} \dot{x}_{Gi} \\ \dot{y}_{Gi} \\ \vdots \\ \dot{e}_{1i} \\ \dot{e}_{2i} \\ \dot{e}_{0i} \end{bmatrix} = \underbrace{\begin{bmatrix} \mathbf{I}_{3\times3} & \mathbf{0}_{3\times3} \\ \mathbf{0}_{4\times3} & \frac{1}{2}\mathbf{E}_{i}^{\mathrm{T}} \end{bmatrix}}_{\mathbf{N}_{i}} \begin{bmatrix} \dot{x}_{Gi} \\ \dot{y}_{Gi} \\ \vdots \\ \dot{x}_{Gi} \\ \vdots \\ \omega_{xi} \\ \omega_{yi} \\ \omega_{zi} \end{bmatrix}} \Rightarrow \dot{\mathbf{q}}_{i} = \mathbf{N}_{i}\mathbf{v}_{i}$$
(B.5)

where \mathbf{N}_i is a 7 × 6 transformation matrix, $\mathbf{I}_{3\times3}$ is the 3 × 3 identity matrix, and $\mathbf{0}_{3\times3}$ and $\mathbf{0}_{4\times3}$ are the 3 × 3 and 4 × 3 zero matrices, respectively.

The rotation matrix of the body i can be expressed in terms of the Euler parameters [125]:

$$\mathbf{R}_{i} = \left(e_{0i}^{2} - \mathbf{e}_{i} \cdot \mathbf{e}_{i}\right) \mathbf{I}_{3\times3} + 2\mathbf{e}_{i}\mathbf{e}_{i}^{\mathrm{T}} + 2e_{0i}\mathbf{E}_{i}$$
(B.6)

The transformation of the scalar components (coordinates) of a vector \mathbf{d} between the local body-fixed frame of reference \mathcal{F}_i and the global reference frame \mathcal{F}_0 can be established as

$$\mathbf{d} = \mathbf{R}_i \mathbf{d}_i \tag{B.7}$$

where \mathbf{d} and \mathbf{d}_i are the 3-dimensional arrays (algebraic vectors) containing the scalar components of \mathbf{d} expressed in \mathcal{F}_0 and \mathcal{F}_i , respectively. A detailed description of Euler parameters and the way in which Eqs. (B.5) and (B.6) are obtained can be found in [124].

By default the states of the system have to be initialized so that they are compatible with the kinematic constraints. However, the user can modify the values of \mathbf{q}_i and \mathbf{v}_i arrays at the beginning of the simulation for every body. Given the rotation

matrix of the body with respect to the global reference frame the Euler parameters can be found [125].

B.3.2 Dynamic equations of a single body. Using the parametrization described above, and decomposing vector and tensor quantities in the absolute reference frame \mathcal{F}_0 , the dynamic equations of body i can be written as

$$\underbrace{\begin{bmatrix} m_i \mathbf{I}_{3\times3} & \mathbf{0}_{3\times3} \\ \mathbf{0}_{3\times3} & \mathbf{J}_{Gi} \end{bmatrix}}_{\mathbf{M}_i} \underbrace{\begin{bmatrix} \dot{\mathbf{v}}_{Gi} \\ \dot{\omega}_i \end{bmatrix}}_{\dot{\mathbf{v}}_i} + \underbrace{\begin{bmatrix} \mathbf{0}_{3\times1} \\ \tilde{\omega}_i \mathbf{J}_{Gi} \omega_i \end{bmatrix}}_{\mathbf{c}_i} = \underbrace{\begin{bmatrix} \mathbf{f}_{Gi} \\ \mathbf{n}_{Gi} \end{bmatrix}}_{\mathbf{f}_i} \tag{B.8}$$

where m_i is the mass of body i, \mathbf{J}_{Gi} is the 3×3 matrix of the inertia tensor about the centre of mass G_i , \mathbf{f}_{Gi} and \mathbf{n}_{Gi} are the 3×3 arrays of resultant force and moment at the CoM, and $\tilde{\boldsymbol{\omega}}_i$ is the 3×3 skew-symmetric matrix associated with $\boldsymbol{\omega}_i$. In this case, \mathbf{J}_{Gi} does not remain constant as the body-fixed axes are changing relative to the inertial reference frame. If \mathbf{J}_{Gi}^0 is the inertia matrix expressed in the local body-fixed axes, then

$$\mathbf{J}_{Gi} = \mathbf{R}_i \mathbf{J}_{Gi}^0 \mathbf{R}_i^{\mathrm{T}} \tag{B.9}$$

B.3.3 Dynamic equations of a set of unconstrained bodies. In the dynamic equations of a multibody system the generalized coordinates and velocities of the bodies can be concatenated into the arrays of the generalized coordinates and velocities of the entire system:

$$\mathbf{q} = \begin{bmatrix} \mathbf{q}_1^{\mathrm{T}}, ..., \mathbf{q}_{n_b}^{\mathrm{T}} \end{bmatrix}^{\mathrm{T}}$$

$$\mathbf{v} = \begin{bmatrix} \mathbf{v}_1^{\mathrm{T}}, ..., \mathbf{v}_{n_b}^{\mathrm{T}} \end{bmatrix}^{\mathrm{T}}$$
(B.10)

where n_b is the number of bodies in the system, \mathbf{q} is the $7n_b$ -dimensional array of generalized coordinates, and \mathbf{v} is the $6n_b$ -dimensional array of generalized velocities.

In the general case, the relation between the generalized coordinates of the system \mathbf{q} and the set of generalized velocities \mathbf{v} is described as

$$\dot{\mathbf{q}} = \mathbf{N}\mathbf{v} \tag{B.11}$$

where

$$\mathbf{N} = \begin{bmatrix} \mathbf{N}_1 & \mathbf{0}_{76} & \mathbf{0}_{76} & \dots & \mathbf{0}_{76} \\ \mathbf{0}_{76} & \mathbf{N}_2 & \mathbf{0}_{76} & \dots & \mathbf{0}_{76} \\ \mathbf{0}_{76} & \mathbf{0}_{76} & \mathbf{N}_3 & \dots & \mathbf{0}_{76} \\ \vdots & \vdots & \vdots & \ddots & \vdots \\ \mathbf{0}_{76} & \mathbf{0}_{76} & \mathbf{0}_{76} & \dots & \mathbf{N}_{n_b} \end{bmatrix}$$
(B.12)

where $\mathbf{0}_{76}$ represents the 7×6 zero matrix, \mathbf{N}_i was interpreted in Eq. (B.5), and $i = 1, \ldots, n_b$.

Dynamic equations of a set of rigid bodies can be given in the form

$$\mathbf{M}\dot{\mathbf{v}} + \mathbf{c} = \mathbf{f}_a \tag{B.13}$$

where \mathbf{M} is the $6n_b \times 6n_b$ mass matrix that is symmetric and positive-definite. The terms \mathbf{f}_a and \mathbf{c} stand for the $6n_b$ -dimensional arrays of generalized force, and coriolis and centrifugal terms, respectively, and $\dot{\mathbf{v}}$ is the $6n_b$ -dimensional array of generalized accelerations.

In the same way as in Eq. (B.12) the dynamic terms can be composed of the individual terms associated with each body.

$$\mathbf{M} = \operatorname{diag}\left(\mathbf{M}_{1}, \dots, \mathbf{M}_{n_{b}}\right); \quad \mathbf{c} = \begin{bmatrix} \mathbf{c}_{1} \\ \vdots \\ \mathbf{c}_{n_{b}} \end{bmatrix}; \quad \mathbf{f}_{a} = \begin{bmatrix} \mathbf{f}_{1} \\ \vdots \\ \mathbf{f}_{n_{b}} \end{bmatrix}; \dot{\mathbf{v}} = \begin{bmatrix} \dot{\mathbf{v}}_{1} \\ \vdots \\ \dot{\mathbf{v}}_{n_{b}} \end{bmatrix}; \quad (B.14)$$

B.3.4 Dynamic equations of a system of bodies constrained to each other. Kinematic pairs are used to link the bodies in the system to represent how the different system elements are connected to each other. In the general case, kinematic constraints are represented by a set of constraint equations at the velocity level. For a multibody system with n generalized velocities and m constraint equations, the constraint equations can be expressed as:

$$\mathbf{A}(\mathbf{q})\mathbf{v} + \mathbf{b}(\mathbf{q}, t) = \mathbf{0} \tag{B.15}$$

where **A** is the $m \times n$ constraint Jacobian matrix and **b** is the m-dimensional array of acatastatic terms.

These equations can be expressed at the acceleration level by differentiating with respect to time:

$$\dot{\mathbf{A}}\mathbf{v} + \mathbf{A}\dot{\mathbf{v}} + \dot{\mathbf{b}} = \mathbf{0} \tag{B.16}$$

Equations (B.15) can be expressed at the configuration level if the constraints are holonomic:

$$\phi(\mathbf{q}, t) = \mathbf{0} \tag{B.17}$$

In the case of constrained multibody systems, the equations of motion given in Eq. (B.13) must also satisfy the m constraint equations. The equations of motion are therefore modified to

$$\mathbf{M}\dot{\mathbf{v}} + \mathbf{c} = \mathbf{f}_a + \mathbf{A}^{\mathrm{T}} \boldsymbol{\lambda} \tag{B.18}$$

where λ is the *m*-dimensional array of generalized constraint forces also referred to as Lagrange multipliers. The term $\mathbf{A}^{\mathrm{T}}\lambda$ represents the array of generalized constraint forces expressed in terms of the selected generalized velocities, \mathbf{v} :

$$\mathbf{f}_c = \mathbf{A}^{\mathrm{T}} \boldsymbol{\lambda} \tag{B.19}$$

which has n components. In Eq. (B.18) both $\dot{\mathbf{v}}$ and $\boldsymbol{\lambda}$ are unknown which result in the a system of n+m unknown variables and n dynamic equations. To resolve this issue the constraint equations at acceleration level are added to the equations in (B.18), resulting in:

$$\begin{bmatrix} \mathbf{M} & -\mathbf{A}^{\mathrm{T}} \\ -\mathbf{A} & \mathbf{0} \end{bmatrix} \begin{bmatrix} \dot{\mathbf{v}} \\ \boldsymbol{\lambda} \end{bmatrix} = \begin{bmatrix} \mathbf{f}_{a} - \mathbf{c} \\ \dot{\mathbf{A}}\mathbf{v} + \dot{\mathbf{b}} \end{bmatrix}$$
(B.20)

which can be solved for $\dot{\mathbf{v}}$ and $\boldsymbol{\lambda}$ provided that the lead matrix is not singular.¹.

B.4 Library implementation

In the presented library the equations of motion of mechanical systems are generated following the steps described in the previous sections. Single bodies are building blocks of the multibody model of mechanisms. In order to define a body its mass and inertial properties, the location of its centre of mass, and the initial orientation of the body relative to the global frame, i.e., Euler parameters have to be given. The initial velocity of the body must be given via the six generalized velocities. This information is stored in a MATLAB structure called **BODIES**, described in Section B.4.1. Once all the bodies are added to the system the terms in the left hand side of Eq. (B.13) are automatically generated via internal routines.

Next, the kinematic constraints are introduced. In order to solve the system of constrained bodies values of ϕ , A, \dot{A} and \dot{b} need to be known ar every time-step. Several commonly used kinematics constraints are included in the library which have the above terms predefined. These constraints are introduced in Section B.4.2. Additionally, custom constraints can be defined by the user by providing the above-mentioned information.

 $^{^{1}}$ If **M** is symmetric and positive definite, then the solvability condition comes down to the properties of **A**, i.e., matrix **A** needs to be full row rank

APPENDIX B. THE GENERIC MULTIBODY DYNAMICS LIBRARY

Applied forces and moments are added to the system via relevant routines described in Section B.4.3. These routines collect the required information about the magnitude, direction, and point of application of forces and moments and automatically generate the array of generalized applied forces \mathbf{f}_a . For a general system of constrained bodies, the array of generalized applied forces and all other dynamic terms in Eq. (B.20) need to be updated at every time step. The equations of motion are then solved to obtain the array of generalized accelerations and Lagrange multipliers. The integration of the array of generalized accelerations yields the generalized velocities and coordinates of the next time step. The above procedures are described in detail in the following sections.

B.4.1 Data structures: BODIES, CONSTS, FORCES. Data structures are an important part of the library which enable the user to store, access and modify variables during or after the simulation. In the presented library three main data structures are defined; these are the ones which store information related to the bodies, constraints, and forces.

All the information related to the bodies are stored in a MATLAB structure called **BODIES**. For a system consisting of n_b bodies:

- BODIES.PROPS.name is a n_b -dimensional array which stores the name of each body at its associated index.
- BODIES.COORDS.q is a $7n_b$ -dimensional array which stores 7 generalized coordinates for each body in the order of body indices.
- BODIES.COORDS.qd is a $6n_b$ -dimensional array which stores 6 generalized velocities for each body in the order of body indices.
- BODIES.COORDS.qdd is a $6n_b$ -dimensional array which stores 6 generalized accelerations for each body in the order of body indices.

Other information such as the mass and inertial properties of each body are stored in **BODIES.PROPS**. Mass matrix **M**, rotation matrix **R**, and transformation matrix **N** are also stored in the **BODIES** at each time-step.

Details related to the kinematic constraints are stored in a MATLAB structure called **CONST**. For a system with l kinematic constraints and m constraint equations:

- CONSTS.LIST.name is a *l*-dimensional array which stores the name of each constraints at its associated index.
- **CONSTS.LIST.idxi** is a *l*-dimensional array which stores the index of the bodies connected by each constraint.
- **CONSTS.LIST.size** is a *l*-dimensional array which stores the number of constraint equations for each constraint.
- CONSTS.LIST.release is a *l*-dimensional array which contains an indicator for the state of each constraint: 0 if the constraint is active and 1 otherwise.

The array of Lagrange multipliers is also stored in **CONST**.

In the same way the properties associated with the applied forces are stored in **FORCES**. For a system with u applied forces:

- **FORCES.LIST.name** is a *u*-dimensional array which stores the name of each force at its associated index.
- **FORCES.LIST.idxBody** is a *u*-dimensional array which stores the index of the body each force is acting on.
- FORCES.LIST.fx, FORCES.LIST.fy, and FORCES.LIST.fz are u-dimensional arrays which store the components of each force in the x, y, and z directions, respectively. Forces can be defined in global or body-fixed reference frames. This choice is stored in a u-dimensional array called FORCES.LIST.isLocal.

• FORCES.LIST.sx, FORCES.LIST.sy, and FORCES.LIST.sz are u-dimensional arrays which store the components of the position vector of the point of application for each force with respect to its associated body CoM. The position vectors can be defined in global or body-fixed reference frames. This choice is stored in a u-dimensional array called FORCES.LIST.isLocals.

The values stored in these data structures are updated at each time-step and the old values are overwritten by the new ones. If the time history of certain terms is required by the user these terms have to be stored for each time-step in another structure called **STORAGE**.

The information related to a variable can be accessed by referring to its index in the related structure. This can be done during or after numerical integration. For convenience, names can be assigned to the index of frequently used variables.

- **B.4.2 Predefined constraints.** Several kinematic constraints are defined in the library. It is possible to add any custom constraint to the library based on the system modelling requirements. The predefined constraints in the library are:
 - Spherical joint: it eliminates 3 degrees of freedom by enforcing that two points that belong to two different bodies occupy the same location in space during motion.
 - Revolute joint: it eliminates 5 degrees of freedom by enforcing that two points that belong to two different bodies occupy the same location and prevents the relative rotation of the two bodies about two axes that are perpendicular to the axis of the revolute joint.
 - Prismatic joint: it eliminates 5 degrees of freedom by enforcing that two reference points of the two different bodies keep the same relative distance along two directions perpendicular to the axis of the prismatic joint.

- Rigid wheel-ground contact: it eliminates 4 degrees of freedom by imposing pure relative rolling and no-penetration contact (non holonomic).
- Lock: it eliminates the degree of freedom of the revolute joint and allows for prescribing its joint rate.

The following constraints are specifically defined to prescribe the motion of a single body, for example a wheel:

- Specify translational velocity: prescribes the velocity of the CoM in the global x direction. It leaves the motion in the other remaining directions free.
- Rigidly guided wheel: prescribes the velocity of the CoM in the longitudinal direction (global x) and an angular velocity about the wheel axis (global z). It leaves the motion in vertical direction (global y) free and enforces the remaining three velocities to be zero. This constraint was defined for the purpose of simulating the test conditions in a single wheel test bed which is used extensively in wheel-soil interaction studies.

It is also possible to define a constraint which engages three bodies at the same time. A constraint called differential is available in the library that adds a differential constraint to a set of three bodies, for example to the main body of a rover and its two side bogies. The differential constraint makes the rotation angle of one body equal to the average of the other two bodies. Examples of mechanical system models built using the library are shown in Fig. B.1.

B.4.3 Definition of forces. The interaction of the system with the environment can be modelled by evaluating the resultant reaction forces on the system. Note that here force is used as a general term referring to both forces and torques. Two approaches are adopted in the presented library to model the interaction with the environment:

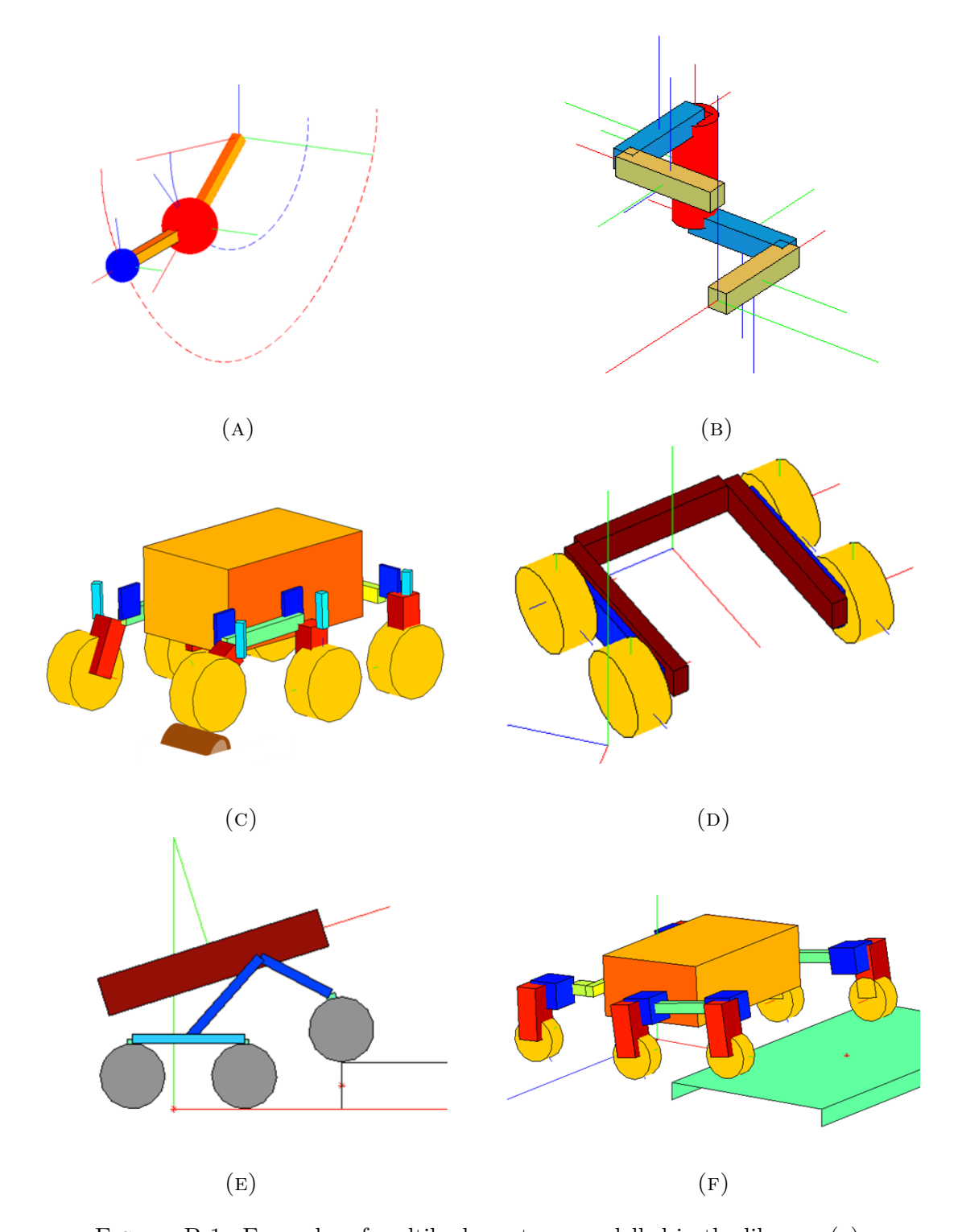


FIGURE B.1. Examples of multibody systems modelled in the library: (a) double pendulum, (b) Bricard mechanism, (c) the Rover Chassis Prototype (RCP), (d) Juno rover, (e) MER, (f) ExoMars

166

- Specifying motion: for example, the motion of velocity driven vehicles or rolling wheels can be modelled by introducing kinematic constraints.
- Specifying forces: gravitational forces, actuation, and forces computed via constitutive relations are introduced as applied forces.

Motion specification is especially useful when information on the motion of some part of the system is available but the forces that cause that motion are unknown. For examples, some wheeled robots are operated under velocity control to maintain the angular velocity of the wheels at a desired value. In order to model this scenario the desired angular velocity can be imposed on the wheels via kinematic constraints. In this case, the associated constraint force is equivalent to the actuation force required to generate the desired motion. The discussion on the system of constrained bodies and evaluation of constraint forces \mathbf{f}_c is given in Section B.3.4.

The alternative approach for modelling the interaction with the environment is via constitutive relations. The rest of this section provides the implementation details of this approach in the library. The generalized applied forces \mathbf{f}_a in Eq. (B.20) are not unknowns of the problem and their values are determined prior to integration of the equations of motion. As mentioned in Section B.2, at some or all iterations of the solver in each time-step the routine "updateForces.m" is called to update the array of generalized applied forces. In order to update these, all the forces applied on the system are evaluated based on the current state of the model.

Applied forces on the system may be constant values which are defined at the beginning of the simulation and do not change until the end of simulation time. An example of such forces is the gravitational force applied on the centre of mass of all the bodies in the system. However, the related generalized force representation can change during the simulation. Actuation force is an example of variable applied forces which is usually computed based on a feedback control relation as a function of time and state of the system. In some simulations the applied forces are updated

APPENDIX B. THE GENERIC MULTIBODY DYNAMICS LIBRARY

based on stored experimental measurements. Another type of applied forces are obtained via constitutive relations, such as contact models or terramechanics. As an example, handling of terrain reaction forces obtained from terramechanics relations to simulate the motion of a rover on soft terrain is described later in this Section.

- B.4.3.1 Definition of applied forces in the library. In the presented library there are separate routines for defining forces and torques. The input values in the case of defining forces are:
 - BODIES: to retrieve information about the state of the system
 - **FORCES**: to assign the properties of the added force to its index in the structure
 - idxBody: index of the body in the list of **BODIES** that the force is acted on
 - Scalar components of the force vector in the global or local reference frame (explained below)
 - Coordinates of the point of application with respect to the CoM of the body. This position vector can be represented in the global frame or body-fixed frame (explained below)
 - isLocals: indicates whether the coordinates of the point of application are represented in the global or local reference frame
 - name: this is optional

Scalar components of applied forces can be defined in the global reference frame \mathcal{F}_0 or in the local frame of a body. This is done by calling either "addForceGlobal" or "addForceLocal" routine. The reference frame is chosen based on the type of the force. For example, in the case of a gravitational force the global reference frame is more suitable since the direction of the force is always fixed with respect to this frame. On the other hand, in the case of a force applied by a motor or an actuator, its direction is fixed with respect to the body attached to the motor and local reference

frame of that body is more suitable for defining the actuation force. The same options are available for defining the vector which gives the position of the point of application with respect to the CoM of the body. The selected option is indicated via isLocalS. Valid values for this parameter are 'Local_s' and 'Global_s'. The applied wrenches on the system can also be categorized as internal or external. The example of gravitational force falls into the external force category while actuator effort between two bodies in the system generates internal wrench. When dealing with the latter case, it is necessary to include the applied wrenches with the same magnitude but opposite sign on both bodies.

In order to define a torque all the above input values except the point of application are required. The same as for forces, a torque can be added by calling either "addTorqueGlobal" or "addTorqueLocal" routines. Assigning a name to the index of the defined force or torque can facilitate its future referencing.

B.5 Formulation and algorithm options

Several dynamics formulations have been included in the library. Regardless of their type, all dynamics formulations must receive as an input the dynamics terms, such as mass matrix, constraint Jacobian matrix, etc, evaluated at each time-step. The unknowns in the dynamic equations are generalized accelerations and Lagrange multipliers. When selecting the formulation parameters the required precision in the solution of the forward dynamics problem as well as the stability of the simulation must be taken into consideration. In this section the formulations and algorithms implemented in the library are described.

• System of unconstrained bodies

Equations of motion of systems without kinematic constraints can be given
in the form of Eq. (B.13). Since the mass matrix is symmetric and positive

APPENDIX B. THE GENERIC MULTIBODY DYNAMICS LIBRARY

definite (SPD) the array of generalized accelerations $\dot{\mathbf{v}}$ can be directly found by solving the linear equations of motion.

• Direct solution of dynamic equations

In the presence of constraints the system of equations takes the form of Eq. (B.20). This formulation works best for systems without redundant kinematic constraints. For this type of models the lead matrix, matrix of coefficients of the unknowns, is regular and direct solution is obtained by inversion or decomposition of the lead matrix.

Direct solution of Eq. (B.20) suffers from a series of issues. The constraints are imposed at the acceleration level and therefore, the solution of Eq. (B.20) will accumulate a drift at the configuration and velocity levels. This problem can be addressed by the Baumgarte stabilization method and more accurately by projections, as will be discussed in the following options.

With n being the number of generalized velocities and m the number of constraint equations the lead matrix in Eq. (B.20) is a $(n+m) \times (n+m)$ matrix. Due to the presence of constraint Jacobian matrix in the lead matrix if the system has redundant constraints the direct solution cannot be obtained. These issues are addressed in the penalty formulation and later in the augmented Lagrangian method.

• Direct solution of dynamic equations- with Baumgarte's stabilization

As mentioned above, the problem with the direct solution of dynamic equations is that only the violation of constraints at acceleration level is enforced. Baumgarte's stabilization method penalizes the violation of constraints at velocity and position levels as well. Therefore, instead of Eq.(B.16) the following condition is used:

$$\dot{\mathbf{A}}\mathbf{v} + \mathbf{A}\dot{\mathbf{v}} + \dot{\mathbf{b}} + 2\xi\omega\left(\mathbf{A}\dot{\mathbf{q}} + \mathbf{b}\right) + \omega^2\phi = \mathbf{0}$$
(B.21)

The weight of penalization for position and velocity is determined by parameters ξ and ω . These parameters need to be adjusted depending on the system nature and the integrator used in the simulation [126]. However, $\xi = 10$ (-) and $\omega = 1$ Hz can be used as the starting point for tuning these parameters. The dynamic equations with Baumgarte stabilization technique have the form of:

$$\begin{bmatrix} \mathbf{M} & -\mathbf{A}^{\mathrm{T}} \\ -\mathbf{A} & \mathbf{0} \end{bmatrix} \begin{bmatrix} \dot{\mathbf{v}} \\ \boldsymbol{\lambda} \end{bmatrix} = \begin{bmatrix} \mathbf{f}_{a} - \mathbf{c} \\ \dot{\mathbf{A}}\dot{\mathbf{q}} + \dot{\mathbf{b}} + 2\xi\omega\left(\mathbf{A}\dot{\mathbf{q}} + \mathbf{b}\right) + \omega^{2}\boldsymbol{\phi} \end{bmatrix}$$
(B.22)

which results in a damped harmonic solution that can stabilize the constraints.

• Penalty formulation

In this approach, which is described in more detail by Bayo et al. [127], the unknown values of Lagrange multipliers λ are made proportional to the violation of constraints in Eq. (B.21):

$$\lambda = \mathbf{H} \left(\dot{\mathbf{A}} \mathbf{v} + \mathbf{A} \dot{\mathbf{v}} + \dot{\mathbf{b}} + 2\omega \xi \left(\mathbf{A} \dot{\mathbf{q}} + \mathbf{b} \right) + \omega^2 \phi \right)$$
(B.23)

where \mathbf{H} is the $m \times m$ matrix of penalty factors. In the above equation \mathbf{H} has replaced the scalar penalty factor in order to introduce the possibility of giving different weight to each constraint violation. This modification can be advantageous for incorporating structural properties of the system when evaluating the constraint forces in the presence of redundant constraints [108].

Substituting Eq. (B.23) into Eq. (B.18) leads to:

$$\mathbf{M}\dot{\mathbf{v}} = \mathbf{f}_a - \mathbf{c} + \mathbf{A}^{\mathrm{T}}\mathbf{H}\left(\dot{\mathbf{A}}\mathbf{v} + \mathbf{A}\dot{\mathbf{v}} + \dot{\mathbf{b}} + 2\omega\xi\left(\mathbf{A}\dot{\mathbf{q}} + \mathbf{b}\right) + \omega^2\phi\right)$$
(B.24)

which can be rearranged to:

$$\left(\mathbf{M} - \mathbf{A}^{\mathrm{T}}\mathbf{H}\mathbf{A}\right)\dot{\mathbf{v}} = \mathbf{f}_{a} - \mathbf{c} + \mathbf{A}^{\mathrm{T}}\mathbf{H}\left(\dot{\mathbf{A}}\mathbf{v} + \dot{\mathbf{b}} + 2\omega\xi\left(\mathbf{A}\mathbf{v} + \mathbf{b}\right) + \omega^{2}\boldsymbol{\phi}\right)$$
(B.25)

In this approach the size of the leading matrix remains $n \times n$ as opposed to $(n+m) \times (n+m)$ when solving the augmented set of unknowns, $\dot{\mathbf{v}}$ and $\boldsymbol{\lambda}$, in the previous method. In penalty formulation the Lagrange multipliers are removed from the set of unknowns and the constraint equations enter the equations of motion as a dynamical system. The constraint equations are penalized by a large penalty factor when they are incorporated in the equations of motion. Larger magnitude of the penalty factor can result in smaller violation of constraints but it can also introduce numerical ill-conditioning [127]. It is stated in [128] that by choosing a factor of 10^7 times the largest term of the mass matrix acceptable numerical results can be obtained.

• Augmented Lagrangian algorithm with projections

The main disadvantage of penalty method is the fact that the choice of penalty factors can affect the values of the Lagrange multipliers and consequently the behaviour of the entire system which may lead to incorrect simulation results. The augmented Lagrangian algorithm [127], similar to the penalty method, deals with a reduced number of equations and therefore, has all the advantages of the penalty method. On the other hand, it eliminates the variability of the results with respect to changes

in the penalty factors in **H**. As it is shown below, the penalty terms are only used as an intermediate tool to obtain the Lagrange multipliers without the need for numerical integration of the acceleration-level constraint equations. Therefore, although the value of penalty factors can affect the convergence rate, it does not change the solution of Lagrange multipliers and the simulation results. Furthermore, the augmented Lagrangian algorithm does not require large penalty factors to ensure convergence. This results in a better numerical conditioning [117].

The augmented Lagrangian algorithm leads to the following equations of motion:

$$\left(\mathbf{M} - \mathbf{A}^{\mathrm{T}}\mathbf{H}\mathbf{A}\right)\dot{\mathbf{v}} = \mathbf{f}_{a} - \mathbf{c} + \mathbf{A}^{\mathrm{T}}\mathbf{H}\left(\dot{\mathbf{A}}\mathbf{v} + \dot{\mathbf{b}} + 2\omega\xi\left(\mathbf{A}\mathbf{v} + \mathbf{b}\right) + \omega^{2}\boldsymbol{\phi}\right) + \mathbf{A}^{\mathrm{T}}\boldsymbol{\lambda}^{*}$$
(B.26)

where λ^* are the Lagrange multipliers of the modified system.

In the limit case where the constraint conditions are satisfied Eq. (B.26) becomes the same as Eq. (B.18) and $\lambda = \lambda^*$. The iteration process that leads to satisfaction of the constraints is

$$\boldsymbol{\lambda}^{(i+1)} = \boldsymbol{\lambda}^{(i)} + \mathbf{H} \left(\dot{\mathbf{A}} \mathbf{v} + \mathbf{A} \dot{\mathbf{v}} + \dot{\mathbf{b}} + 2\omega \xi \left(\mathbf{A} \mathbf{v} + \mathbf{b} \right) + \omega^2 \boldsymbol{\phi} \right)^{(i+1)}$$
(B.27)

where $\lambda^{(i)}$ is the array of Lagrange multipliers at the i^{th} iteration. Based on this algorithm, $\lambda^{(i+1)}$ introduces forces to the system which are proportional to the violation of constraints and are intended to compensate this violation. Substituting Eq. (B.27) in Eq. (B.26) gives the relation between the generalized accelerations at iteration i and i + 1:

$$\left(\mathbf{M} - \mathbf{A}^{\mathrm{T}}\mathbf{H}\mathbf{A}\right)\dot{\mathbf{v}}^{(i+1)} = \mathbf{M}\dot{\mathbf{v}}^{(i)} + \mathbf{A}^{\mathrm{T}}\mathbf{H}\left(\dot{\mathbf{A}}\mathbf{v} + \dot{\mathbf{b}} + 2\omega\xi\left(\mathbf{A}\mathbf{v} + \mathbf{b}\right) + \omega^{2}\boldsymbol{\phi}\right) \quad (B.28)$$

The iteration continues until either $\|\dot{\mathbf{v}}^{(i+1)} - \dot{\mathbf{v}}^{(i)}\|$ becomes smaller than a given threshold or the maximum number of iterations is reached. This iterative process can reduce the violation of constraints to machine precision.

An important advantage of penalty formulation and the augmented Lagrangian algorithm compared to Eq. (B.22) is due to their difference in the lead matrix. In presence of redundant constraints the lead matrix in Eq. (B.22) can become singular. However, even though mass matrix **M** is in general a positive semi-definite matrix the lead matrix in Eqs. (B.25) and (B.26) is always positive definite. That is true even in the cases of singular positions and presence of redundant constraints.

Mass-orthogonal projections can be used to enforce the exact satisfaction of constraints at the configuration and velocity levels [117]. The Baumgarte stabilization only guaranties the satisfaction of Eq. (B.21) but does not exactly satisfy $\mathbf{A}\mathbf{v} + \mathbf{b} = \mathbf{0}$ and $\boldsymbol{\phi} = \mathbf{0}$. The augmented Lagrangian algorithm yields a solution set of \mathbf{q}_{k+1}^* and $\dot{\mathbf{q}}_{k+1}^*$ which does not result in full constraint satisfaction. The objective is to perform a mass-orthogonal projection of the solution of the augmented Lagrangian algorithm to the constraint manifold in order to satisfy the constraints at both configuration and velocity levels. To this end, the following minimization problem is defined

$$\min_{\mathbf{q}} \frac{1}{2} (\mathbf{q} - \mathbf{q}^*)^{\mathrm{T}} \mathbf{M} (\mathbf{q} - \mathbf{q}^*) \quad \text{s.t. } \boldsymbol{\phi} = \mathbf{0}$$
 (B.29)

The solution of the above minimization problem is the array of generalized coordinates closest to \mathbf{q}_{k+1}^* that satisfies $\boldsymbol{\phi} = \mathbf{0}$. The mass matrix \mathbf{M} is used in the objective function in order to generate a set of dynamic equations with the same lead matrix as in Eq. (B.26).

Similarly, in order to fully satisfy the velocity level constraints the following minimization problem is defined:

$$\min_{\mathbf{v}} \frac{1}{2} (\mathbf{v} - \mathbf{v}^*)^{\mathrm{T}} \mathbf{M} (\mathbf{v} - \mathbf{v}^*) \qquad \text{s.t. } \mathbf{A}\mathbf{v} + \mathbf{b} = \mathbf{0}$$
 (B.30)

In order to solve the above constrained minimization problem penalty formulation can be used to transform these equations to the following equivalent unconstrained ones, where the details of the derivation can be found in [117].

$$\left(\mathbf{M} - \mathbf{A}^{\mathrm{T}}\mathbf{H}\mathbf{A}\right)\Delta\mathbf{q}_{k+1} = \mathbf{M}\left(\mathbf{q}_{k} - \mathbf{q}^{*}\right)$$
(B.31)

$$(\mathbf{M} - \mathbf{A}^{\mathrm{T}} \mathbf{H} \mathbf{A}) \dot{\mathbf{q}} = \mathbf{M} \dot{\mathbf{q}}^* + \mathbf{A}^{\mathrm{T}} \mathbf{H} \mathbf{b}$$
(B.32)

B.6 Integrator options

Several integrators are implemented in the library; one explicit and one implicit integrators are described here. The explicit integrator is the forward Euler method and the explicit one is the trapezoidal rule which are briefly described here.

• Forward Euler (explicit, single-step)

This integrator is not always stable and is more suitable for systems without high stiffness. In practice, this method requires very small step-sizes to be accurate. The equations used to relate the coordinates, velocities,

and accelerations from step k to k+1 are:

$$\mathbf{v}_{k+1} = \mathbf{v}_k + \Delta t \dot{\mathbf{v}}_k$$

$$\mathbf{q}_{k+1} = \mathbf{q}_k + \Delta t \mathbf{N}_k \mathbf{v}_{k+1}$$
(B.33)

• Trapezoidal rule (implicit, single-step)

This explicit integrator involves iterations and is stable and robust [118]. In the library the trapezoidal rule is implemented in a predictor-corrector fashion which is described in more detail in Section B.7. The generalized coordinates and velocities of the next time-step are evaluated according to:

$$\mathbf{v}_{k+1} = \mathbf{v}_k + \frac{\Delta t}{2} (\dot{\mathbf{v}}_k + \dot{\mathbf{v}}_{k+1})$$

$$\mathbf{q}_{k+1} = \mathbf{q}_k + \frac{\Delta t}{2} (\mathbf{N}_k \mathbf{v}_k + \mathbf{N}_{k+1} \mathbf{v}_{k+1})$$
(B.34)

B.7 Numerical integration

Once the model of the mechanism is built and the relations to represent the system's interaction with the environment are defined the numerical integration starts. In this section the procedure for stepping forward is described. Based on the formulation option or the choice of the integrator this procedure can vary. The augmented Lagrangian method with projection and trapezoidal rule for integration are selected to present the details of the procedure. Using other formulations and integrators results in some changes in this procedure but the algorithm is generally the same.

The actions described below are listed in a flowchart as illustrated in Fig. B.2. At the beginning of each time-step the generalized coordinates and velocities of the system are retrieved either from the initialized values or the values stored from the previous time-step. The interaction forces with the environment are then evaluated

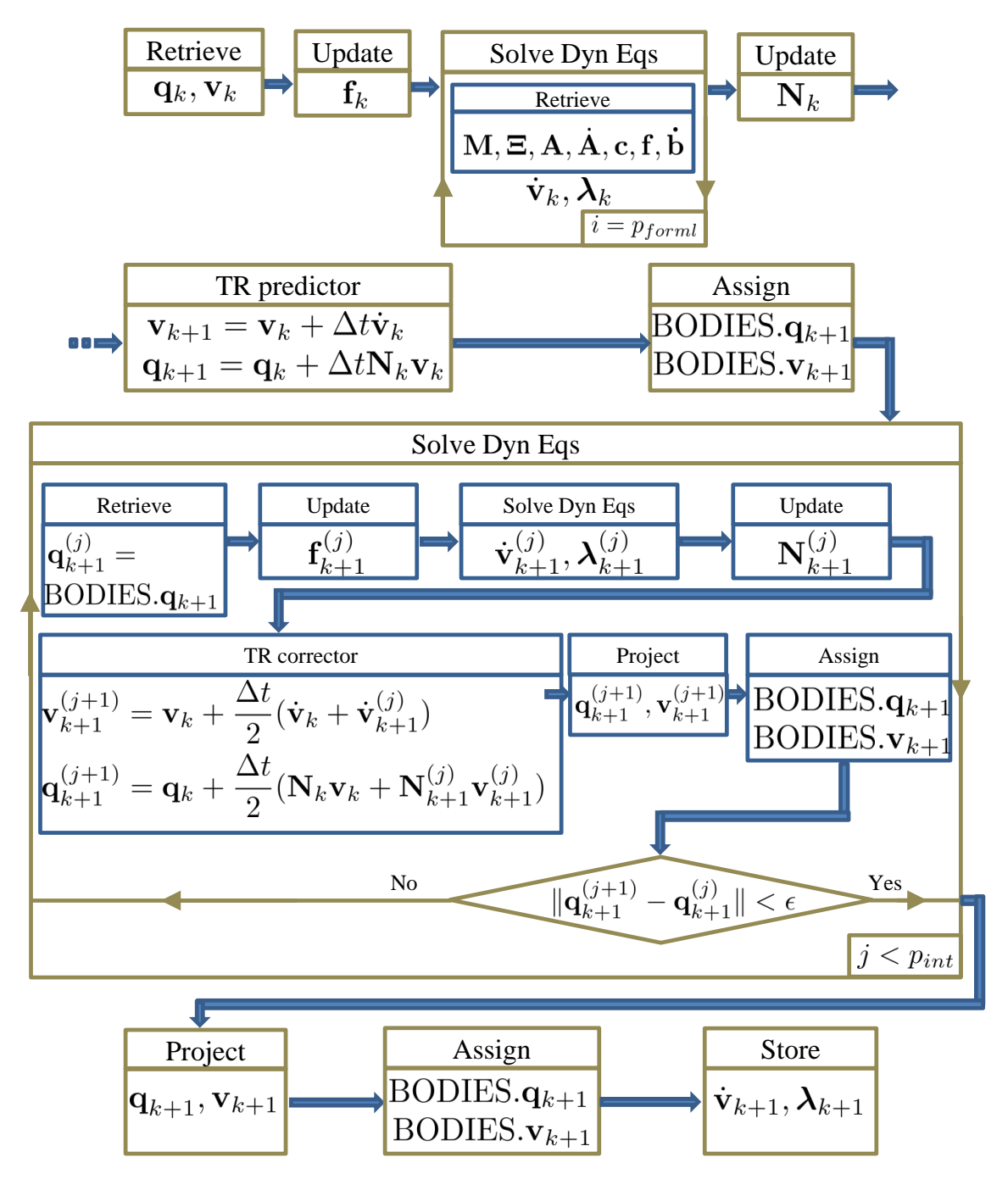


FIGURE B.2. Flowchart of the algorithm with the trapezoidal rule and the augmented Lagrangian formulation with projections

as a function of the state of the system. The dynamics terms such as mass matrix and Jacobian matrix are also evaluated for the current time-step. By solving the set of dynamic equations accelerations $\dot{\mathbf{v}}_k$ and Lagrange multipliers λ_k of the current time-step are evaluated. The dynamic equations are solved repeatedly until the maximum number of iteration allowed p_{forml} is reached. This iteration is specific to the selected type of formulation as explained in Section B.5. The criteria to exit the iteration vary in different implementations.

Next, by integrating the accelerations of the system the generalized coordinates and velocities of the next time-step, \mathbf{q}_{k+1} and \mathbf{v}_{k+1} , are obtained. Before integration the transformation matrix \mathbf{N}_k has to be updated for the current time-step. At this point the choice of integrator determines the rest of the algorithm. Here, trapezoidal rule is selected which is an implicit integrator. This integrator requires information about the acceleration at the next time-step $\dot{\mathbf{v}}_{k+1}$ which is not available at this point. Therefore, the integration includes two parts: the predictor and the corrector. First, the predictor is called which computes \mathbf{q}_{k+1} and \mathbf{v}_{k+1} from Eqs. (B.33) and assigns their values to BODIES. $\dot{\mathbf{q}}_{k+1}$ and BODIES. \mathbf{q}_{k+1} , respectively.

In the second part, the corrector, the process enters a loop which involves solving the dynamic equations and correcting the values until they converge. In this loop, first the current values of the generalized coordinates \mathbf{q}_{k+1} is stored as $\mathbf{q}_{k+1}^{(j)}$, where j is the iteration number. The array of applied forces $\mathbf{f}_{k+1}^{(j)}$ is updated based on the state of the system at iteration j. The solution of the dynamic equations yields the values for $\dot{\mathbf{v}}_{k+1}^{(j)}$ and $\lambda_{k+1}^{(j)}$. Prior to integration the transformation matrix $\mathbf{N}_{k+1}^{(j)}$ is also evaluated for the current iteration. The integration routine at this stage is called corrector since all the required information to use the trapezoidal rule in Eq. (B.34) is available and the resultant solution will be more accurate. The integration yields the generalized coordinates and velocities of the system $\mathbf{q}_{k+1}^{(j+1)}$ and $\dot{\mathbf{q}}_{k+1}^{(j+1)}$ at the next iteration.

The generalized coordinates and velocities of the system are then sent for post iteration process which in this case involves projection of the position and velocity. Again, the structure **BODIES** will be updated with the values of $\mathbf{q}_{k+1}^{(j+1)}$ and $\dot{\mathbf{q}}_{k+1}^{(j+1)}$ at iteration j+1. The iteration stops if either of the following conditions is met: first, if the difference between $\mathbf{q}_{k+1}^{(j+1)}$ and $\mathbf{q}_{k+1}^{(j)}$ is smaller than a given threshold it means that the solution has converged and no more iteration is required. If this difference is not sufficiently small the loop iterates until either the specified error threshold is met or the maximum number of iterations p_{int} is reached. In the latter case a message notifies the user that the maximum number of iteration was reached before convergence and that means that the solution might not be accurate.

In either cases, the generalized coordinates and velocities of the system will be sent again for post iteration process such as projection. Then, the structure **BODIES** is updated with the values of the states from the last iteration. Also, $\dot{\mathbf{v}}_{k+1}$ and λ_{k+1} are stored at each time-step for future access.

B.8 Post processing

After the completion of the simulation there are certain data which might be of interest but are not directly the output of the simulation. The post processing step prepares the required data in the format requested by the user. One example of such data can be calculating the generalized constraint forces in a given coordinate representation, associated with a certain kinematic constraint in the system. The Jacobian matrix and the array of Lagrange multipliers (constraint forces) are stored for every time-step and their time-history is available at the end of the simulation. Assume that the index of the constraint of interest is idxCt and it connects two bodies with indices idxB1 and idxB2. In order to get the constraint forces associated with the constraint idxCt acting on the first body idxB1 the related rows and columns of $\bf A$ and $\bf \lambda$ are multiplied. This is graphically illustrated in Fig. B.3.

$$\mathbf{idxB1} \begin{bmatrix} f_1 \\ \vdots \\ f_{6n} \end{bmatrix} = \begin{bmatrix} a_{11} & \dots & a_{1j} & \dots & a_{1m} \\ \vdots & \ddots & \vdots & \ddots & \vdots \\ a_{i1} & \dots & a_{ij} & \dots & a_{im} \\ \vdots & \ddots & \vdots & \ddots & \vdots \\ a_{(6n)1} & \dots & a_{(6n)j} & \dots & a_{(6n)m} \end{bmatrix} \begin{bmatrix} \lambda_1 \\ \vdots \\ \lambda_j \\ \vdots \\ \lambda_m \end{bmatrix} \mathbf{idxCt}$$

FIGURE B.3. Calculating the constraint forces associated with constraint of index idxCt on the body of index idxB1.

B.9 Display

Graphical representation of the simulated motion is very useful for better understanding of the system behaviour. In this library simulation results can be displayed in the following forms:

- Plots: They show the time-history of variables or compare sets of data
- Animation: Animates the motion of the system. It uses MATLAB graphics tools to draw basic shapes. One or more basic shapes can be assigned to each body. To update the graphics the CoM position and the rotation matrix of each body with respect to the global reference frame are retrieved at every time-step. Trajectory of selected points in the system, coordinate frames, and other additional details can also appear in the animation.

B.10 Analysis capabilities of the library

This library is a generic simulation tool applicable to any mechanical system. However, many of the additional features were mainly developed for rover simulation and analysis purposes which are also useful for other mechanical systems. In this section available tools for analysis of mechanical systems such as rovers and the approaches to address them are described.

B.10.1 Position, velocity, and acceleration problems. Rovers are complex multibody systems which may consist of open and closed kinematic loops in their structure. As an example, the RCP rover which is introduced in Section 4.5 consists of 28 bodies. This results in a 168×168 mass matrix with 196 generalized coordinates. In the beginning of the simulation, the initial position and velocity of all the bodies in the system have to be prescribed. For the default configuration of the rover these values are known from available CAD models. The default configuration is when the rover is placed on a flat terrain, heading towards the positive x axis (Fig. 4.10, with the generalized coordinates set to their initial values. The default velocity is zero for all the bodies. This default setting might not be suitable for some simulations. For example, some simulations start with the rover being on a slope or some wheels placed on an obstacle, or simply at a location different from the global origin. Similarly, the velocity of some bodies can be unknown at the beginning of the simulation. In these scenarios, the joint coordinates and velocities of the system are usually known but it is necessary to find the generalized coordinates and velocities of all the 28 bodies prior to the simulation. Therefore, these have to be evaluated based on the joints and other kinematic constraints that dictate the relative motion of the bodies in the system. This procedure is called solving a position or velocity problem which can be required prior to solving the initial value problems.

B.10.1.1 Position problem. In the initial position problem, the objective is to determine the generalized coordinates that satisfy the constraint equations of the system for a given set of values of the coordinates chosen as degrees of freedom. Assume a system with n generalized dependent coordinates which is subjected to m holonomic constraint equations and has p degrees of freedom. It must be noted that in presence of redundant constraints, n-m can not be used as the number of independent coordinates and therefore, p is defined. The constraint equations of the system are the ones given in Eq (B.17). Finding the value of \mathbf{q} that verifies the

APPENDIX B. THE GENERIC MULTIBODY DYNAMICS LIBRARY

constraint equations involves solving a non-linear system of equations. Expanding the constraint expressions ϕ into Taylor series around an initial approximate $\mathbf{q}^{(0)}$ and considering only the first order terms results in:

$$\phi(\mathbf{q}) \approx \phi(\mathbf{q}^{(0)}) + \mathbf{A}(\mathbf{q}^{(0)})(\mathbf{q} - \mathbf{q}^{(0)})$$
 (B.35)

The solution which satisfies $\phi(\mathbf{q}) = \mathbf{0}$ can then be found solving the following equation iteratively:

$$\mathbf{A}\left(\mathbf{q}^{(i)}\right)\Delta\mathbf{q}^{(i+1)} = -\phi\left(\mathbf{q}^{(i)}\right) \tag{B.36}$$

where i is the iteration number.

In order to solve Eq. (B.36), the array of generalized coordinates is partitioned into the (n-p)-dimensional array of dependent coordinates \mathbf{q}_D and the p-dimensional array of independent coordinates \mathbf{q}_I :

$$\mathbf{q} = \left[\begin{array}{c|c} \mathbf{q}_D^{\mathrm{T}} & \mathbf{q}_I^{\mathrm{T}} \end{array} \right]^{\mathrm{T}} \tag{B.37}$$

The constraint Jacobian matrix is partitioned accordingly:

$$\mathbf{A} = \left[\begin{array}{cc} \mathbf{A}_D & \mathbf{A}_I \end{array} \right] \tag{B.38}$$

where \mathbf{A}_D is a $m \times (n-p)$ block, and \mathbf{A}_I is a $m \times p$ block of the constraint Jacobian matrix. For systems without redundant constraints n-p=m and therefore, \mathbf{A}_D is a square full rank matrix. Given that the only unknown of the system is \mathbf{q}_D , the new lead matrix is \mathbf{A}_D and the solution of this system of equations is unique.

If the model of the system involves redundant constraints, p constraint equations that impose the desired values of the degrees of freedom are added to the system of equations in Eq. (B.36):

$$\mathbf{A}^* \left(\mathbf{q}^{(i)} \right) \Delta \mathbf{q}^{(i+1)} = -\boldsymbol{\phi}^* \left(\mathbf{q}^{(i)} \right)$$
 (B.39)

where \mathbf{A}^* is the $(m+p) \times n$ augmented constraint Jacobian matrix and $\boldsymbol{\phi}^*$ is the (m+p)-dimensional array of augmented position level constraints. Equation B.39 can be solved for $\Delta \mathbf{q}^{(i+1)}$ via performing QR decomposition of matrix \mathbf{A}^* .

It has to be noted that in solving the position problem only holonomic constraints need be considered because the non-holonomic ones do not restrict the configuration. Therefore, the Jacobian matrix **A** that is used to solve the position problem should only contain the rows corresponding to holonomic constraints and the ones related to the non-holonomic constraints have to be omitted.

B.10.1.2 *Velocity problem*. The solution of the velocity problem requires the knowledge of the configuration, or in other words, the position problem must be solved first. Despite the position problem, the velocity problem is a linear one and can be solved directly based on Eq. (B.15). The partitioning method can be useful here as well. Therefore, Eq. (B.15) can be written as:

$$\begin{bmatrix} \mathbf{A}_D & \mathbf{A}_I \end{bmatrix} \begin{bmatrix} \mathbf{v}_D \\ \mathbf{v}_I \end{bmatrix} = -\mathbf{b} \tag{B.40}$$

where \mathbf{v}_D is the (n-p)-dimensional array of dependent velocities, \mathbf{v}_I is the p-dimensional array of known independent velocities, \mathbf{A}_D is the $m \times (n-p)$ block, and \mathbf{A}_D is the $m \times p$ block of the constraint Jacobian matrix. The following set of linear equations can be solved for \mathbf{v}_D :

$$\mathbf{A}_D \mathbf{v}_D = -\mathbf{A}_I \mathbf{v}_I - \mathbf{b} \tag{B.41}$$

The difference between the position and velocity problems is that since the set of equations in Eq. (B.41) is linear there is no iteration required for solving the velocity problem and the solution is unique.

Similar to the position problem, in presence of redundant constraints, Eq. (B.40) will be replaced by:

$$\mathbf{A}^* \mathbf{v} = -\mathbf{b}^* \tag{B.42}$$

where \mathbf{A}^* is similar to the one defined in Eq. (B.39) and \mathbf{b}^* is the (m+p)-dimensional array of augmented acatastatic terms.

B.10.1.3 Acceleration problem. Acceleration problem is solved to determined the array of generalized accelerations which corresponds to the known accelerations of the system and satisfies the constraint equations. It is used is several analysis applications such as velocity transformation as described in Section B.10.3. In order to solve an acceleration problem the solution of the position and velocity problems is required. Acceleration problem is linear and can be solved directly from Eq. (B.16). Partitioning the coordinates results in

$$\begin{bmatrix} \mathbf{A}_D & \mathbf{A}_I \end{bmatrix} \begin{bmatrix} \dot{\mathbf{v}}_D \\ \dot{\mathbf{v}}_I \end{bmatrix} = -\dot{\mathbf{A}}\mathbf{v} - \dot{\mathbf{b}}$$
 (B.43)

where \mathbf{v}_D is the (n-p)-dimensional array of dependent accelerations and \mathbf{v}_I is the p-dimensional array of known independent accelerations. Equation (B.16) can be arranges as:

$$\mathbf{A}_D \dot{\mathbf{v}}_D = -\mathbf{A}_I \dot{\mathbf{v}}_I - \dot{\mathbf{A}} \mathbf{v} - \dot{\mathbf{b}}$$
 (B.44)

Again, in presence of redundant constraints, Eq. (B.43) will be replaced by:

$$\mathbf{A}^* \dot{\mathbf{v}} = -\dot{\mathbf{A}}^* \mathbf{v} - \dot{\mathbf{b}}^* \tag{B.45}$$

where $\dot{\mathbf{A}}^*$ is the $(m+p) \times n$ time derivative of the augmented constraint Jacobian matrix and $\dot{\mathbf{b}}^*$ is the (m+p)-dimensional time derivative array of the augmented acatastatic terms.

B.10.2 Force and motion specification. In some applications the purpose of simulation is to represent an actual experiment. Therefore, the best result can

be achieved if the input to the simulation can be of the similar nature to the one in the experiment. In most cases, the real operations of rovers cannot be categorized as pure forward or inverse dynamics problems. These operations are sometimes a hybrid of forward- and inverse-dynamics scenarios. Therefore, it is necessary to be able to simulate these operations in a hybrid setting. In this case, the input to the system can include both motion and force specifications. This feature is available in the library. An example of such operations is drawbar pull experiments where both the angular velocity of the wheels and the force applied to the rover are the input to the system. The output is the translational velocity of the rover which leads to the computation of the wheel slip ratios. Simulation of such operations is described in Sections 4.5.1 and 4.7.

B.10.3 Velocity transformation. In this library the *n*-dimensional array of generalized velocities is used to parameterize the motion of the system. However, other representations such as independent velocities or velocities of the end effector can be more useful for certain cases. Therefore, coordinate transformation is a tool to convert the equations of motion of the system to ones using the desired set of velocities. This feature is included in the library and as an example the description of transforming the dynamic equations to minimum set of coordinates is given in this section.

Consider a mechanical system defined by a set of n dependent generalized velocities \mathbf{v} which are subjected to a set of m constraint equations. The dynamic equations of the system are the ones given in Eq. (B.20). For the sake of simplicity in the derivation of equations in this section it is assumed that $\dot{\mathbf{b}} = \mathbf{0}$, which reduces Eq. (B.15) to

$$\mathbf{A}\mathbf{v} = \mathbf{0} \tag{B.46}$$

APPENDIX B. THE GENERIC MULTIBODY DYNAMICS LIBRARY

The objective is to transform the equations of motion to a subset of \mathbf{v} which only includes the independent velocities $\dot{\mathbf{z}}$.² If p is the number of degrees of freedom of the system, then $\dot{\mathbf{z}}$ is a p-dimensional array. The relation between \mathbf{v} and $\dot{\mathbf{z}}$ can be expressed as

$$\mathbf{v} = \mathbf{S}\dot{\mathbf{z}} \tag{B.47}$$

where **S** is a $n \times p$ dimensional transformation matrix which is not known at this stage. Differentiating Eq. (B.47) with respect to time gives:

$$\dot{\mathbf{v}} = \mathbf{S}\ddot{\mathbf{z}} + \dot{\mathbf{S}}\dot{\mathbf{z}} \tag{B.48}$$

where $\ddot{\mathbf{z}}$ is the *p*-dimensional array of independent accelerations and $\dot{\mathbf{S}}$ is the $n \times p$ dimensional time derivative of the transformation matrix. Substitution of Eq. (B.48) in Eq. (B.18) yields:

$$\mathbf{M}\mathbf{S}\ddot{\mathbf{z}} + \mathbf{M}\dot{\mathbf{S}}\dot{\mathbf{z}} - \mathbf{A}^{\mathrm{T}}\boldsymbol{\lambda} = \mathbf{f}_a - \mathbf{c}$$
 (B.49)

Equation (B.49) can be simplified by first being pre-multiplied by S^{T} :

$$\mathbf{S}^{\mathrm{T}}\mathbf{M}\mathbf{S}\ddot{\mathbf{z}} - (\mathbf{A}\mathbf{S})^{\mathrm{T}}\boldsymbol{\lambda} = \mathbf{S}^{\mathrm{T}}\left(\mathbf{f}_{a} - \mathbf{c} - \mathbf{M}\dot{\mathbf{S}}\dot{\mathbf{z}}\right)$$
(B.50)

It it shown next that with the choice of independent velocities for $\dot{\mathbf{z}}$ the second term on the left hand side of Eq. (B.50) vanishes. Substituting Eq. (B.47) in Eq. (B.46) gives:

$$\mathbf{AS}\dot{\mathbf{z}} = \mathbf{0} \tag{B.51}$$

Since $\dot{\mathbf{z}}$ is a set of independent velocities it can take any value while the above equation still holds. Thus,

$$\mathbf{AS} = \mathbf{0} \tag{B.52}$$

²In this case $\dot{\mathbf{z}} = \mathbf{v}_I$, defined in Section B.10.1

Considering Eq. (B.52), the new representation of the equations of motion (B.50) reduces to:

$$\mathbf{S}^{\mathrm{T}}\mathbf{M}\mathbf{S}\ddot{\mathbf{z}} = \mathbf{S}^{\mathrm{T}}\left(\mathbf{f}_{a} - \mathbf{c} - \mathbf{M}\dot{\mathbf{S}}\dot{\mathbf{z}}\right)$$
(B.53)

The $p \times p$ lead matrix is named $\mathbf{H} = \mathbf{S}^{\mathrm{T}}\mathbf{M}\mathbf{S}$ and the right hand side of the equation is grouped into a p-dimensional array $\boldsymbol{\kappa} = \mathbf{S}^{\mathrm{T}} \left(\mathbf{f}_a - \mathbf{c} - \mathbf{M} \dot{\mathbf{S}} \dot{\mathbf{z}} \right)$. Therefore,

$$\mathbf{H}\ddot{\mathbf{z}} = \boldsymbol{\kappa} \tag{B.54}$$

This reduces the number of equations of motion to p which is the number of degrees of freedom. The procedure is completed by finding matrix \mathbf{S} and term $\dot{\mathbf{S}}\dot{\mathbf{z}}$. They can be directly found if the expression of the constraints is available. For large systems this is not usually the case and thus, the following algorithm should be used to find \mathbf{S} and $\dot{\mathbf{S}}\dot{\mathbf{z}}$.

In order to find **S** first consider Eq. (B.47). Assume that the value of one element of $\dot{\mathbf{z}}$ is unity and the rest of the elements are zero, meaning $\dot{z}_i = 1$ and $\dot{z}_j = 0$, $\forall j \neq i$:

$$\begin{bmatrix} v_1 \\ \vdots \\ v_n \end{bmatrix} = \begin{bmatrix} S_{11} & \dots & S_{1i} & \dots & S_{1p} \\ \vdots & \ddots & \vdots & \ddots & \vdots \\ S_{i1} & \dots & S_{ii} & \dots & S_{ip} \\ \vdots & \ddots & \vdots & \ddots & \vdots \\ S_{n1} & \dots & S_{ni} & \dots & S_{np} \end{bmatrix} \begin{bmatrix} 0 \\ \vdots \\ 1 \\ \vdots \\ 0 \end{bmatrix}$$
(B.55)

Column i of the **S** matrix represents the set of generalized velocities \mathbf{v}_i that is developed as a result of $\dot{z}_i = 1$, while the other generalized velocities are zero. The procedure to compute the **S** matrix is the following:

- First, impose $\dot{z}_i = 1$ and $\dot{z}_j = 0$, $\forall j \neq i$
- ullet Solve the corresponding velocity problem $\mathbf{A}\mathbf{v}_i=\mathbf{0}$
- Repeat for $i = 1 \dots p$

• Assemble the S matrix as

$$\mathbf{S} = \left[\begin{array}{c|c} \mathbf{v}_1 & \dots & \mathbf{v}_i & \dots & \mathbf{v}_p \end{array} \right] \tag{B.56}$$

Therefore, in order to find the transformation matrix, p velocity problems have to be solved at each time-step.

Next, the array $\dot{\mathbf{S}}\dot{\mathbf{z}}$ has to be evaluated. In Eq. (B.48) if $\ddot{\mathbf{z}} = \mathbf{0}$, then $\dot{\mathbf{v}} = \dot{\mathbf{S}}\dot{\mathbf{z}}$. Therefore, the following procedure leads to computation of $\dot{\mathbf{S}}\dot{\mathbf{z}}$ for every time-step:

- First, impose $\ddot{\mathbf{z}} = \mathbf{0}$
- Solve the acceleration problem $\mathbf{A}\dot{\mathbf{v}}_0 = -\dot{\mathbf{A}}\mathbf{v}$, where $\dot{\mathbf{v}}_0$ is the array of generalized accelerations corresponding to the set of known accelerations $\ddot{\mathbf{z}}$

This procedure directly gives $\dot{\mathbf{S}}\dot{\mathbf{z}}$ because $\dot{\mathbf{S}}\dot{\mathbf{z}} = \dot{\mathbf{v}}_0$.

Document Log:

 $\label{eq:manuscript} \mbox{Manuscript Version 0}$ Typeset by $\mbox{$\mathcal{A}_{\!\!\!M}\!\mathcal{S}$-IAT_{\!\!\!E}\!X$--15 December 2015}$

Ванаген Снотві

Centre for Intelligent Machines, McGill University, 3480 University St., Montreal (Québec), H3A 2A7, Canada

 $E ext{-}mail\ address: bahareh.ghotbi@mail.mcgill.ca}$

Typeset by $\mathcal{A}_{\mathcal{M}}\mathcal{S}$ -LATEX